Polytechnic University of Catalonia
Doctorate Program in Environmental Engineering
Industrial Doctoral Thesis

A downscaling methodology for microscale wind modelling and forecasting

Industrial Ph.D. candidate:
Jordi Barcons Roca

Supervisor:
Dr. Arnau Folch
Barcelona Supercomputing Center -
Centro Nacional de Supercomputación
(BSC-CNS)

Company supervisor:
Dr. Josep Ramon Miró
Servei Meteorològic de Catalunya
(SMC)

University coordinator:
Dr. Santiago Gassó Domingo
Universitat Politècnica de Catalunya
(UPC)

September, 2017

Acknowledgements

The research conducted in this thesis has received funding from the Industrial Doctorates Plan[1] promoted by the Government of Catalonia, and the New European Wind Atlas (NEWA). ERA-NET Plus, topic FP7-ENERGY.2013.10.1.2[2]. This project would not have been possible without the support of the Servei Meteorològic de Catalunya (SMC) and the CASE department from the Barcelona Supercomputing Center - Centro Nacional de Supercomputación (BSC-CNS).

First of all, I want to express my sincere gratitude to my Ph.D. supervisor, Dr. Arnau Folch, for his mentoring, support and kindness. I also want to thank Arnau his confidence in me when I did not have it. I have no words to express my gratitude to Dr. Matias Avila for his strong support and patience throughout the PhD, because he has been key to making this project a success. My sincere acknowledge to Dr. Josep Ramon Miró for his strong willingness to provide me support and for his kindness. I would like to thank Dr. Abdel Sairouní for his advice, and especially for being the way he is.

I would also like to thank all RAM department of SMC, and especially Jordi Moré and Jordi Mercader, for their support during my first stages in SMC. I would like to thank CASE colleagues, and particularly to Alex Martí, Matias Ribero and Miguel Zavala, for sharing with me these 4 years of intense and rich moments. A warm acknowledge for Dr. Javier Sanz Rodrigo, Dr. Mireia Udina, Dr. Roberto Aurelio Chávez, Dr. Daniel Paredes and Dr. Luis Prieto for their disinterested collaboration and kindness. I also want to thank Dr. Oriol Jorba, and Dr. María Goncalves from Earth Science dept. and the co-authors Dr. Antonio Costa and Dr. Tomofumi Kozono.

And naturally, infinite gratitude goes to my family and friends, because they are the backbone of my strength. I would also like to thank my crazy-physics colleagues and Dr. Maria José González, I have been really inspired by them and their successes.

---

[1] http://doctoratsindustrials.gencat.cat

[2] http://www.neweuropeanwindatlas.eu

Industrial Doctorates Plan

The present thesis has been developed within the Industrial Doctorates Plan[3] promoted by the Government of Catalonia, via the Agency for Management of University and Research Grants (AGAUR). The aim of this program is to contribute to the competitiveness and internationalisation of Catalan industry, strengthen the tools for recruiting the talent generated in the country and place future Ph.D. holders in the right place to carry out **R**esearch&**D**evelopment&**I**nnovation projects in a company. Therefore, the industrial doctorates act as a bridge for knowledge transfer and encourage closer ties between Catalan industry, universities and research centres.

The eligible projects are open to researchers in all fields, to companies of all sizes and to students of any nationality. The thesis are developed under a collaboration agreement between both, one representative of the academy and one representative of the business, and the candidate is supervised by a thesis director from the academy and a project manager from the company. In addition, the student take part in transversal skills trainings and is given an annual mobility found to enable attendance at workshops and conferences. The Government of Catalonia provide specific funding for each of these activities related to supervision, mobility, training, etc.

---

[3] http://doctoratsindustrials.gencat.cat

Abstract

Near-surface wind fields are typically obtained from mesoscale Numerical Weather Prediction (NWP) models. These models describe the physics and dynamics of the atmosphere in the mesoscale range, *i.e.* covering atmospheric phenomena with characteristic dimensions spanning from several hundreds down to few kilometres. Operational mesoscale model configurations, which use horizontal grid resolutions from tens to ∼1 kilometre, are often insufficient to capture flow effects over complex terrains. High-resolution (tens to hundreds of meters) near-surface wind fields are strongly influenced by mesoscale sub-grid scale topographic features and can be important for several applications. Some of these applications include wind resource evaluation, wind power forecast, or simulation of wind-driven hazardous phenomena such as wildfire spreading or atmospheric dispersion of pollutants and toxic substances. In these applications, some mesoscale-to-microscale downscaling strategy turns necessary.

Traditionally, high-resolution near-surface microscale winds have been obtained by means of mass-consistent diagnostic models. These models can handle simple cases, but fail in representing flow phenomena such as recirculation behind obstacles, vortex shedding or surface boundary layer profiles. On the other hand, the increase in computational power is extending rapidly the use of Computational Fluid Dynamics (CFD) models for atmospheric simulations, including both steady or unsteady Reynolds Averaged Navier-Stokes RANS and Large Eddy Simulation (LES) models; all with turbulence closures and wall laws adapted to atmospheric flows. The dynamical NWP-CFD model coupling methodologies allow capturing physical phenomena that are not implicit in the simpler mass-consistent models. However, the computational cost of CFD models still precludes the use of dynamical downscaling strategies in routine simulations and in operational weather forecast environments. Therefore, although the ABL flow is intrinsically dynamic, operational high-resolution wind modelling below the mesoscale range should be headed towards less computationally intensive Physical-Statistical methodologies.

This Ph.D. thesis proposes an efficient, operationally affordable, novel downscaling methodology for wind field characterisation and forecast. The downscaling is based on a model chain, which considers a NWP model in the mesoscale range, a CFD-RANS model in the microscale range, and the methodologies to couple both models physically-statistically. The Ph.D. focuses on three main objectives:

Objective 1 considers the initialisation of the mesoscale model by WRF-3DVar and LAPS data assimilation systems. This first study evaluates the ability of both systems to assimilate surface automatic weather stations. Results show that 3DVar and LAPS present different assimilation

patterns; on the one side, 3DVar shows unrealistic large-scale features missing in representing the inhomogeneous nature of the near-surface fields; on the other side, LAPS reproduces small-scale features and provides an initial condition for the WRF model much consistent with observations. The validation shows that high-resolution WRF forecasts initialized with LAPS analyses improve substantially the forecasted wind fields.

Objective 2 faces the CFD-RANS model simulation of diurnal cycles to circumvent part of the limitations of the neutral atmosphere assumption. These transient simulations, together with the selection of certain time instants representative of each thermal stability regime, provide a suitable framework to incorporate atmospheric stability considerations in the downscaling. As a test case, a wind resource assessment incorporating this capability shows promising results and substantially improves the annual energy production with respect to the neutral stratified assumption.

Objective 3 focuses on the development of the downscaling strategy. The methodology combines a domain segmentation technique with the use of transfer functions to physically-statistically couple WRF and Alya-CFDWind (CFD-RANS) models. This strategy preserves the mesoscale pattern and incorporates the unresolved mesoscale model sub-grid terrain forcing effects from pre-computed microscale simulations. Nonetheless, the validation conducted shows that wind fields are still poorly characterised during the development of the convective ABL. Finally, the downscaling is successfully applied to simulate atmospheric CO_2 dispersal from a limnic eruption occured at Lake Nyos (Cameroon) in 1986.

The fulfilment of these objectives has resulted in an efficient and operationally affordable downscaling methodology designed as a NWP model post-process tool for wind field characterisation and forecast. At present, the methodology is ready to be implemented at the Meteorological Service of Catalonia (SMC) operational setup as a prototype for its validation and evaluation.

Resum

Els camps de vent pròxims a la superfície es solen obtenir a partir de models numèrics de predicció meteorològica mesoescalar (Numerical Weather Prediction: NWP). Aquests models descriuen la física i la dinàmica de fenòmens atmosfèrics amb extensions que van des de diversos centenars fins uns quilòmetres. Operacionalment, aquests models treballen a resolucions insuficients per capturar els efectes que exerceixen orografies complexes sobre el flux. Aquests efectes poden ser rellevants per aplicacions com l'avaluació i previsió del recurs eòlic o la simulació de fenòmens perillosos deguts al vent, com la propagació d'incendis forestals o la dispersió atmosfèrica de substàncies tòxiques. Per aquestes aplicacions, és necessària una estratègia de *downscaling* mesoescala-microescala.

Tradicionalment, els vents en alta resolució s'obtenen mitjançant models de diagnòstic. Aquests models, però, no són capaços de representar fenòmens com els de la recirculació darrere d'obstacles o els perfils de vent en la capa límit atmosfèrica. Gràcies a l'increment del poder computacional, l'ús de models *Computational Fluid Dynamics* (CFD) s'està extenent ràpidament. Les metodologies per acoblar dinàmicament models mesoescalars i CFDs permeten capturar fenòmens físics que no són resolts per models més simples. Tanmateix, el cost computacional dels CFD encara n'impedeix l'ús en entorns de predicció operacional. Per tant, tot i que la capa límit atmosfèrica és intrínsecament dinàmica, la modelització eòlica operativa en alta resolució ha d'enfocar-se en mètodes computacionalment menys exigents, com per exemple, mètodes estadístics o físic-estadístics.

Aquesta tesi doctoral proposa una nova metodologia per a la caracterització i pronòstic del vent en alta resolució. El *downscaling* es basa en una cadena de models; un model NWP en el rang de la mesoescala, un model CFD-RANS en el rang de la microescala, i les metodologies per l'acoblament físic-estadístic. El doctorat es centra en tres objectius principals:

Objectiu 1. S'avalua la capacitat d'assimilar estacions meteorològiques automàtiques en superfície de WRF-3DVar i LAPS, per a l'inicialització del model mesoscalar WRF. Els resultats mostren patrons d'assimilació molt diferents; el 3DVar mostra característiques de gran escala sense representar la naturalesa no-homogènia dels camps superficials; el LAPS reprodueix característiques de petita escala i proporciona una condició inicial coherent amb les observacions. La validació mostra que les prediccions del model WRF inicialitzades amb els anàlisis provinents de LAPS milloren substancialment els camps de vent pronosticats.

Objectiu 2. S'afronta la simulació de cicles diaris amb Alya-CFDWind (CFD-RANS) per tal de paliar part de les limitacions provinents de l'assumpció d'atmosfera neutra. Aquestes simulacions transitòries proporcionen un marc adequat per incorporar consideracions tèrmiques degudes a l'estratificació atmosfèrica. Els resultats de l'avaluació del recurs eòlic en un enclau

a l'estat de Puebla (Mèxic) són prometedors i substancialment millors que els obtinguts amb l'assumpció d'estratificació neutra.

Objectiu 3. Es desenvolupa l'estratègia de *downscaling*. La metodologia combina una tècnica de segmentació de dominis amb l'ús de funcions de transferència. Aquesta estratègia demostra la capacitat de preservar el patró mesoescalar i d'incorporar els efectes microescalars no resolts pel model mesoescalar. Finalment, el *downscaling* s'aplica amb èxit en la simulació d'un cas de dispersió atmosfèrica de CO_2 procedent de l'erupció límnica al Llac Nyos (Camerun, 1986).

El compliment d'aquests objectius ha donat com a resultat una metodologia de *downscaling* eficient i operacionalment assumible, dissenyada com a post-procés del model mesoescalar i que permet la caracterització i el pronòstic del camp de vents. Actualment, la metodologia està preparada per ser implementada al Servei Meteorològic de Catalunya com a prototip per a la seva validació i avaluació.

Contributions

International Journals

1. **Barcons, J.**, Folch, A., Sairouní, A., Miró, J.R., 2015. Assimilation of surface AWS using 3DVAR and LAPS and their effects on short-term high-resolution weather forecasts. Atmos. Res. 156, 160-173; doi:10.1016/j.atmosres.2014.12.019

2. Folch, A., **Barcons, J.**, Kozono, T., Ntchantcho, R., Costa., A., 2017. High-resolution modeling of atmospheric dense gas dispersion using TWODEE-2.1. Application to the 1986 Lake Nyos event. Natural Hazards and Earth System Sciences. 17, 6, 861-879; doi:10.5194/nhess-17-861-2017

3. Sanz Rodrigo, J., Allaerts, D., Avila, M., **Barcons, J.**, Cavar, D., Chávez Arroyo, R., Churchfield, M., Kosovic, B., Lundquist, J.-K., Meyers, J., Muñoz Esparza, D., Palma, JMLM., Tomaszewski, J.-M., Troldborg, N., van der Laan, M.-P., Veiga Rodrigues, C., 2017. Results of the GABLS3 diurnal-cycle benchmark for wind energy applications. IOP Conf. Series: Journal of Physics: Conf. Series 1825344(526071879)012037; doi:10.1088/1742-6596/854/1/012037

4. **Barcons, J.**, Folch, A., **in review**. A wind field downscaling strategy based on domain segmentation and transfer functions. Wind Energy

5. **Barcons, J.**, Avila, M., Folch, A., **submitted**. Diurnal cycle RANS simulations applied to wind resource assessment. Wind Energy

Conference proceedings and workshops

1. **Barcons, J.**, Folch, A., Sairouní, A., Miró, J.R., Poster: Assimilation of surface AWS using 3DVAR and LAPS and their effects on short-term high-resolution weather forecasts. EGU General Assembly 2014, Vienna, Austria.

2. **Barcons, J.**, Folch, A., Sairouní, A., Miró, J.R., Oral communication: Assimilation of surface AWS using 3DVAR and LAPS and their effects on short-term high-resolution weather forecasts. ELAPS meeting 2014, Vienna, Austria.

3. **Barcons, J.**, Avila, M., Folch, A., Oral communication: Diurnal cycle RANS simulations applied to wind resource assessment. NEWA general meeting 2017, Pamplona, Spain.

Projects participation

1. New European Wind Atlas (NEWA). ERA-NET Plus, topic FP7-ENERGY.2013.10.1.2; http://www.neweuropeanwindatlas.eu

List of acronyms

ABL Atmospheric Boundary Layer

AEP Annual Energy Production

ARW Advanced Research WRF model

AWS Automatic Weather Stations

BSC-CNS Barcelona Supercomputing Center- Centro Nacional de Supercomputación

CFD Computational Fluid Dynamics

DA Data Assimilation

GCM Global Circulation Model

HPC High Performance Computing

ID Industrial Doctorates program (Doctorats Industrials)

LES Large-Eddy Simulation

LLJ Low-Level Jet

MMM Mesoscale Meteorological Model

MOST Monin-Obukhov Similarity Theory

NWP Numerical Weather Prediction

RANS Reynolds Averaged Navier-Stokes

RHS Right Hand Side

SGS Sub-Grid Scale

SMC Meteorological Service of Catalonia (Servei Meteorològic de Catalunya)

TKE Turbulent Kinetic Energy

WPS WRF Preprocessing System

WRA Wind Resource Assessment

WRF Weather Research and Forecasting model

Contents

List of Figures

List of Tables

CHAPTER 1

Introduction

1.1 Framework

The present thesis has been developed within the Industrial Doctorates (ID) plan promoted by the Catalan Government[1]. The ID program aims at linking research centres and industry in order to strengthen relations and promote collaborations. The PhD project, entitled *Meteorological microscale forecasting using a CFD model*, started in February 2013 linking two institutions; the Meteorological Service of Catalonia (Servei Meteorològic de Catalunya; SMC)[2], and the Barcelona Supercomputing Center- Centro Nacional de Supercomputación (BSC-CNS)[3].

---

[1] http://doctoratsindustrials.gencat.cat

[2] http://www.meteo.cat

[3] https://www.bsc.es

SMC is a public enterprise and the official meteorological service of Catalonia. As an official entity, SMC is dedicated to assist and collaborate with other public entities in the areas of meteorology, climatology, and assessment of meteorological hazards. SMC also manages the meteorological observational network of the Government of Catalonia, with 185 surface automatic weather stations (AWS), 4 meteorological C band RADAR, 4 lightning detectors, 1 Daily Radiosounding station in Barcelona (launched twice a day) and 228 observer's monitoring sites, and performs meteorological forecasts for their public dissemination. Since 2008, the SMC runs operationally the mesoscale Weather Research and Forecasting (WRF) model, currently at 3 km horizontal grid resolution[4]. In the course of this thesis, the SMC implemented a nowcasting system based on a high-resolution model and sophisticated data assimilation (DA) tools to improve the accuracy and capabilities of the forecasts. Operationally, observations from satellites, radars, surface AWS, and metars are assimilated into the WRF simulations using two DA Systems (3DVar and LAPS).

BSC-CNS is a public research institution at the service of the international scientific community and industry. The center is specialised in high performance computing (HPC) and manages the MareNostrum, one of the most powerful supercomputers in Europe. The Computer Applications for Science and Engineering (CASE) department has developed an HPC code from scratch to solve complex coupled multi-physics and multi-scale problems using the finite element method. This code, called Alya[5] [Vázquez et al., 2016], solves different physics including: incompressible/compressible flow, non-linear solid mechanics, chemistry, particle transport, heat transfer, turbulence modelling, electrical propagation, etc. The CASE Environmental Simulations (ES) group applies Alya for microscale high-resolution wind field modelling in complex terrains, solving the Reynolds Averaged Navier-Stokes (RANS) equations coupled with a turbulence model adapted to atmospheric boundary layer (ABL) flows. The ES group collaborates with the wind energy industry in wind simulation over onshore and offshore wind farms and the modelling of wind turbines for wind resource assessment and short-term wind power forecasts. Present challenges entail the introduction of mesoscale information and thermal effects into the microscale simulations which, so far, assume no thermal stratification.

---

[4] http://www.meteo.cat/prediccio/models/wrf

[5] https://www.bsc.es/research-and-development/software-and-apps/software-list/alya

1.2 Motivation

Near-surface wind fields are typically obtained from mesoscale Numerical Weather Prediction (NWP) models. These models describe the physics and dynamics of the atmosphere in the mesoscale range, *i.e.* covering atmospheric phenomena with characteristic dimensions spanning from several hundreds down to few kilometres. Operational mesoscale model configurations, which use horizontal grid resolutions from tens to ∼1 kilometre, are often insufficient to capture flow effects over complex terrains. High-resolution (tens to hundreds of meters) near-surface wind fields are strongly influenced by mesoscale sub-grid scale (SGS) topographic features and can be important for several applications. Some of these applications include wind resource evaluation, wind power forecast, or simulation of wind-driven hazardous phenomena such as wildfire spreading or atmospheric dispersion of pollutants and toxic substances. In these applications, some mesoscale-to-microscale downscaling strategy turns necessary.

Traditionally, high-resolution near-surface microscale winds have been obtained by means of mass-consistent diagnostic models [e.g. Toshihiro et al., 1983; Homicz, 2002]. These models enforce the conservation of mass and, in some cases, include also additional parameterisations to approximate (not solve) microscale effects such as wind channeling and thermal slope flows. In this case, the downscaling strategy consists on obtaining an initial guess wind field from a mesoscale NWP model which is then projected over the finer complex terrain grid applying some divergence minimisation procedure [e.g. Wagenbrenner et al., 2016]. This model chain can handle simple cases, but fails in representing flow phenomena such as recirculation behind obstacles, vortex shedding or surface boundary layer profiles [e.g. Ehrhard et al., 2000]. On the other hand, the increase in computational power is extending rapidly the use of Computational Fluid Dynamics (CFD) models for atmospheric simulations, including both steady or unsteady RANS and Large Eddy Simulation (LES) models [e.g. Chávez-Arroyo et al., 2014; Castro et al., 2015; Udina et al., 2016]; all with turbulence closures and wall laws adapted to atmospheric flows.

CFD-based microscale atmospheric models explicitly solve the momentum (and eventually energy) equations and, therefore, can capture physical phenomena that are not implicit in the simpler mass-consistent models. However, open issues still exist regarding the optimal strategies for dynamical NWP-to-CFD (meso-to-micro) model coupling [e.g. Zajaczkowski et al., 2011; Castro et al., 2015], including inconsistencies between the physics of models across scales or the imposition of suitable boundary conditions for nesting [Ehrhard et al., 2000; Sanz-Rodrigo et al., 2016b]. Different downscaling strategies are being a subject of active research within the wind engineering community but, in meteorology and numerical weather prediction, progress is running more slowly. One of the reasons for this is that the computational cost of CFD models still precludes the use of dynamical downscaling strategies in routine simulations and in operational weather forecast environments.

The present thesis aims at continuing research on downscaling methodologies and designing a strategy for operational high-resolution wind forecasts. In a near future, the goal is to apply the downscaling methodology to wind forecast, atmospheric dispersion models, high-resolution regional wind characterisation studies, wind resource evaluation projects and wind power forecasts. The most important constrain comes from the limited computational capacity of end users (*e.g.* SMC), that will dictate whether the methodology can be operationally affordable or not.

1.3 Modelling the Atmospheric Boundary Layer flow

The Atmospheric Boundary Layer (ABL), also called Planetary Boundary Layer (PBL), is the lower part of the troposphere that is directly influenced by the Earth's surface, and responds to its forcings with a timescale of about an hour or less [Stull, 1988]. Depending whether it is over sea or over land, the ABL behaviour differs substantially. Over sea, the ABL resembles the free atmosphere and is mainly driven by synoptic scale patterns. Thus, the large heat capacity of water and the absence of terrain forcings usually entail smooth diurnal cycle variations. In contrast, over land, the ABL shows strong diurnal variations and very local scale effects driven by the diurnal cycle of insolation and the terrain effects. For a detailed description of the physical processes that take place in the ABL see, for example, Stull [1988]; Garratt [1994] and Wallace, Hobbs [2006].

Simulating the ABL entails solving the governing equations of the atmospheric flow. These equations are the Navier-Stokes equations, *i.e.* conservation of mass (continuity equation), conservation of momentum (Newton's second law), conservation of energy (first law of thermodynamics), and the ideal gas law. In addition, equations accounting for the conservation of moisture and other quantities of interest can be added into the system. In first instance, the simulations reliability and the physical processes solved depend on the physical model, *i.e.* the approximations used: incompressible flow, hydrostatic flow, Boussinesq approx., anelastic approx., turbulence model, etc. The physical model equations are continuos in space and time and numerical techniques are used to spatially and temporally discretise and solve theme. The order and adequacy of the numerical treatment will dictate the accuracy of the simulations. For a description of the physical approximations and numerical techniques used in NWP see, for example, Warner [2011].

1.3.1 ABL turbulence

One of the principal characteristics of the ABL flows is turbulence. Even though ABL flows can be laminar, they are mainly turbulent and contain eddies of different sizes generated mechanically and thermally, for example, by shear stress or buoyant forces. Such eddies tend to homogenise the ABL by transferring momentum, heat and moisture. The largest eddies can be of the size of the ABL and contain large amounts of energy. These large eddies loss part of their energy generating smaller eddies in a process called the turbulent cascade (Figure 1.1). Once the eddies are sufficiently small, *i.e.* the Kolmogorov scale is reached, the molecular viscosity dissipates the turbulent kinetic energy (TKE) into heat. These processes can be simulated resolving the eddies (grid-resolved scales) or modelled using empirical or theoretical models.

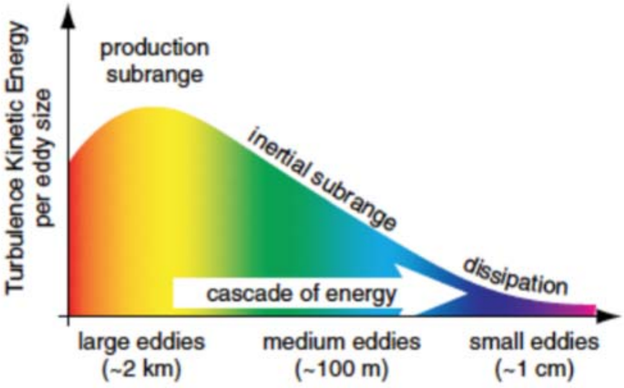

Figure 1.1
Spectrum of the turbulent kinetic energy (extracted from Wallace, Hobbs [2006]).

The modelling of the turbulence is usually called parameterisation and involves a closure problem, in which there are more unknown turbulence-related terms than prognostic equations; *i.e.* these unknowns must be parameterised as function of known quantities and parameters [Stull, 1988]. Two major approaches exist: local closures and non-local closures. On the one hand, local closures parameterise an unknown quantity at any point in space depending on values and/or gradients of known quantities at the same point. On the other hand, non-local closures use known quantities at many points for the same problem. Independently of being local or non-local, the turbulence closures are differentiated and named by their order. This means that a closure is of order n (in the literature some times also referred as $n+1$) when there is a prognostic equation for each statistical moment of order n. In this context, the statistical moment refers to a correlation between the turbulent parts of the unknowns.

The horizontal and temporal scales of the physical processes of interest determine the kind of approach. On the one hand, Mesoscale Meteorological Models (MMMs) cover phenomena with characteristic spatial dimensions spanning from several hundreds down to few kilometres, and temporal dimensions spanning from several days down to few hours. These models commonly use horizontal grid resolutions from tens to ~1 kilometre and parameterise the whole turbulence spectrum (Figure 1.1) with closures of order 1 or 1.5. On the other hand, Computational Fluid Dynamics (CFD) models, also know as microscale turbulent models, cover phenomena of around 1 kilometre or less, and of about 1 hour or less. Both approaches solve similar prognostic equations but differ on the physical processes solved and the turbulence closure models.

1.4 Microscale models

Nowadays, high-resolution wind modelling below the mesoscale limit is required for multiple applications including, among others, dispersion of pollutants at urban scale, wildfire propagation or wind resource assessment at sites with complex orography. All these applications may require of model spatial resolutions where the use of NWP models (or MMM) is not fully justified. For example, the wind energy sector needs accurate predictions of the ABL and near-surface flow characteristics at or around wind farms. Initially, industry used linear models like WAsP [Troen, Petersen, 1998] and MS-Micro [Taylor et al., 1983], based on simplified equations of motion where the advection and turbulent terms were linearised. However, because of the linear assumptions, these models fail in reproducing realistic vertical structures, especially in non neutral stratifications and steep slopes [Ayotte, 2008]. As the computational power increased and more complex sites were considered, wind industry underwent an important transition from linear to non-linear CFD models.

The CFD models allow the simulation of small-scale flows at very fine grid resolutions. Three types of CFD models exist ordered by increasing the computational cost:

- **Reynolds-Averaged Navier-Stokes (RANS)** turbulent models parameterise the whole turbulence spectrum (Figure 1.1). These models solve the averaged Navier-Stokes equations for the fluid motion introducing the Reynolds-stress term (that accounts for turbulent fluctuations) and a turbulent closure model. The degree of complexity of these models varies according to the turbulence closure model used (of order 0,1, 1.5, 2...) [Hanjalić, Kenjereš, 2008]. The most common approaches are those solving two transport equations, one for the turbulent kinetic energy (TKE) and another for a quantity related to its dissipation (*e.g* dissipation rate). Two examples are the standard $\kappa - \epsilon$ model [Jones, Launder, 1972] and the $\kappa - \omega$ model [Wilcox, 1988; Stull, 1988].

- **Large-Eddy Simulation (LES)** models explicitly simulate the larger and most energy-containing eddies (Figure 1.1). The governing equations are filtered using a spatial filter, and the phenomena with characteristic scale bellow the filter are not solved explicitly. The part of the turbulence spectrum that is not explicitly resolved is modelled by SGS closure models. The use of these models is justified under 100 m resolution [Hong, Dudhia, 2012].

- **Direct Numerical Simulation (DNS)** models are not strictly turbulent CFD models because they do not apply any parameterisation for sub-grid turbulence. Instead, they solve the equations of the fluid motion capturing the whole range of turbulent scales and, for this reason, require extremely fine grids and are the most computationally expensive [Chung, 2002]. The use of this type of models for ABL simulations is unfeasible because the resolved scales are bellow the millimetre.

Although RANS models are the least computationally-demanding models within the CFD turbulent models, they are still constrained to reduced domains due to their computational cost. Examples in literature use RANS models over domains spanning from hundreds of meters up to few km and grid-spacings from few to hundreds of meters. As these models are applied to relatively small areas and the physical models considered are limited, CFD models can not reproduce large-scale atmospheric features properly [Coirier et al., 2006; Mochida, Lun, 2008; Mochida et al., 2011].

1.5 Mesoscale to microscale downscaling strategies

The ABL is a dynamical complex system, where the scales of the involved phenomena span several orders of magnitude. However, CFD models are constrained to reduced areas (typically few km) because of their computational cost. In addition, they usually do not account for moisture, radiation or large-scale effects into the governing equations. Consequently, CFD solutions do not resemble the real atmosphere and are, somehow, idealised representations. To circumvent this limitation, mesoscale-to-microscale downscaling strategies turn necessary. Figure 1.2 summarises the different possible downscaling approaches to simulate high-resolution (tens to hundreds of meters) near-surface wind fields.

1.5.1 Physical Downscaling

The first group, the Physical Downscaling approach (Figure 1.2), is a common practice within the MMMs[6]. The one-way and two-way mesh-refinement techniques [Warner, 2011] allow these models to account for certain terrain-induced processes not captured with coarser discretizations of the topography (Figure 1.3). However, when moving towards higher-resolutions some physical issues and computational challenges need to be addressed, especially in operational applications. The MMMs contain parameterisations for the physical processes that take place in the ABL and rarely

---

[6] Holtslag et al. [2013] describe the state-of-the-art of the MMMs and climate models

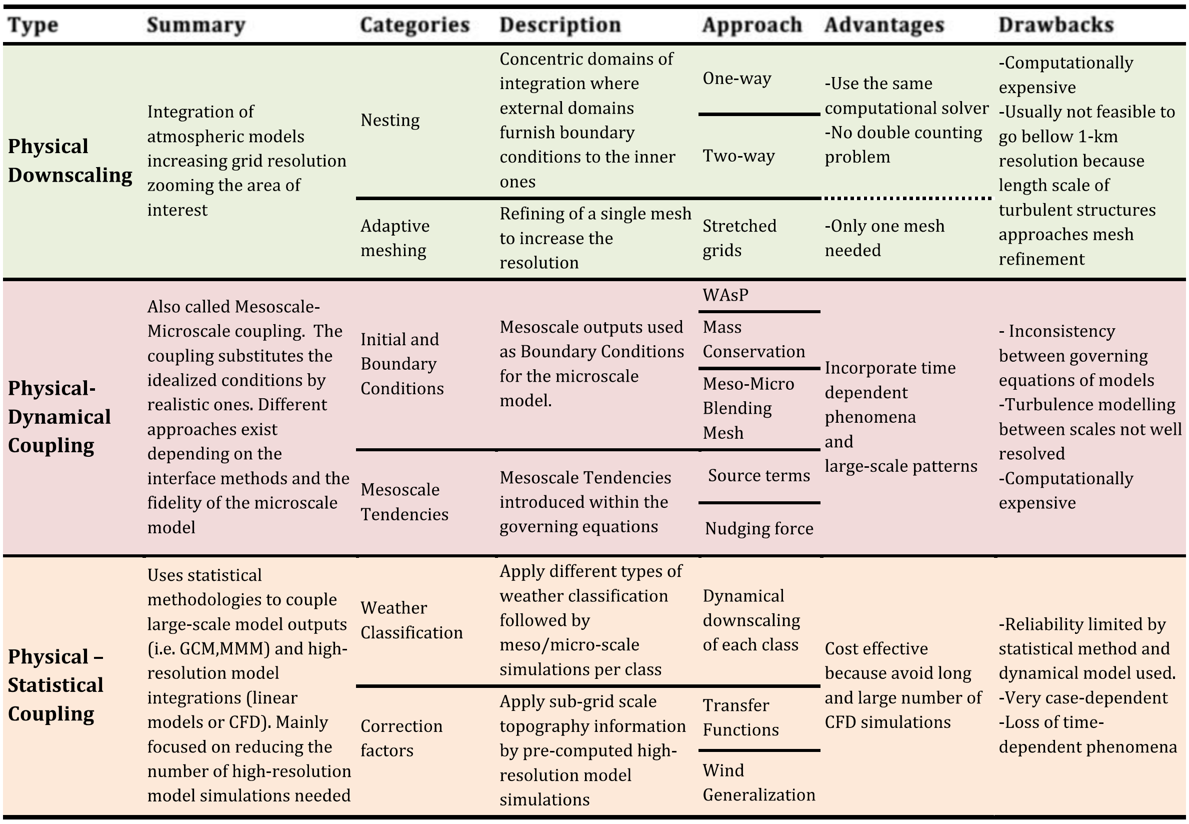

Type	Summary	Categories	Description	Approach	Advantages	Drawbacks
Physical Downscaling	Integration of atmospheric models increasing grid resolution zooming the area of interest	Nesting	Concentric domains of integration where external domains furnish boundary conditions to the inner ones	One-way	-Use the same computational solver -No double counting problem	-Computationally expensive -Usually not feasible to go bellow 1-km resolution because length scale of turbulent structures approaches mesh refinement
				Two-way		
		Adaptive meshing	Refining of a single mesh to increase the resolution	Stretched grids	-Only one mesh needed	
Physical-Dynamical Coupling	Also called Mesoscale-Microscale coupling. The coupling substitutes the idealized conditions by realistic ones. Different approaches exist depending on the interface methods and the fidelity of the microscale model	Initial and Boundary Conditions	Mesoscale outputs used as Boundary Conditions for the microscale model.	WAsP	Incorporate time dependent phenomena and large-scale patterns	- Inconsistency between governing equations of models -Turbulence modelling between scales not well resolved -Computationally expensive
				Mass Conservation		
				Meso-Micro Blending Mesh		
		Mesoscale Tendencies	Mesoscale Tendencies introduced within the governing equations	Source terms		
				Nudging force		
Physical – Statistical Coupling	Uses statistical methodologies to couple large-scale model outputs (i.e. GCM,MMM) and high-resolution model integrations (linear models or CFD). Mainly focused on reducing the number of high-resolution model simulations needed	Weather Classification	Apply different types of weather classification followed by meso/micro-scale simulations per class	Dynamical downscaling of each class	Cost effective because avoid long and large number of CFD simulations	-Reliability limited by statistical method and dynamical model used. -Very case-dependent -Loss of time-dependent phenomena
		Correction factors	Apply sub-grid scale topography information by pre-computed high-resolution model simulations	Transfer Functions		
				Wind Generalization		

Figure 1.2

Table based on the types of downscaling approaches exposed in Sanz-Rodrigo et al. [2016a].

use grid spacings near or less than 1 km. Thus, MMMs assume that the model grid size is large enough so that the whole turbulence spectrum has a sub-grid scale nature and, consequently, do not resolve turbulent motions explicitly.

During the HiRCoT (*High Resolution Modelling in complex Terrain*) workshop [Arnold et al., 2012] held in Vienna in February 2012, the role of the MMM ABL parameterisations was discussed. As stated in Arnold et al. [2012], the use of turbulence parameterisations below 1 km grid-size becomes questionable when attaining the mixing problems driven by turbulence, because this mixing starts being explicitly resolved by the model. The length scale of turbulent structures within this region of the spectrum, named *Terra incognita* by Wyngaard [2004], approaches the mesh refinement and a transition between mesoscale and microscale meteorology occurs. Hence, this transition may imply the substitution of turbulence parameterisations by formulations for the explicit horizontal and vertical diffusion and the use of SGS models like in WRF-LES [e.g. Skamarock et al., 2008; Moeng et al., 2007; Mirocha et al., 2010].

The computational cost of simulations is another issue when increasing resolution. For example, Morton et al. [2010] used a case study to illustrate the impacts of increasing resolution from 27

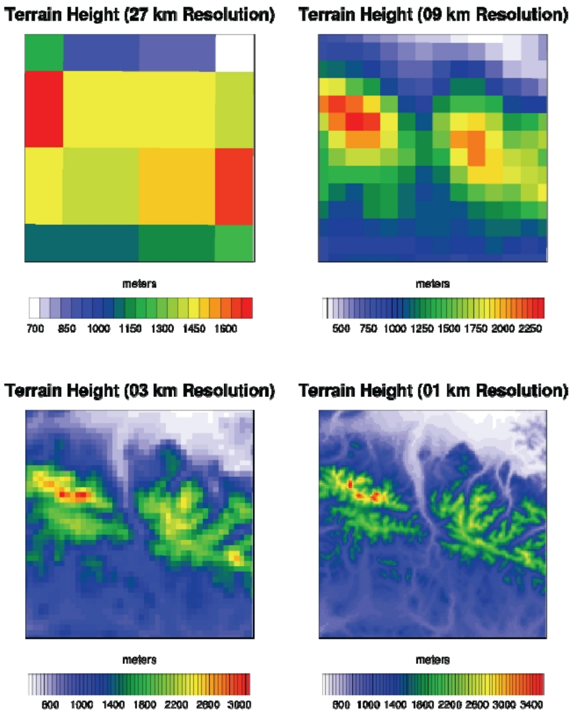

Figure 1.3
MMM terrain height resulting from 27 to 1-km grid spacing topography refinement (extracted from Morton et al. [2010]).

down to 1 km. Their nest-down strategy using the WRF model considered domains with 27, 9, 3 and 1 km horizontal resolutions and, as expected, concluded that simulations at 1 km grid spacing were in much better agreement with observations than those of coarser domains. However, the main drawback was the computational cost, where they found that the transition from 9 to 1km horizontal resolution (for the same domain) increased the computational time from 1 hour to 1 month and the storage requirements by almost two orders of magnitude.

1.5.2 Physical-Dynamical coupling

The second group, the Physical-Dynamical coupling approach, drive a CFD model through a "nest-down" strategy, just like Global Circulation models (GCM) drive NWP models on a limited area. In this case, a NWP model furnishes initial and time-dependent boundary conditions to the CFD model. In addition to this, there also exists the possibility to incorporate mesoscale tendencies into the CFD governing equations as advective and pressure gradient source terms [e.g. Sanz-Rodrigo et al., 2017].

Several methodologies that dynamically couple NWP and CFD models have been developed in recent years, see for example Kunz et al. [2000]; Coirier et al. [2006]; Baik et al. [2009]; Yamada, Koike [2010]; Li et al. [2010]; Haupt et al. [2010]; Castro et al. [2014]. This type of methodologies present four challenges; first, the inconsistency between governing equations of models, *i.e.* compressible/incompressible, turbulence modelling, etc. Second, the difference in vertical grid resolutions that require the use of three-dimensional spatial interpolation schemes and a specific treatment for the values within the surface layer. Third, the difficulty to avoid double counting problems in certain approaches. And last but not least, the computational cost of the CFD transient simulations, that limits the range of applicability of these physical-dynamical coupling methodologies.

The NWP-CFD physical-dynamical coupling methodologies have been proven as a valuable tool in urban simulations. One of the earliest approaches was proposed by Ehrhard et al. [2000] and Kunz et al. [2000]. These authors coupled the NWP model MEMO with the MIMO RANS $k-\varepsilon$ turbulence model to simulate the wind flow and the dispersion of pollutants over an industrial area. This methodology was used to calculate quasi-steady flow fields and the results showed good agreement with observations even if predicted wind speeds were slightly overestimated. Coirier et al. [2006] is another example of urban pollutant dispersion modelling. They used the model WRF and the CFD-Urban RANS model with a variant of the standard $k-\varepsilon$ turbulence model. In this work, two different strategies of coupling were addressed; an unsteady coupling mode to provide "continuous" boundary conditions to CFD-Urban and, a quasi-steady mode where successive CFD steady states were computed and the solutions linearly interpolated in time. Coirier et al. [2006] concluded the study strongly recommending the use of the quasi-steady approach for operational purposes given the large computational resources needed by the unsteady approach.

Thanks to the research done in the field and the rapid increase on computational power, these methodologies have been extended; Table 1.1 lists some examples. The majority of these approaches used turbulent RANS models partly because they are the less computationally demanding within the CFD models. Even so, models were run for research purposes and some of them stated explicitly that the computational cost precludes operational forecasts applications. So, although the ABL flow is intrinsically dynamic, operational high-resolution wind modelling below the mesoscale range

Table 1.1
List of some physical-dynamical coupling strategies found in the literature.

Reference	**MMM**	**CFD**
Baik et al. [2009]	MM5	RANS $k-\varepsilon$
Tewari et al. [2010]	WRF	CFD-Urban
Li et al. [2010]	RAMS	FLUENT RANS $k-\varepsilon$
Yamada, Koike [2010, 2011]	WRF	A2C model
Haupt et al. [2010]; Zajaczkowski et al. [2011]	WRF	AcuSolve hybrid RANS/LES *
Miao et al. [2013]	WRF	OpenFOAM RANS $k-\varepsilon$ model
Castro et al. [2014]	WRF	WINDE RANS $k-\varepsilon-l$ and $k-l$

* *The commercial CFD model AcuSolve uses a one-equation turbulence model [Spalart et al., 1997]*

should be headed towards less computational intensive approaches, for example, Physical-Statistical methodologies discussed in next section.

1.5.3 Physical-Statistical coupling

The last group presented in Figure 1.2 is the Physical-Statistical coupling between mesoscale and microscale models, sometimes also called Statistical-Dynamical. These downscaling strategies are often used within the wind energy sector for wind resource evaluation and short-term forecast. Their high potential comes from the statistical methods, that are mainly focused on reducing the number of microscale simulations required. Frey-Buness et al. [1995] was one of the earliest approaches using weather classification techniques for the assessment of regional climate patterns. This kind of approaches assumes that any regional climate can be associated with a specific combination of large-scale weather situations. In this way, the statistical weather classification is based on a clustering analysis to find out a set of weather representatives of a region (from GCM simulations, reanalysis data sets, observations, etc). Each one of these representatives is dynamically downscaled using numerical models and can be weighted according to their climate-specific frequencies. Some examples are Frey-Buness et al. [1995], Frank, Landberg [1997], Mengelkamp et al. [1997], Pinto et al. [2010] or Badger et al. [2014]. Concretely, Badger et al. [2014] presented a sophisticated version, which defined a methodology with three steps; a pre-process generating wind classes from a reanalysis dataset using the wind direction, wind speed, and the Froude number; a dynamic downscaling of each wind class using a mesoscale model; and a post-process that uses a complex methodology called, the wind generalisation technique.

The wind generalisation together with transfer-function methodologies assume that certain quantities can be corrected by introducing SGS effects. The former is based on the concept that the topographic effects on wind field are linear combinations of orographic and roughness effects [e.g. Badger et al., 2014]. On the other hand, transfer functions assume that certain quantities can be correlated over space, time or across different scales. For example, Veiga Rodrigues et al. [2008] used transfer functions for short-term wind power forecast. The methodology is based on the possibility that the wind velocity and direction at two different spatial locations can be correlated, solely using these two variables. Sanz-Rodrigo et al. [2010] used transfer functions to combine a distribution of the long term geostrophic wind statistics (wind direction, wind speed and stability) with CFD simulations, and obtain near-surface wind fields.

All these Physical-Statistical coupling strategies, *i.e.* Weather classification and transfer-function methodologies, mainly rely on a model chain (*e.g.* a MMM and a CFD) and the statistical methods used. Therefore, a successful downscaling requires a high quality large-scale data, because uncertainties are transmitted down to smaller scales. In addition, the transfer-function methods can fail at reproducing time-dependent phenomena because models are not dynamically coupled.

1.6 Thesis objectives

The main objective of this thesis is to develop a modelling strategy to set up a prototype for operational high-resolution wind forecasts at SMC and BSC-CNS. This implies the design an efficient downscaling methodology to obtain wind fields at resolutions from tens to few hundreds of meters. One constraining requirement is that the prognostic tool has to be computationally affordable by the SMC operational setup. Since the very beginning, the downscaling methodology has been thought as a chain of models, one model working in the mesoscale range and the other in the microscale range. In this way, both institutions bring their knowhow into the development; the SMC in the mesoscale side using the WRF model, and the BSC-CNS (ES team) in the microscale side using Alya. The design of the downscaling methodology has been sub-divided in three main thesis objectives:

Objective 1. Improvement of the MMM initial conditions by AWS Data Assimilation

Clearly, the accuracy of a downscaling methodology depends on the mesoscale simulations, and these on their initial conditions[7]. Any inaccuracy in the mesoscale range will propagate through the cascade of scales of the model chain. Thus, we focus on the initialisation of the WRF model. The objective is to investigate different data assimilation (DA) techniques to incorporate surface automatic weather stations (AWS) data into the model analysis (initial condition) to better represent the near-surface atmosphere initial state.

Objective 2. Incorporation of thermal effects in the microscale simulations

The ABL RANS model in Alya[8], called Alya-CFDWind model [Avila et al., 2013, 2017], is a state-of-the-art model used by industry for wind simulation in complex terrains. This model is adapted to simulate ABL flows under neutral stratification, an assumption that can lead to inaccurate modelling results and to large uncertainties at certain sites. In order to account for dynamical and thermal effects in the downscaling, one needs to address the simulation of diurnal cycles accounting for thermal stratification.

Objective 3. Design of the downscaling methodology

The ultimate objective of this thesis is to design a strategy for operational high-resolution wind forecast. SMC and BSC-CNS envisioned a downscaling methodology capable of taking advantage of the Alya-CFDWind microscale high-resolution wind field modelling. However,

---

[7] The atmospheric modelling is said to be an initial-value problem [Warner, 2011].

[8] https://www.bsc.es/research-and-development/software-and-apps/software-list/alya

because the limited computational capacity of SMC, Physical-Statistical methodologies suppose a good alternative to the pure Physical-Dynamical coupling strategies. The challenge is to redefine and adapt strategies that are not usually applied in NWP models.

1.7 Thesis structure

This Introduction has presented the framework in which the present PhD thesis has been developed; the ID program, the institutions involved and the background motivations. It has also overviewed some important aspects of the ABL flow modelling, stressing on turbulence and the multiplicity of scales. Various approaches and models, *i.e.* mesoscale and microscale models, and the need to circumvent the conflict between resolved and parameterised turbulence have been presented. Current mesoscale-to-microscale downscaling strategies have been introduced and the objectives exposed.

Chapter 2 presents the models that form the model chain in the proposed downscaling methodology. This chapter presents the MMM model WRF-ARW version 3.4.1, its governing equations, the different physical parameterisations available and the boundary conditions furnished for real cases. The chapter continues introducing the Alya-CFDWind model; the governing equations, the boundary conditions implemented and, shortly, the preprocessing tools.

Chapter 3 focuses on improving the initialisation of the WRF model, investigating different data assimilation (DA) techniques to incorporate surface AWS data into the model analysis (objective 1). The chapter starts presenting the challenges found in the assimilation of AWS, and the observational network of the Government of Catalonia. Two DA systems are selected to better represent the initial state for the WRF model. Both systems are extensively compared and validated using a set of common mesoscale meteorological cases occurring within the region of Catalonia. This chapter is an elaboration of the material in

Barcons, J., Folch, A., Sairouní, A., Miró, J.R., 2015. Assimilation of surface AWS using 3DVAR and LAPS and their effects on short-term high-resolution weather forecasts. Atmos. Res. 156, 160-173; doi:10.1016/j.atmosres.2014.12.019

Chapter 4 deals with the simulation of diurnal cycles accounting for thermal stratification using the AlyaCFDWind model (objective 2). The chapter first presents the thermal model that has been implemented and the new terms appearing in the governing equations. The complete diurnal-cycle methodology comprehends the 1D precursor simulations, the 3D diurnal cycle simulations, and the definition of stability classes. The methodology is applied to wind resource assessment on complex terrain site at the mexican state of Puebla. Finally, this chapter presents an initial 1D test case to incorporate mesoscale tendencies into the diurnal cycle simulations. This chapter is an elaboration of the material in

Barcons, J., Avila, M., Folch, A., **submitted**. Diurnal cycle RANS simulations applied to wind resource assessment. Wind Energy

Chapter 5 presents a cost-effective alternative wind field downscaling strategy based on domain segmentation and transfer functions (objective 3). The methodology is validated for the Puebla site presenting qualitative and quantitative results; first, using the neutral stability approach and then, introducing the AlyaCFDWind diurnal cycle simulations and ABL stability classes discretisation strategy. This chapter is an elaboration of the material in

Barcons, J., Folch, A., **in review**. A wind field downscaling strategy based on domain segmentation and transfer functions. Wind Energy

Chapter 6 applies the downscaling methodology (using the neutral stability approach for simplicity) coupled with the TWODEE dense gas dispersal model in a real CO_2 gas dispersion occurred at lake Nyos, Cameroon in 1986. The chapter presents the TWODEE model equations and overviews the Lake Nyos limnic eruption and previous modelling results. Following sections present the WRF, Alya-CFDWind and downscaling results for the Nyos region. Finally, this chapter presents the high-resolution dispersal modelling results. This chapter is an elaboration of the material in

Folch, A., **Barcons, J.**, Kozono, T., Ntchantcho, R., Costa., A., 2017. High-resolution modeling of atmospheric dense gas dispersion using TWODEE-2.1. Application to the 1986 Lake Nyos event. Natural Hazards and Earth System Sciences. 17, 6, 861-879; doi:10.5194/nhess-17-861-2017

Conclusion and Future work summarises the previous chapters, analyses the strengths and weaknesses of the downscaling methodology and sketches the structure of the SMC operational setup. This concluding chapter also discusses about future validations plans and methodology improvements.

CHAPTER 2

The physical models

This chapter presents the physical models used in the thesis. The WRF[1] and the Alya-CFDWind models are respectively the mesoscale and the microscale models present in the model chain. WRF description is mainly extracted from Skamarock et al. [2008] and presented here as overall vision of the model. The Alya-CFDWind [Avila et al., 2013, 2017] is presented in its thermally neutral formulation because this was the version implemented in Alya code[2] [Vázquez et al., 2016; Houzeaux et al., 2009] at the initial stages of the present thesis.

2.1 The WRF mesoscale model

WRF[3] is a NWP model and a atmospheric simulation system designed for both research and operational applications [Skamarock et al., 2008]. The model is the result of a multi-agency effort to develop a flexible, state-of-the-art and portable code computationally efficient for both massive-parallel supercomputers and personal computers. The WRF system offers two different dynamic solvers.

---

[1] http://www2.mmm.ucar.edu/wrf/users/

[2] https://www.bsc.es/research-and-development/software-and-apps/software-list/alya

[3] http://www2.mmm.ucar.edu/wrf/users/

On the one hand, the Advanced Research WRF (ARW) developed primarily at, and supported by, the National Center for Atmospheric Research's (NCAR). On the other hand, the Non-hydrostatic Mesoscale Model (NMM) solver developed at the the National Oceanic and Atmospheric Administration's (NOAA) National Centers for Environmental Prediction (NCEP). The present doctoral thesis considers the WRF-ARW system version 3.4.1. for the model chain.

The WRF-ARW possible applications span across scales ranging from global down to LES. Some features that make this possible are the global simulation capability using Fourier filter and periodic east-west conditions, the one-way and two-way nesting options, or the different map projections supported. In addition, the system encompasses many numerical and physical options, and packages like the WRF preprocessing system (WPS) and the data assimilation system (WRF-DA). This section focus on the model governing equations, the physical schemes used for model solution, and the settings of initial and boundary conditions.

2.1.1 WRF-ARW governing equations

The WRF-ARW dynamics solver integrates the fully compressible, non-hydrostatic Euler equations, formulated in flux conservative form (using mainly variables that have conservation properties). These equations are written in a terrain-following hydrostatic-pressure vertical coordinate system in terms of the dry-air mass column defined as:

$$\eta = \frac{p_h - p_{ht}}{\mu} \quad \text{where} \quad \mu = p_{hs} - p_{ht} \tag{2.1}$$

where p_h is the hydrostatic component of the pressure, and p_{hs} and p_{ht} are the pressures at the surface and at the top boundary, respectively. Note that η varies from 1 at the surface to 0 at the top boundary (p_{ht} is set constant during integration). The WRF-ARW moist governing equations are [Skamarock et al., 2008]:

Momentum eqs.

$$\left\{\begin{aligned}
&\tfrac{\partial U}{\partial t} + \nabla \cdot \boldsymbol{V} u + \mu\alpha \tfrac{\partial p}{\partial x} + \tfrac{\alpha}{\alpha_d}\tfrac{\partial p}{\partial \eta}\tfrac{\partial \phi}{\partial x} &&= F_U && (2.2)\\
&\tfrac{\partial V}{\partial t} + \nabla \cdot \boldsymbol{V} v + \mu\alpha \tfrac{\partial p}{\partial y} + \tfrac{\alpha}{\alpha_d}\tfrac{\partial p}{\partial \eta}\tfrac{\partial \phi}{\partial y} &&= F_V && (2.3)\\
&\tfrac{\partial W}{\partial t} + \nabla \cdot \boldsymbol{V} w + g\left(\mu - \tfrac{\alpha}{\alpha_d}\tfrac{\partial p}{\partial \eta}\right) &&= F_W && (2.4)
\end{aligned}\right.$$

Energy eq.

$$\tfrac{\partial \Theta}{\partial t} + \nabla \cdot \boldsymbol{V}\theta = F_\Theta \tag{2.5}$$

Mass eq.

$$\tfrac{\partial \mu}{\partial t} + \nabla \cdot \boldsymbol{V} = 0 \tag{2.6}$$

Geopotential eq.

$$\tfrac{\partial \phi}{\partial t} + \tfrac{1}{\mu}\left(\boldsymbol{V} \cdot \nabla\phi - gW\right) = 0 \tag{2.7}$$

Transport of species eqs.

$$\tfrac{\partial Q_m}{\partial t} + \nabla \cdot \boldsymbol{V} q_m = F_{Q_m} \tag{2.8}$$

in which the Right Hand Side (RHS) F terms include flux contributions depending on the parametrised physics, Coriolis terms, mixing terms, etc. The conserved variables are:

- $\boldsymbol{V} = \mu \boldsymbol{v} = \mu(u, v, w) = (U, V, W)$ where u and v are the horizontal covariant velocities, and $w = \partial\eta/\partial t$ is the vertical contravariant velocity.
- $\Theta = \mu\theta$ where θ is the potential temperature.
- $\mu(x, y)$ is the column of dry-mass per unit area at (x, y).
- $Q_m = \mu q_m$ where $q_m = q_v, q_c, q_i, ...$ are the mixing ratios of water vapour, cloud, rain, ice, etc.

and the non-conserved variables are:

- p is the pressure
- $\phi = g\,z$ is the geopotential
- α is the inverse of the full parcel density $(1/\rho)$ as $\alpha = \alpha_d(1 + q_v + q_c + q_i + ...)^{-1}$ where α_d is the inverse of the dry-air density $(1/\rho_d)$

In addition, there are the α_d diagnostic equation and the p diagnostic relation that read as:

$$\begin{aligned} \frac{\partial\phi}{\partial\eta} &= -\alpha_d\,\mu \\ p &= p_0\left(\frac{R_d\,\theta_m}{p_0\,\alpha_d}\right)^{\gamma} \end{aligned}$$

where R_d is the gas constant for dry air, p_0 is the reference pressure, $\gamma = c_p/c_v = 1.4$ is the ratio of the heat capacities of dry air and $\theta_m = \theta\,(1 + (R_v/R_d)q_v) \approx \theta(1 + 1.61q_v)$.

The WRF-ARW solves this system of equations using perturbation variables to reduce truncation errors in the horizontal pressure gradient in the discrete solver and machine rounding errors in the vertical pressure gradient and buoyancy calculations [Skamarock et al., 2008]. The model is solved using staggered finite differences schemes on an horizontal Arakawa C-grid. The temporal integration uses an explicit third-order Runge Kutta time integration scheme for low frequency modes and a smaller time step for high-frequency acoustic modes [Wicker, Skamarock, 2002; Klemp et al., 2007].

2.1.2 Physical parameterisations

The WRF-ARW system provides a list of physical options that can be classified into microphysics, cumulus, land-surface, PBL and radiation models. The coupling with the governing equations is made by computed tendencies for the velocity components, potential temperature and moisture fields, that are included in the RHS terms of equations (2.2)-(2.8). The selection of most suitable schemes for a concrete case depend on various aspects like; the climatology of the region simulated, the specific phenomena, the grid resolution, etc. Table 2.1 shows the physical parameterisations adopted during the this thesis.

Table 2.1
Physical parametrization used in WRF-ARW simulations.

Parametrization	**Scheme**	**Reference**
Microphysics	WRF single-moment 6-class (WSM6)	[Hong, Lim, 2006]
Cumulus	Modified Kain-Fritsch (KF) (*disabled in 1GRD*)	[Kain, 2004]
Surface Layer*	MM5 Monin-Obukhov (MM5) Eta Monin-Obukhov (Eta)	[Janjić, 1996, 2001]
Land Surface	Unified Noah Land Surface Model (LSM)	[Chen, Dudhia, 2001]
Planetary Boundary Layer*	Younsei University PBL (YSU)	[Hong et al., 2006]
	Mellor Yamada Janjic (MYJ)	[Janjić, 1994, 2001]
Long-wave Radiation	Rapid Radiative Transfer Model (RRTM)	[Mlawer et al., 1997]
Short-wave Radiation	Dudhia	[Dudhia, 1989]

* *This thesis uses two different PBL schemes with the Surface Layer scheme recommended.*

Microphysics packages include explicitly resolved water vapor, cloud and precipitation processes, and account for sedimentation and saturation. Microphysics schemes are applied at the end of each time step as an adjustment process and without providing tendencies to the dynamics governing equations. The WSM6 scheme predicts six categories of hydrometeors; vapour, rain, snow, cloud ice, cloud water and graupel with its associated processes.

Cumulus packages model the sub-grid scale effects of convective and/or shallow clouds. Thus, these parameterisations should not be used when the WRF model can resolve the convective eddies (resolutions below 3 km in our case). The modified KF scheme is a simple mass-flux 1D cloud model for the vertical fluxes due to the moist updrafts and downdrafts, also including entrainment and detrainment effects.

Surface Layer packages provide thermal stability-dependent information to the Land Surface and PBL schemes that are used to calculate surface heat and moisture fluxes. Each surface layer model is tied to a PBL scheme and does not provide tendencies. The MM5 and the Eta schemes are based on the Monin-Obukhov similarity theory (MOST) [Monin, Obukhov, 1954] and are tied to YSU and MYJ PBL schemes respectively.

Land Surface packages are 1D column models that deal with thermal and moisture fluxes in multiple soil layers. These models gather information from the surface layer, radiative and PBL schemes together with land-surface properties to primarily provide bottom boundary conditions (*i.e.* sensible and latent heat fluxes) for the PBL schemes. The LSM scheme is a four-layer (10, 30, 60, 100 cm from the top down) soil temperature and moisture model that deals with canopy moisture and snow cover considering evapotranspiration, soil drainage, vegetation categories, etc.

Planetary Boundary Layer packages are 1D models that provide source terms (tendencies) to the horizontal momentum, temperature and moisture in the entire atmospheric column. These schemes model the vertical sub-grid scale fluxes due to eddy transports, *i.e* in the WRF model explicit vertical diffusion is deactivated.

The **YSU scheme** is a non-local one order closure based on the K-theory. It approximates turbulent fluxes (second order moments) of a quantity β with the vertical gradient of its mean profile multiplied by an eddy diffusivity (or eddy viscosity) coefficient K as

$$\left(\overline{w'\beta'}\right) = -K\frac{\partial\overline{\beta}}{\partial z}$$

where K (for momentum K_m) is paramteterised as

$$K_m = \kappa\,\omega_s\,z\left(1-\frac{z}{h}\right)^2$$

where ω_s is the velocity scale, κ is the von Karman constant, z is a given height above the surface and h the PBL height. YSU scheme also adds a non-local gradient term to account for large eddies and an explicit treatment of the entrainment layer at PBL top.

The **MYJ scheme** is a local 1.5 order closure also based on the K-theory where K takes the form

$$K = \alpha\,l\,S\sqrt{k}$$

where α is a non-dimensional coefficient, l is the turbulence mixing length, S is the inverse of a stability function and k is the TKE defined as

$$k = \frac{1}{2}\sum_i \overline{u_i'u_i'}$$

The scheme can also be called a one-equation turbulence model because it solves a prognostic equation for the TKE like (with no horizontal advection) [Janjić, 2001]:

$$\frac{\partial k}{\partial t} - \frac{\partial}{\partial z}\left(l\,q\,S_q\frac{\partial k}{\partial z}\right) = P_k + G_k - \varepsilon \tag{2.9}$$

where $q = \sqrt{2k}$, $S_q = 0.2$, P_k and G_k are the shear and buoyancy TKE production terms respectively as

$$P_k = -\left(\overline{w'u'}\right)\left(\frac{\partial U}{\partial z}\right) - \left(\overline{w'v'}\right)\left(\frac{\partial V}{\partial z}\right) = K_m\left[\left(\frac{\partial U}{\partial z}\right)^2 + \left(\frac{\partial V}{\partial z}\right)^2\right] \tag{2.10}$$

$$G_k = -\frac{|\boldsymbol{g}|}{\theta_{v0}}\left(\overline{w'\theta'_v}\right) = -K_h\frac{|\boldsymbol{g}|}{\theta_{v0}}\left(\frac{\partial \theta_v}{\partial z}\right) \tag{2.11}$$

and ε is the TKE dissipation expressed as

$$\varepsilon = \frac{k^{3/2}}{B\,l} \tag{2.12}$$

where B is a constant and the mixing length l is calculated with the diagnostic formula of the form [Janjić, 2001]:

$$l = l_{max}\frac{\kappa z}{\kappa z + l_{max}} \tag{2.13}$$

$$l_{\max} = \beta\frac{\int_0^\infty z\sqrt{k}dz}{\int_0^\infty \sqrt{k}dz} \tag{2.14}$$

where l_{max} is the maximum mixing length, κ is the von Karman constant and β an empirical constant.

2.1.3 Boundary conditions

The boundaries of the computational domain are classified into bottom, top, and lateral:

- **The bottom boundary** conditions are provided by physics of the land and surface packages previously introduced. These models are all based on MOST [Monin, Obukhov, 1954] and incorporate different similarity stability functions accounting for the different stability regimes. From MOST, the surface (s) fluxes for momentum and heat are of the form

$$\left[\left(\overline{u'w'_s}\right)^2 + \left(\overline{v'w'_s}\right)^2\right]^{1/2} = \frac{\overline{\boldsymbol{u_1}}^2\kappa^2}{\left[\ln\left(1+\frac{z}{z_0}\right) - \Psi_m\left(\frac{z}{L}\right)\right]^2} = u_*^2 \tag{2.15}$$

$$\left(\overline{w'\theta'}\right)_s = \frac{u_*\left(\overline{\theta_1} - \overline{\theta_s}\right)}{\left[\ln\left(1+\frac{z}{z_0}\right) - \Psi_h\left(\frac{z}{L}\right)\right]} \tag{2.16}$$

where $\overline{\boldsymbol{u_1}} = \sqrt{\overline{u_1} + \overline{v_1}}$ is the wind velocity prescribed at the first model level, z_0 is the roughness length and the quantity u_* is called friction velocity. The terms $\Psi_m\left(\frac{z}{L}\right)$ and $\Psi_h\left(\frac{z}{L}\right)$ are stability functions where $\frac{z}{L}$ is a stability parameter and L is the Obukhov length

$$L = -\frac{\left[\left(\overline{u'w'_s}\right)^2 + \left(\overline{v'w'_s}\right)^2\right]^{3/4}\overline{\theta_v}}{\kappa g\left(\overline{w'\theta'_v}\right)_s} \tag{2.17}$$

- **The top boundary** is a constant pressure level with different gravity wave absorbing options: diffusion, Rayleigh damping, or implicit Rayleigh damping for vertical velocity.

- **The lateral boundary** is specified by, and relaxed (or nudged) towards larger scale forecasts or analysis. The larger scale fields can be supplied by the preprocessor (WPS) in the case of the outer-most domain, or directly by the nested parent grids. The specification and relaxation combination comprehends 3 different grid regions: the outer-most grid points have the unknowns of the prognostic equations specified; in the following inward grid points (commonly 5 grid points are involved), the model is relaxed towards the larger-scale forecasts using linear weighted functions; and the inner region for the model development.

2.2 Alya-CFDWind microscale model

Alya-CFDWind [Avila et al., 2013, 2017] is a CFD model for the ABL based on the RANS equations and a κ-ε turbulence model. The model considers the flow as incompressible and isothermal (neutral stability), the Coriolis effects with a consistent limitation of the mixing length, and a wall law for atmospheric boundary layers. The wind model is implemented in Alya, an in-house HPC multiphysics parallel solver based on the finite element method [Vázquez et al., 2016; Houzeaux et al., 2009]. Alya-CFDWind is routinely used in the context of wind energy to solve atmospheric flows in complex terrains, and incorporates the possibility to model the wake effects of wind turbines using the actuator disc theory [Avila et al., 2017].

2.2.1 Alya-CFDWind governing equations

The Alya-CFDWind governing equations are the incompressible Reynolds Averaged Navier-Stokes (RANS) equations (2.18)-(2.19), together with a k-ε turbulence model (2.20)-(2.21). The model accounts for the Coriolis force and uses a consistent limitation of the mixing length [Apsley, Castro, 1997]. The resulting system of equations is:

$$\begin{aligned}
&\textbf{Mass eq.} && \nabla \cdot \boldsymbol{u} && = 0 && (2.18)\\
&\textbf{Momentum eq.} && \tfrac{\partial \boldsymbol{u}}{\partial t} + \boldsymbol{u}\cdot\nabla\boldsymbol{u} - \nabla\cdot(\nu_t \nabla^s \boldsymbol{u}) && = -\boldsymbol{\nabla} p - 2\boldsymbol{\omega}\times\boldsymbol{u} && (2.19)\\
&\textbf{TKE eq.} && \tfrac{\partial k}{\partial t} + \boldsymbol{u}\cdot\nabla k - \nabla\cdot\left(\tfrac{\nu_t}{\sigma_k}\cdot\nabla k\right) && = P_k - \varepsilon && (2.20)\\
&\textbf{TKE dissipation eq.} && \tfrac{\partial \varepsilon}{\partial t} + \boldsymbol{u}\cdot\nabla \varepsilon - \nabla\cdot\left(\tfrac{\nu_t}{\sigma_\varepsilon}\cdot\nabla \varepsilon\right) && = \frac{\varepsilon}{k}\left(C_1' P_k - C_2\varepsilon\right) && (2.21)
\end{aligned}$$

where the unknowns are the wind velocity vector $\boldsymbol{u}$, the pressure p, the turbulent kinetic energy k and its dissipation rate ε. The turbulent viscosity ν_t is given by

$$\nu_t = \frac{C_\mu k^2}{\varepsilon} \tag{2.22}$$

In the momentum equation, ∇^s refers to the symmetric gradient operator. The second term in the RHS of equation (2.19) is the Coriolis force term, being $\boldsymbol{\omega}$ the Earth's angular velocity. The coefficient C_1' in the RHS of equation (2.21) is a modified coefficient, originally proposed by Apsley, Castro [1997], to limit the mixing length (l_m) by a maximum (l_{max}) when accounting for Coriolis effects:

$$C_1' = C_1 + (C_2 - C_1)\frac{l_m}{l_{max}}$$

where l_m is defined as

$$l_m = C_\mu^{3/4}\frac{k^{3/2}}{\varepsilon} \tag{2.23}$$

and l_{max} for thermally neutral flows is computed as [Blackadar, 1962]

$$l_{\max} = 0.00027\frac{|\boldsymbol{u_g}|}{2|\boldsymbol{\omega}| sin\lambda} \tag{2.24}$$

with the latitude λ and the geostrophic wind velocity $\boldsymbol{u_g}$. The TKE production rate by mechanical shear (P_k) is:

$$P_k = 2\nu_t \boldsymbol{\nabla^s u} : \boldsymbol{\nabla^s u} \tag{2.25}$$

Finally, Table 4.1 shows the Alya-CFDWind coefficients:

Table 2.2
Alya-CFDWind model coefficients

κ	C_μ	C_1	C_2	σ_k	σ_ε
0.4	0.033	1.176	1.92	1.0	1.238

Chapter 4 presents the thermal model that has been implemented during this thesis and the new terms appearing in the governing equations to deal with the simulation of diurnal cycles.

2.2.2 Boundary conditions

The boundaries of the computational domain are classified as bottom, top, lateral inflow and lateral outflow.

- **On the bottom boundary**, wall law functions following the Monin-Obukhov similarity theory [Monin, Obukhov, 1954] are imposed for momentum and turbulence equations to remove a boundary layer of thickness δ_w above z_0. Thus, the wind velocity at distance δ_w from the ground is imposed as:

  $$|\boldsymbol{u}|(\delta_w) = \frac{u_*}{\kappa} \ln\left(1 + \frac{\delta_w}{z_0}\right) \tag{2.26}$$

  where u_* is the friction velocity ($u_*{=}(\tau_{wall}/\rho)^{1/2}$, with τ_{wall} being the shear stress at the bottom wall) and z_0 is the terrain roughness length. A zero diffusion through the wall is imposed for the turbulent kinetic energy ($\nabla k \cdot \boldsymbol{n}{=}0$, with $\boldsymbol{n}$ the normal vector to the wall) and the dissipation rate is imposed as:

  $$\varepsilon\left(\delta_w\right) = \frac{k^{3/2} {C_\mu}^{3/4}}{\kappa\left(\delta_w + z_0\right)} \tag{2.27}$$

- **On the top boundary**, symmetry boundary conditions (zero normal gradient to the wall) are imposed for the tangential velocity component, θ, k, and ε. The normal velocity component is fixed to zero (*i.e.* $\boldsymbol{u} \cdot \boldsymbol{n}{=}0$).

- **On the lateral inflow boundary**, vertical profiles for $\boldsymbol{u}$, θ, k and ε are imposed from a 1D precursor simulation (see Sect. 2.2.3) assuming uniform roughness and flat terrain.

- **On the lateral outflow boundaries**, symmetry boundary conditions are imposed for θ, k, and ε. For the momentum equation two options exist, to impose the geostrophic pressure and no shear stress or, to prescribe the vertical profiles (*i.e.* to impose Dirichlet conditions at outflow).

2.2.3 Preprocess

The Alya-CFDWind is part of a simulation framework that involves an automatic meshing tool, a preprocessing tool and a set of postprocessing routines. The meshing tool [Gargallo-Peiró et al., 2015; Avila et al., 2017] assimilates terrain information and generates structured meshes made of hexahedral elements. The meshes are specifically designed to simulate ABL flows over complex terrains and consist of three differentiated regions, namely: farm, transition and buffer zones. The farm zone comprehends the area of interest and contains the smaller elements to represent the topography and the roughness. The transition zone surrounds the farm zone; its elements grow gradually outwards and it also has the topography and roughness fields assimilated. Finally, the buffer is the outer-most zone; it has the coarser elements and it is flat to accommodate the inflow boundary conditions, and to avoid recirculation at the outflow boundary.

The preprocessing tool generates initial and boundary conditions consistent with the atmospheric boundary layer by means of a single column precursor model. This is a single-column (1D) simulator based on the Alya-CFDWind governing equations that assumes flat terrain and uniform roughness. The tool primarily uses the geostrophic wind velocity, wind direction and the latitude as input parameters for the precursor, together with the mesh information for the interpolation of the precursor solution.

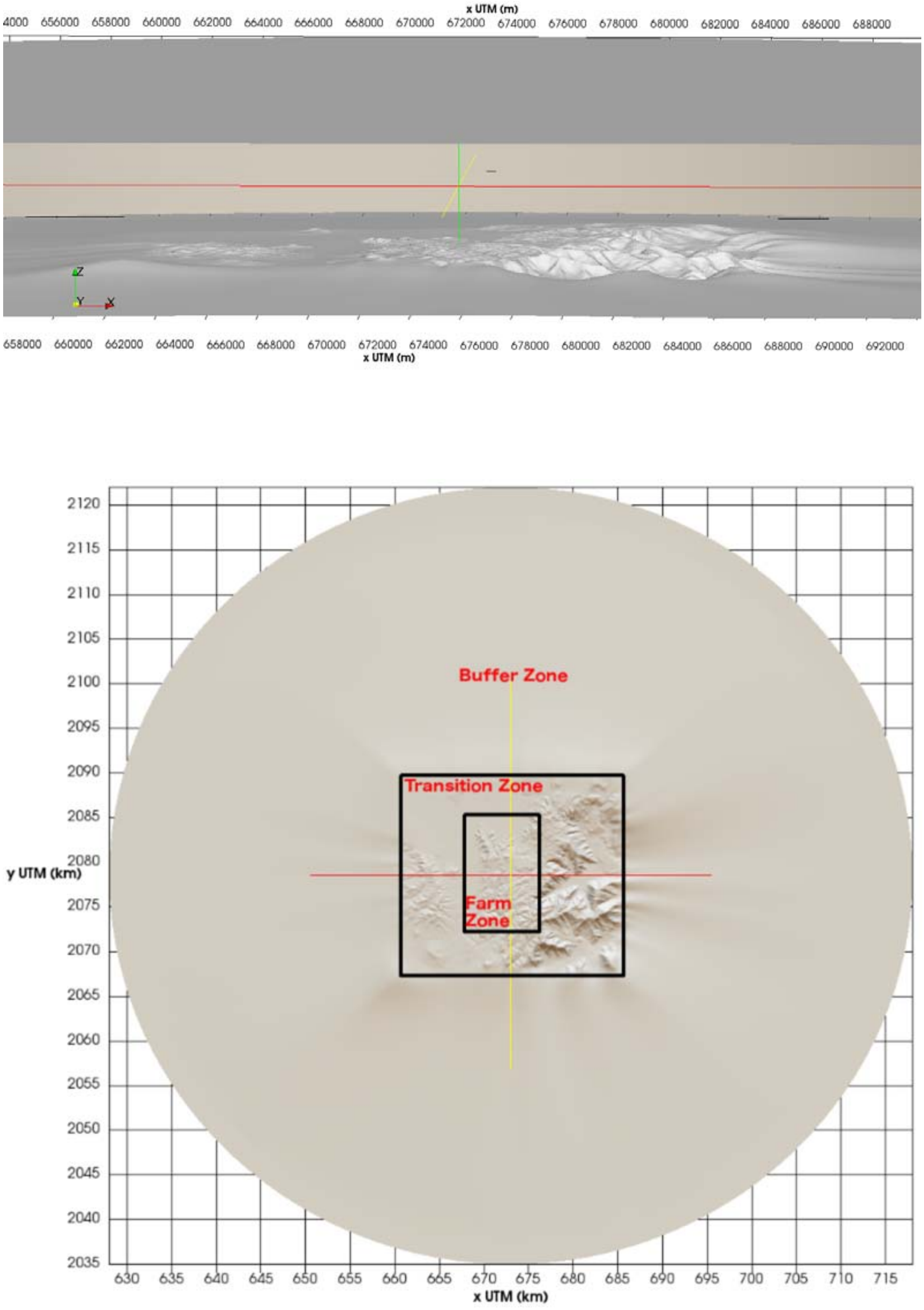

Figure 2.1
An example of one Alya-CFDWind computational domain with 3 different mesh zones identified: a 8×13 *km*^{2} *zone at 40 m horizontal grid resolution, a transition zone of 5 km at north and south and 8 km and 10 km at west and east respectively, and an external flat buffer zone.*

CHAPTER 3

Assimilation of surface automatic weather stations

This chapter is an elaboration of the material in

Barcons, J., Folch, A., Sairouní, A., Miró, J.R., 2015. Assimilation of surface AWS using 3DVAR and LAPS and their effects on short-term high-resolution weather forecasts. Atmos. Res. 156, 160-173; doi:10.1016/j.atmosres.2014.12.019

3.1 Introduction

Conventional observational data from surface Automatic Weather Stations (AWS) is a valuable in-situ high-frequency source of information for weather forecast [Warner, 2011]. However, the assimilation of surface observations into numerical weather prediction (NWP) models remains challenging despite the important advances in meteorological Data Assimilation (DA) [Pu et al., 2013]. The spatial-density of a network and the spatial resolution of a model are crucial in the DA process [Müller, 2011]. In the case of complex terrains, the difficulties increase as the model better represents the topography (the higher the resolution of the model the larger the number of terrain effects explicitly resolved). Such difficulties could be alleviated with denser observational networks, but the number of AWS needed is unaffordable. As a result, AWS representativity and correlation problems arise and have no trivial solutions.

The representativity of each AWS of a network varies depending on its location, surroundings, altitude and synoptic characteristics at the time of assimilation. For example, consider the case of two different stations, one in a valley and the other at a mountain top. Even if both can give valuable information of the region, some anisotropic surface analysis is needed to reflect terrain complexities [Deng, Stull, 2005, 2007]. Intuitively, one may expect that working with higher-resolution regional models and assimilating AWS capturing local characteristics would produce an improvement of the model analyses. However, some aspects need to be considered, including the spread of information by the DA schemes [Daley, 1991] (controlled by setting parameters related to the radius of influence of the stations, which may overlap), the correlation between points inside the domain and the different variables and, for some DA schemes, the introduction of effects related to inhomogeneities of the terrain.

Since 2008, the Meteorological Service of Catalonia (SMC) runs operationally the WRF model and at present, at 3 km horizontal grid resolution. Two different meteorological DA systems are used at SMC, the WRF three-dimensional variational (3DVar) analysis [Daley, 1991; Barker et al., 2003, 2004] and the Local Analysis and Prediction System (LAPS) [McGinley et al., 1991; Albers, 1995; Albers et al., 1996] (information available online at http://laps.noaa.gov/). Operationally, observational data from satellites, radars, soundings and metars are assimilated using LAPS system and only metars and soundings with 3DVar. However, data from the existing dense network of surface AWS called XMET is not assimilated during operational forecasts yet. Actually, SMC is making efforts to run forecasts at 1 km grid resolution and to assimilate data from the XMET network into the WRF model, keeping in mind computational cost constraints on future operational applications and services.

This Chapter evaluates and compares the ability of WRF-3DVar and LAPS to assimilate surface AWS only on high-resolution model domains. Knowing that the AWS representativity could go from synoptic to local and that the spatial-density of the AWS network varies, the goal is to understand how both systems deal with this type of observational data. Likewise, the aim is to find the most suitable DA system for operational applications around 1 km grid resolution for temperature and wind forecasts. More sophisticated DA methods such as those based on Ensemble Kalman Filters (EnKF) (for example, Stensrud et al. [2009]) or four-dimensional variational analysis (4DVAR) are not considered because of their higher computational cost [Warner, 2011], even if some studies (for example, Pu et al. [2013]) conclude that EnKF outperforms 3DVar.

Section 3.2 presents the WRF-3DVar and LAPS DA systems. Section 3.3 presents the methodology that is used to compare and validate both DA systems. This section starts the comparison with two cases of study; the assimilation of one AWS, and the complete assimilation of the XMET in one concrete day. Finally, Section 3.4 presents the results for the set of 29 common mesoscale meteorological cases in the region of Catalonia.

3.1.1 The XMET surface AWS network

The region of Catalonia, on the north-east of the Iberian Peninsula, covers an area of 32.114 km^2, extending from Pyrenees to Mediterranean sea. The XMET network of the SMC contains a total of 159 AWS across the region (Fig. 3.1), resulting on a mean coverage per AWS of 202 km^2. The basic data provided by the stations are 10-m wind velocity (WV10m) and direction (WD10m), 2-m temperature (T2m), 2-m relative humidity (RH2m), precipitation, surface pressure (Psfc) and global solar radiation. Some of the stations, those deployed for agricultural applications, also register 6-m and 2-m winds. In these cases, a wind data extrapolation up to 10 m height is done using a power law [Justus, Mikhail, 1976] in order to have an homogeneous dataset. The data quality is routinely verified in order to guarantee that the sensor equipments work correctly. Checks and calibrations establishing the corresponding error ranges are done periodically. In addition, data passes a quality control consisting on various hierarchical semi-automatic processes of verification, checking that data is within a certain threshold and that the temporal evolution at any station is consistent and coherent with records from other neighboring stations.

3.2 Data assimilation schemes

3.2.1 The WRF-3DVar system

The WRF-3DVar system was developed primarily at the National Center for Atmospheric Research (NCAR) based on the Fifth Generation NCAR / Penn State Mesoscale Model (MM5) 3DVar system [Barker et al., 2004]. The DA builds on a multivariate incremental analysis system. Given the background ($\boldsymbol{x_b}$) and the observational ($\boldsymbol{y_o}$) vectors, the goal is to find an optimal estimate of the atmosphere (the analysis $\boldsymbol{x_a}$) minimizing the cost function $J(\boldsymbol{x})$ [Barker et al., 2003]:

$$J(\boldsymbol{x}) = J_b + J_o = \frac{1}{2}(\boldsymbol{x} - \boldsymbol{x_b})^T \boldsymbol{B}^{-1}(\boldsymbol{x} - \boldsymbol{x_b}) + \frac{1}{2}(\boldsymbol{y} - \boldsymbol{y_o})^T \boldsymbol{O}^{-1}(\boldsymbol{y} - \boldsymbol{y_o}) \tag{3.1}$$

where J_b and J_o represent background and observational terms respectively, $\boldsymbol{y}$ is the observation vector analysis that corresponds to $\boldsymbol{y} = H(\boldsymbol{x})$ ($H(\boldsymbol{x})$ is an operator used to transform the model grid points analysis $\boldsymbol{x}$ to observational space), and $\boldsymbol{B}$ and $\boldsymbol{O}$ are the background and observation error covariance matrices respectively. The minimization procedure changes $\boldsymbol{x}$ iteratively in order to approach the (unique) minimum of $J(\boldsymbol{x})$ and, as a result, the analysis $\boldsymbol{x_a}$. This quadratic representation of the cost function assumes that the observation and background error covariances can be described using Gaussian probability density functions with zero mean error [Barker et al., 2003]. Model errors are neglected and the background and observation errors are assumed uncorrelated. Details on $\boldsymbol{B}$ calculation are given in Section 3.3.1.

3.2.2 The LAPS system

LAPS, developed by the National Oceanic and Atmospheric Administration's (NOAA) Earth System Research Laboratory (ESRL), is a meteorological DA tool that employs available observations (radar, satellite, meteorological networks, soundings, aircraft, etc.) to generate a spatially distributed, three-dimensional representation of atmospheric features and allows to create multi-instrument analysis fields that serve as initial condition in NWP models. The system is currently operated in different centers worldwide. Deserves special mention the European LAPS (ELAPS) community with several institutes and universities participating. Its main members are the Institute of Atmospheric Sciences and Climate (ISAC) of the Italian National Research Council (CNR), the Finnish Meteorological Institute (FMI) in Finland, the Harokopio University of Athens in Greece, or the Meteorological Service of Catalonia (SMC) in Spain.

The analysis provided by LAPS includes wind speed, wind direction, surface temperature, relative humidity, surface pressure, cloud cover and hydrometeor fields, among others. The assimilation process is the result of a complex cycle of ingesting and merging measurements from all the available sources of meteorological information in a computationally efficient manner [Lazarus et al., 2002]. The system is flexible and modular, and depending on the analysis and the sources of data, different analysis procedures can be followed with additional steps and variants to incorporate and blend the observational data into the analysis.

In particular, regarding surface wind and temperature analysis (the fields under study here), LAPS interpolates first the first-guess to its grid. If the first-guess is in a coarser grid than LAPS, a downscaling is performed giving to the fields the reasonably fine-scale terrain-related structure. The terrain-related structures are retained by performing the analysis in an incremental space [Hiemstra et al., 2006]. Before the analysis itself, observations also pass a quality control, where observations exceeding a threshold from background field, are rejected. After this, the analysis is independently performed for each variable following a telescoping successive correction process until the fine-scale structure and the fit to observations is achieved at a desired level of agreement, which is set to the typical instrumental error [Albers, 1995]. In each iteration, the result of the previous one becomes the new background and a modified Barnes scheme [Barnes, 1964] is employed to combine observation increments with the updated background. The Barnes analysis could be described as an interpolation method that relies on a weighting function and the definition of a radius of influence for the observations. Finally, a variational minimization procedure of a cost function is applied to dynamically adjust the wind and pressure fields. In the cost function, one can tune some quantities controlling the relative adjustment of the wind with respect to pressure, and how close the analysis satisfies the equation of motion [McGinley et al., 1991].

3.3 3DVar and LAPS comparison

3.3.1 Methodology

WRF-ARW model set-up

Here we used the version 3.4.1 of the dynamical solver Advanced Research WRF (WRF-ARW) (introduced in Section 2.1) with the physical parameterizations and schemes summarized in Table 3.1. The computational domain is composed of one parent domain at 9 km (9GRD) horizontal grid resolution and two (one-way) nests of 3 km (3GRD) and 1 km (1GRD) resolution respectively (Fig. 3.1). The coarse domain covers the Iberian Peninsula and its design was the result of a compromise between computational cost and the need to avoid complex orography across the borders (i.e. the Alps). The first nest covers Catalonia and is the region under surveillance by the SMC. These two domains coincide with the current operational configuration at SMC. Finally, the inner domain covers the south of Catalonia and is used here to test DA of AWS in a high-resolution domain. All domains have 60 vertical levels with a higher resolution within the boundary layer and a top model pressure of 70 hPa (18.5 km roughly). The initial and boundary conditions come from the European Centre for Medium-Range Weather Forecasts (ECMWF) deterministic model at 0.125 degree resolution. The simulations are carried out up to 24 h forecast and three different sets of runs are distinguished: CNTRL-runs (without DA), and 3DVar-runs and LAPS-runs initialized with analyses resulting for WRF-3DVar and LAPS respectively.

Table 3.1
Configuration and physical parametrization used in the CNTRL-runs, 3DVar-runs and LAPS-runs WRF-ARW simulations.

WRF-ARW configuration	
Version	3.4.1
Initial and Lateral BC's	ECMWF model at 0.125degree resolution
Domains	9GRD, 3GRD, 1GRD
Horizontal resolution	9 km, 3 km, 1 km
Horizontal grid size	166x115, 166x154, 100x94
Vertical levels	60 levels, with top at 70hPa
Length simulation	24 hours
Time step	30 s, 10 s, 2 s
Parametrization	**Scheme**
Microphysics	WRF single-moment 6-class (WSM6) [Hong, Lim, 2006]
Cumulus	Modified Kain-Fritsch (disabled in 1GRD) [Kain, 2004]
Surface Layer	MM5 Monin-Obukhov
Land Surface	Unified Noah Land Surface Model (LSM) [Chen, Dudhia, 2001]
Planet Boundary Layer	Younsei University PBL (YSU) [Hong et al., 2006]
Long-wave Radiation	Rapid Radiative Transfer Model (RRTM) [Mlawer et al., 1997]
Short-wave Radiation	Dudhia [Dudhia, 1989]

Data assimilation

Observational data is assimilated at the initialization time for 3GRD and 1GRD. No DA is done for the 9GRD domain because the attention is focused on the high-resolution domains and because the XMET network covers only the region of Catalonia. The fields from AWS assimilated are WV10m, WD10m, T2m, RH2m and Psfc.

As explained previously, in WRF-3DVar the background error covariance matrix $\boldsymbol{B}$ is used in the cost function to weight model-scale-dependent errors in the background field. This matrix influences the analysis adjustment to observations and the spread of data over the domain. This spread is also determined by recursive filters [Purser et al., 2003] using the length scale parameters derived from the National Meteorological Center (NMC) method [Parrish, Derber, 1992], specified for each variable in each vertical mode. In addition, WRF-3DVar offers the opportunity to tune $\boldsymbol{B}$ using some scaling parameters.

In general, it is very difficult to obtain an accurate background error covariance. As proposed in Barker et al. [2004] and following Parrish, Derber [1992] NMC method, statistical approaches have been applied to obtain covariance estimations. The method assumes that the background is an unbiased random vector representing the true atmosphere, and forecast differences are tipically used

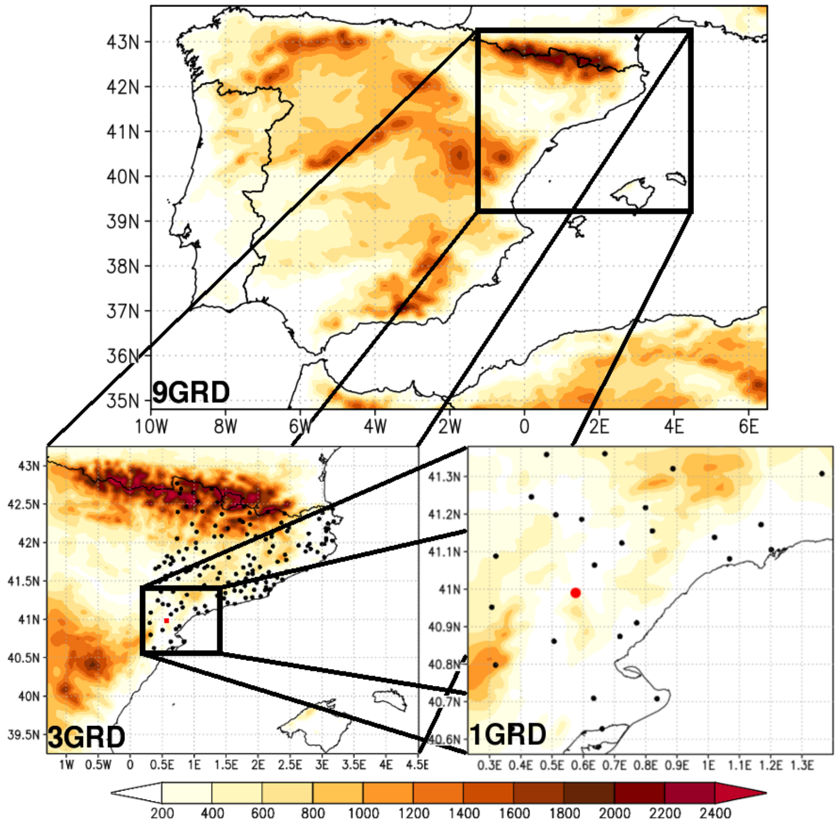

Figure 3.1
Extent of the parent (9GRD) and nested (3GDR and 1GRD) WRF-ARW computational domains. Black dots indicate the AWS of the XMET network. Red dot indicate an independent AWS of the AEMET network. Shaded contours show terrain elevation at 200-m intervals.

to estimate forecast errors. These forecast differences can be computed by subtracting one forecast from another valid at the same time and they can be time-lagged, initial or boundary perturbed, or different model ensemble forecasts [Xie et al., 2011]. Here, $\boldsymbol{B}$ has been obtained climatologically, for each domain with a year-long (2010) series of 24 hour minus 12 hour forecasts valid at the same time. An important shortcoming of the NMC method is that the spatial correlated scales are excessively large. As a consequence, small-scale observed details tend to be filtered out in the analysis and locally observed information is propagated over large spatial distances [Ha, Lee, 2012].

In the case of LAPS, no previous calculation of the background error covariance matrix is needed. The system provides the possibility to tune a wide range of parameters related with the analysis. Recalling Section 3.2.2, there is the possibility to define a radius of influence and, in some cases, the weighting factor for the Barnes analysis, as well as the fitting thresholds to the observations within the successive telescoping correction process. Other important parameters to consider are those affecting the variational minimization and its constraints to the equation of motion.

Taking into account the domain features and the data assimilated in this work (surface AWS), a tuning process for the parameters previously mentioned in both DA systems was conducted. In

WRF-3DVar, a factor of 0.5 for the length scaling parameters showed the best results. In the case of LAPS, the optimal configuration for the 1GRD entailed the following modifications of the parameters:

- *3D wind analysis:*a reduction of the observations radii of influence down to 15 km, 2.1 ms^{-1} of fitting threshold and an important reduction of the background weight (compared to the default).

- *surface analysis:* values for the fitting thresholds of 1.5 ms^{-1} for wind and 1.5°C for temperature and a weak constrain in the variational analysis to the equation of motion.

- *3D temperature analysis:* 2.2 °C of fitting threshold.

- *variational balance:* It is a three-dimensional dynamical adjustment between mass and momentum to force the consistency with the diagnosed cloud vertical motions [McGinley, Smart, 2001]. It is specially focused on the improvement of the cloud analysis and it is supposed to improve other fields for model initialization. However, here it is deactivated because some tests comparing balanced and unbalanced analyses revealed that this option worsens the final fitting of wind and temperature fields to observation. Moreover, the spin-up process of the WRF-ARW model initialization was not reduced significantly when using the balancing procedure.

Validation metrics

In order to validate the performance of the DA systems, a set of 29 Common Mesoscale Meteorological Cases (CMMC) occurring within the region of Catalonia (Table 3.2) has been constructed at SMC. Firstly, a qualitative evaluation of the analysis increments is shown in Section 3.3.2 for the case number 27 of the CMMC (Table 3.2). This case is representative of a common north-westerly advection event with strong winds at surface and is useful to study the ability of both DA systems to reproduce very local effects like wind channelling. To accomplish this evaluation, first model level temperature, wind components and vertical cross-section of wind module fields, with the respective background field subtracted, were used. The background is ECMWF model fields interpolated into the WRF mesh by the WRF-ARW pre-process system. This approach is firstly used for the assimilation of only one station located in the innermost domain (1GRD), and followed by all the stations of XMET network later on.

Further, in order to be able to quantify the accuracy of the CMMC forecasts and to validate them, the root mean square error (RMSE) is computed for each variable as follows:

$$RMSE = \sqrt{\frac{1}{n}\sum(y_i - x_i)^2} \tag{3.2}$$

where n is the number of AWS, y_i is the station value and x_i is the WRF modelled variable at the grid point closest to the station. As 1GRD domain covers a small region, the stations used to calculate the forecast RMSEs are the same 31 stations (Fig. 3.1) that are being assimilated at the initial time. Additionally, with the purpose to validate with independent data, we also consider an independent AWS (red dot in Figure 3.1) managed by the Spanish Meteorological Agency (AEMET). As stated in Müller [2011], a reduction of raw model output temperature and wind speed errors are expected due to the increase in resolution.

Table 3.2
Summary of the 29 Common Mesoscale Meteorological Cases (CMMC) in the region of Catalonia. Cases are ordered chronologically by its occurrence during 2010.

Num.	Date	Case Description
1	11/02/2010	North-easterly dry advection, with drop in temperatures
2	22/02/2010	West front arrival with low rainfall
3	08/03/2010	Snowfall over shoreline
4	16/03/2010	Anticyclonic conditions dominated by stable weather
5	19/03/2010	Two fronts passing with low rainfall
6	03/04/2010	West front arrival with low rainfall on the north-east
7	10/04/2010	Anticyclonic conditions
8	03/05/2010	Rainfall event with a low in front the shoreline
9	12/05/2010	Rainfall event with a low in front the shoreline
10	22/05/2010	Convective event
11	05/06/2010	West front arrival
12	09/06/2010	Rainfall on the South-west
13	23/06/2010	Summer sea breeze circulation
14	15/07/2010	Isolated storms over mountainous zones
15	23/07/2010	Atmospheric instability
16	05/08/2010	Convective event with storms arriving from the coast
17	12/08/2010	Convective event with storms spread out
18	26/08/2010	Warm air arrival
19	14/09/2010	Anticyclonic conditions
20	17/09/2010	General rainfall event
21	27/09/2010	Atmospheric instability
22	09/10/2010	Rainfall event
23	12/10/2010	Rainfall event
24	22/10/2010	A weak frontal line passing
25	25/10/2010	North-easterly dry advection, with a drop in temperatures
26	04/11/2010	Anticyclonic conditions with high temperatures
27	16/11/2010	North-westerly advection and a frontal system passing
28	12/12/2010	Persistent fog over the central depression
29	22/12/2010	West to east traveling perturbation

3.3.2 DA pattern comparison

Assimilation of one AWS

We start comparing the effects of WRF-3DVar and LAPS for a single AWS. Table 3.3 shows the differences between ECMWF analysis and observations, at the station of *El Perelló* (40.87° N, 0.72° E, 158.2 m over mean sea level) for the case number 27 of the CMMC. As observed, large differences in wind module (up to 10 ms^{-1}) existed locally, probably because of topographic channelling effects unresolved by the global model.

Table 3.3
Differences in temperature and wind components between the ECMWF analysis interpolated at 3GRD and 1GRD and observations at the station point of El Perelló during 16th November 2010 at the time of the analysis.

Resolution(km)	T($^{\circ}$C)	u(ms^{-1})	v(ms^{-1})
3	-0.033	-2.898	-9.665
1	-0.026	-2.644	-9.610

Starting with WRF-3DVar, Figure 3.2 shows the analysis increments on temperature and wind components for 3GRD and 1GRD at the first model vertical level. For 3GRD, only the region coinciding with 1GRD is shown in order to highlight the differences coming from the mesh resolution. Two conclusions emerge from inspection of Figure 3.2. Firstly, the WRF-3DVar contours of increments are very homogeneous, reminding large-scale features. This fact is unrealistic in complex terrains given the inhomogeneous nature of the near-surface fields and the data assimilated. Secondly, the shape of the WRF-3DVar analysis increments for each variable is approximately the same in both grids. This effect is due to the strong dependence on the prescribed correlation function in the background error covariance term [Pu et al., 2013]. For comparison, the LAPS analysis increments are shown in Figure 3.3. Before analyzing the pattern of increments, it is important to point out that the background fields subtracted are the result of a downscaling pre-process that incorporates the effects of the higher resolution topography to the temperature fields (increasing and decreasing temperature given the difference in terrain height). As observed, LAPS produces lower increments with height than the background and, therefore, it is warmer in the higher and colder in the lower regions. It also produces a global mean increment of the wind components over the whole domain that is proportional to the value of the observation and background differences (Table 3.3). This is directly related to the decrease of the background weight and despite of the predefined small length scale.

Similar conclusions can be drawn for the analysis increments along the vertical (Fig. 3.4).

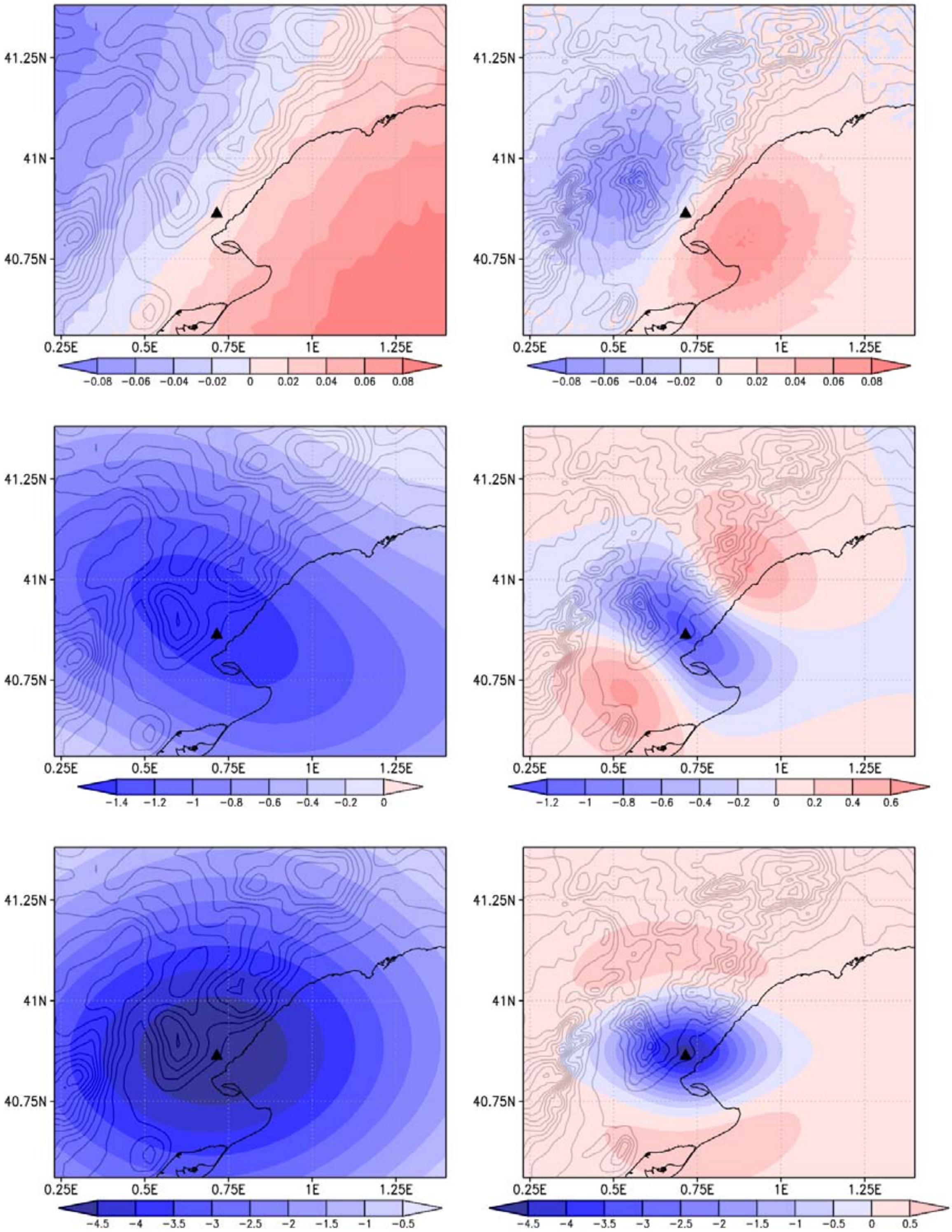

Figure 3.2

Analysis increment after assimilation of 1 AWS using WRF-3DVAR. Results show, from top to bottom, increments on temperature (°C) and wind components (longitudinal and latitudinal) (ms^{-1}) at the first model level for 3GRD (first column) and 1GRD (second column). For 3GRD, only the region overlapping 1GRD is shown. The location of the AWS, near the village of El Perelló, is indicated by a triangle. Black contours indicate elevation using a 100-m contour interval.

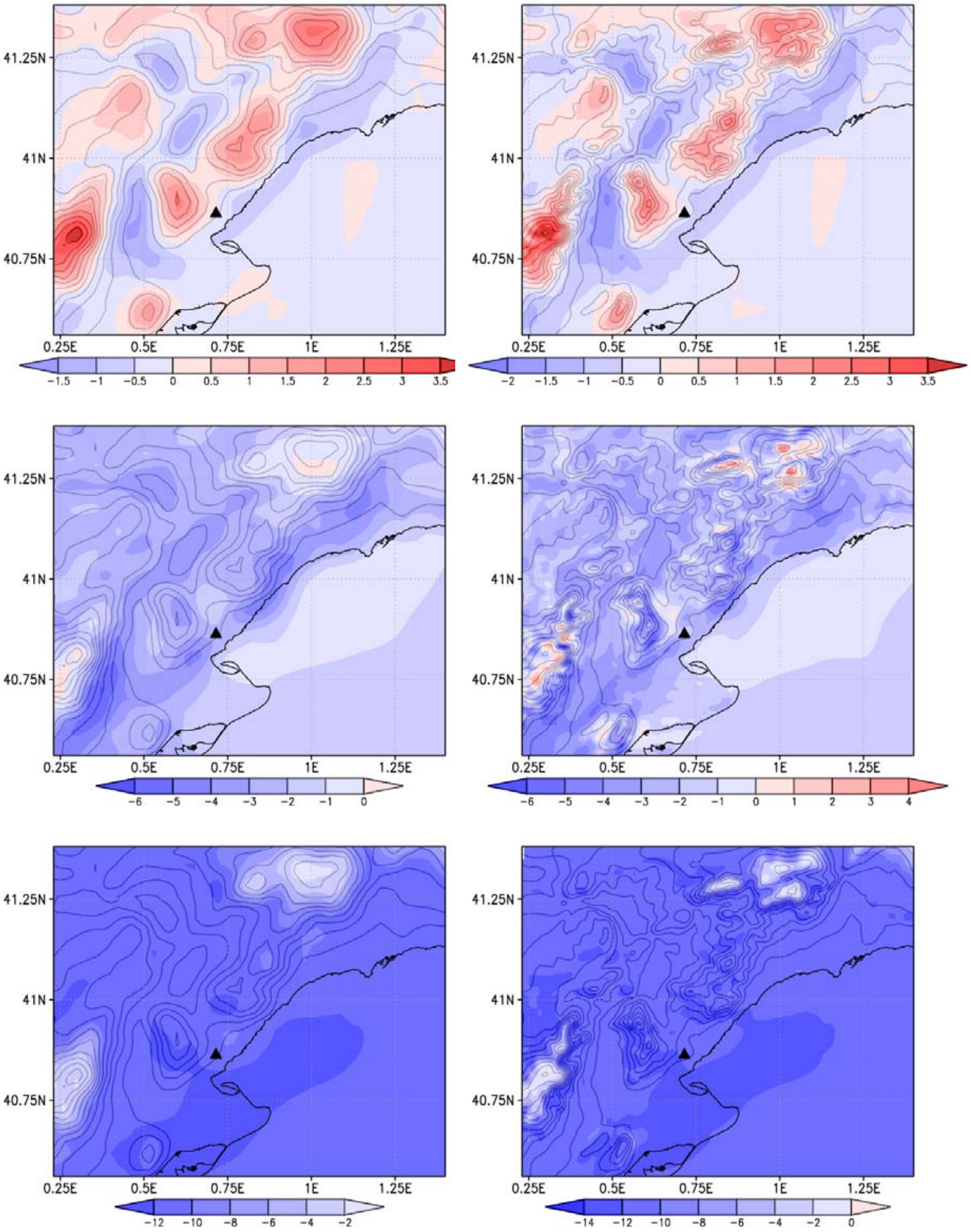

Figure 3.3

Analysis increment after assimilation of 1 AWS using LAPS. Results show, from top to bottom, increments on temperature (°C) and wind components (longitudinal and latitudinal) (ms^{-1}) at the first model level for 3GRD (first column) and 1GRD (second column). For 3GRD, only the region overlapping 1GRD is shown. The location of the AWS, near the village of El Perelló, is indicated by a triangle. Black contours indicate elevation using a 100-m contour interval.

The vertical cross-section of wind analysis increments using WRF-3DVar shows an homogeneous grid-dependent pattern similar to that of the horizontal spread (Fig. 3.2). In contrast, the LAPS cross-section of wind analysis increments are less grid resolution dependent and reflects terrain effects, reducing significantly the value of the increments uphill.

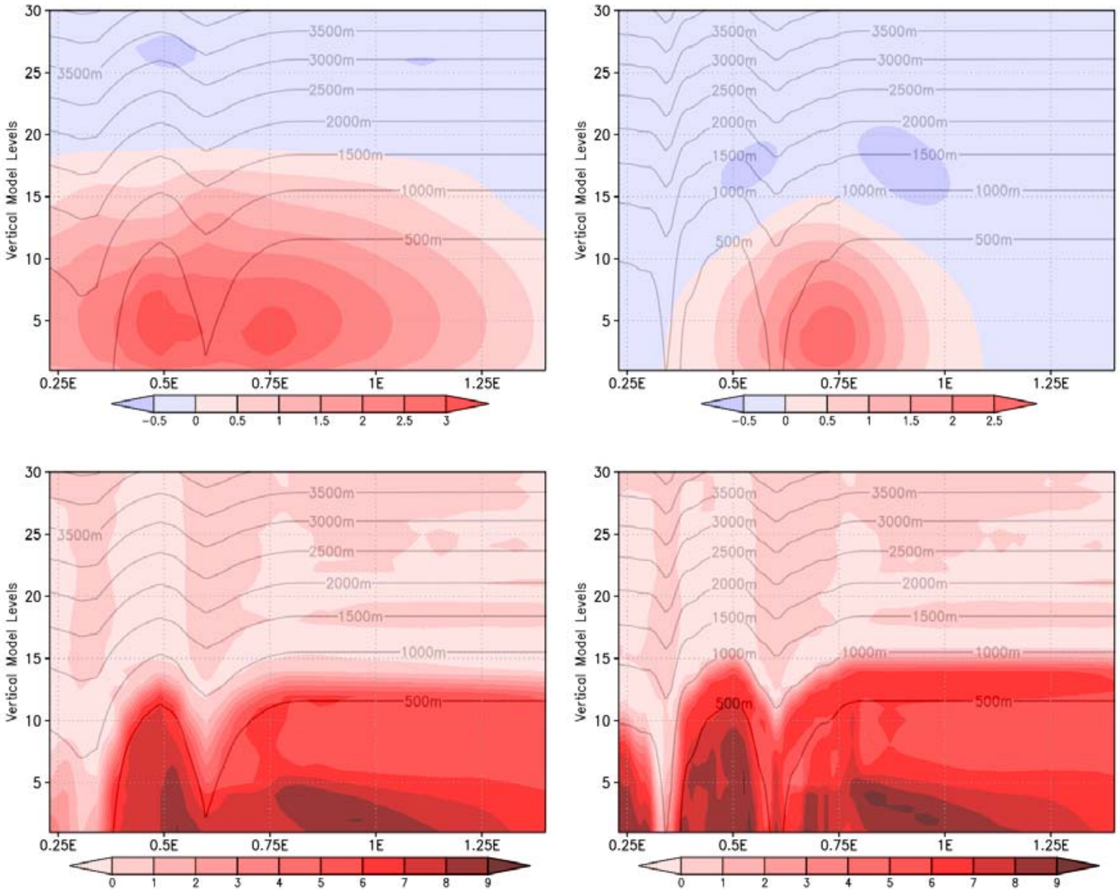

Figure 3.4
Wind module (ms^{-1}) analysis increments along the vertical after assimilation of 1 AWS. Only the first 30 vertical model levels are shown for simplicity. Top: results for WRF-3DVAR at 3GRD (left) and 1GRD (right). Bottom: results for LAPS at 3GRD (left) and 1GRD (right). Black lines denote the geopotential height in meters.

Once both DA systems are contrasted over the area around the station, some significative differences arise. The magnitude of the increments in LAPS analysis are higher than in WRF-3DVar. Also the contours of the analysis increments in LAPS follow the topography profiles giving, in the case of temperature, warmer in the higher and colder in the lower regions. This contrasts with the homogeneity of the approximately circular patterns produced by 3DVar. Even if the background error covariance matrix in 3DVar is tuned reducing the length scale, it always produces these approximately Gaussian shapes. In contrast, LAPS system also allows to adjust the radius of influence but it always modifies the whole domain introducing terrain forcing.

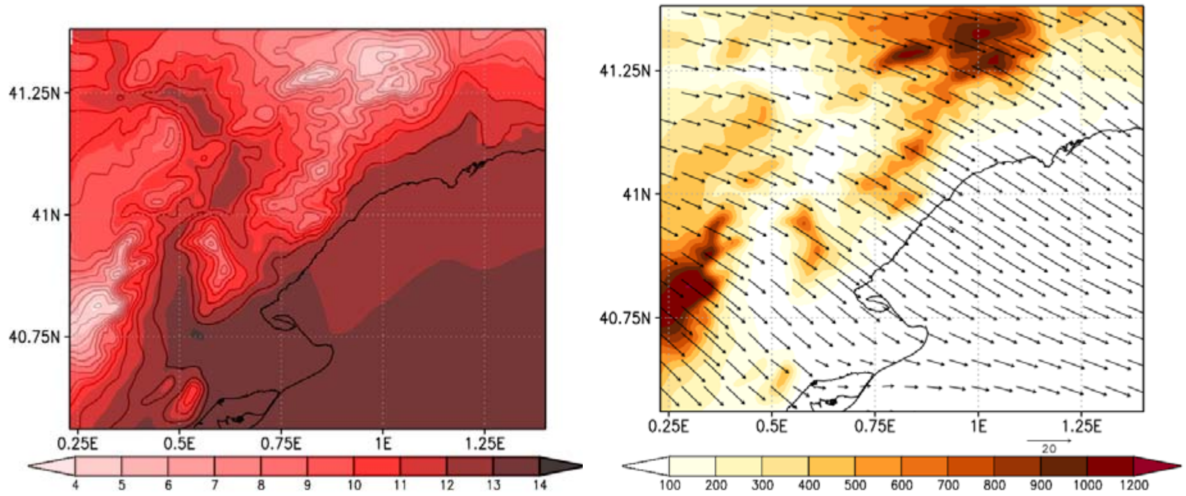

Figure 3.5
ECMWF analysis interpolated to 1GRD (1-km grid resolution) for the CMMC 27 (16th November 2010). Left: first model level contours of temperature (°C). Right: wind vectors at first model level and topography contours (m).

Assimilation of XMET in one meteorological case

Figure 3.5 shows the background temperature and wind field at first model level in 1GRD of the case 27 (Table 3.2). Note how the wind field reflects a north-westerly advection but without small-scale features, only an increase of the wind module uphill and a decrease downhill.

Figure 3.6 and Figure 3.7 show the pattern of increments and the resulting fields for both DA systems after the assimilation of the XMET network for temperature and wind respectively. In the case of temperature, it can be observed how LAPS produces higher variations than WRF-3DVar. As stated in the previous section, LAPS produces an heterogeneous set of increments accounting for the complexity of the terrain, contrasting with the homogeneous 3DVar patterns that apparently neglect local characteristics. Regarding wind field, WRF-3DVar presents two marked increment minima (Fig. 3.7) surrounded by homogeneous "circular" contours, whereas LAPS gives much complex patterns related to the terrain. Notably, both systems spread their increments over the sea in a different way: LAPS decreases the wind module significantly over the eastern side of the domain whereas 3DVar slightly reinforces it.

As seen in Figure 3.7, LAPS analysis is in better agreement with station magnitudes (blue vectors) than 3DVar. An example is found in the north-east and south-west extremes of the domain, where 3DVar shows a wind analysis away from the observations. This is probably because the prescribed correlation function gives a wind field omitting the small-scale features.

Finally, taking advantage of the proximity between the first model level (at a mean elevation of 8 m above the terrain) and the 10 m height wind measurements, the RMSE has been calculated using all stations of the network and the analysed wind at the grid points closest to the stations,

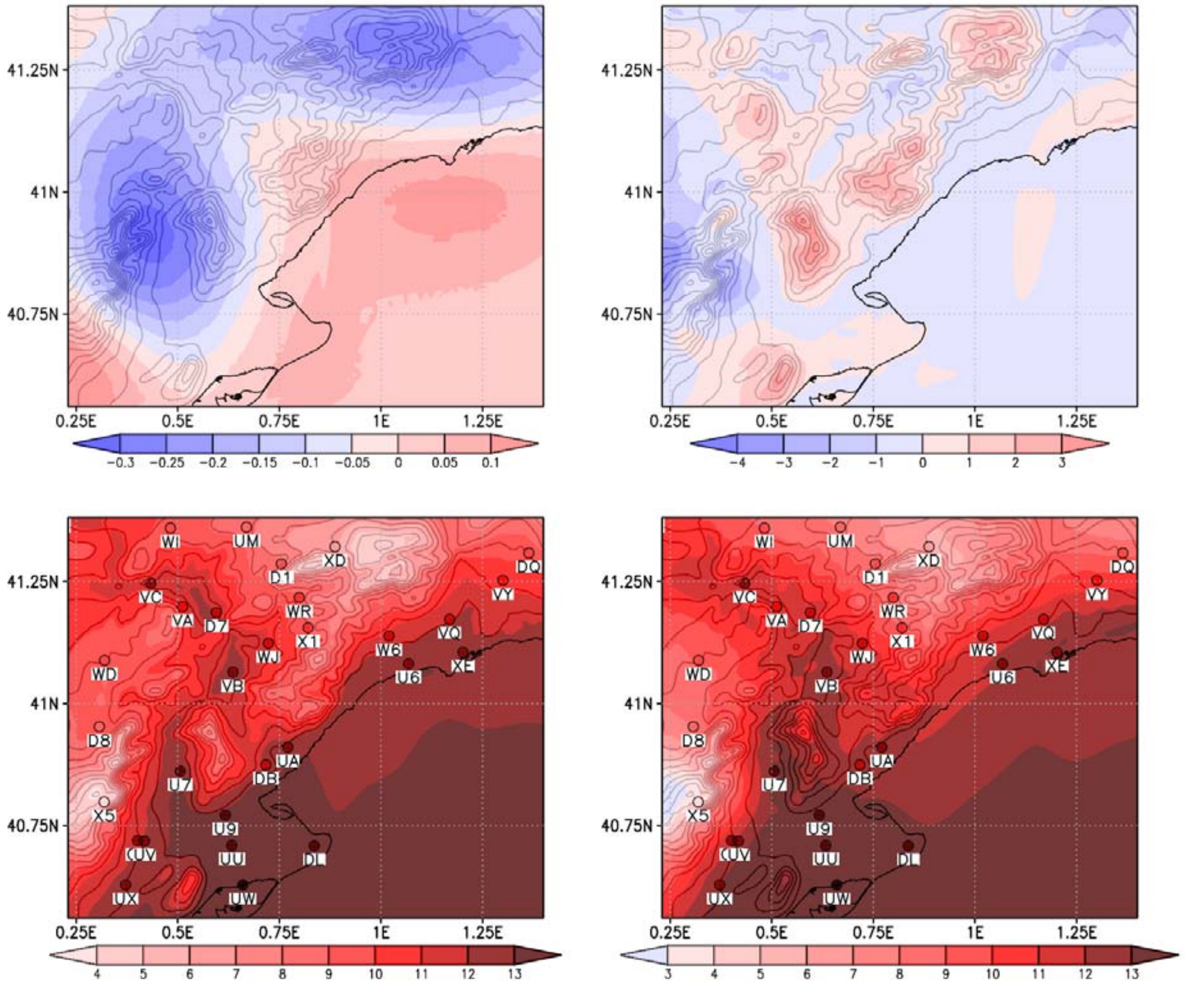

Figure 3.6
Top: analysis temperature increments (°C) at the first model level after assimilating the whole XMET network of AWS for CMMC 27. Results for WRF-3DVAR (left) and LAPS (right) on 1GRD. Note the different colour scales for 3DVAR and LAPS increments. Bottom: resulting temperature (°C) analysis (background plus increment) for WRF-3DVAR (left) and LAPS (right). White labels are the id. of the stations. The small filled circles denote the station locations and the temperature observed.

resulting in 5.27 ms^{-1} for the background, 3.87 ms^{-1} for 3DVar and 1.47 ms^{-1} for LAPS analysis. Additionally, the absolute error at the independent station are of 1.38 ms^{-1} for the background, 1.6 ms^{-1} for 3DVar and 0.97 ms^{-1} for LAPS analysis.

3.4 Validation of short-range forecasts

To validate the short-range forecast, the 29 CMMC (Table 3.2) during 2010 are used. First of all, Figure 3.8 shows the 1GRD wind analysis RMSEs for each case. As in the previous section, it takes advantage of the proximity between the first model level (at a mean elevation of 8 m above the terrain) and the 10 m height wind measurements. LAPS analyses show a better improvement than 3DVar in a vast majority of cases. Even that, both DA systems offer a better initial condition for

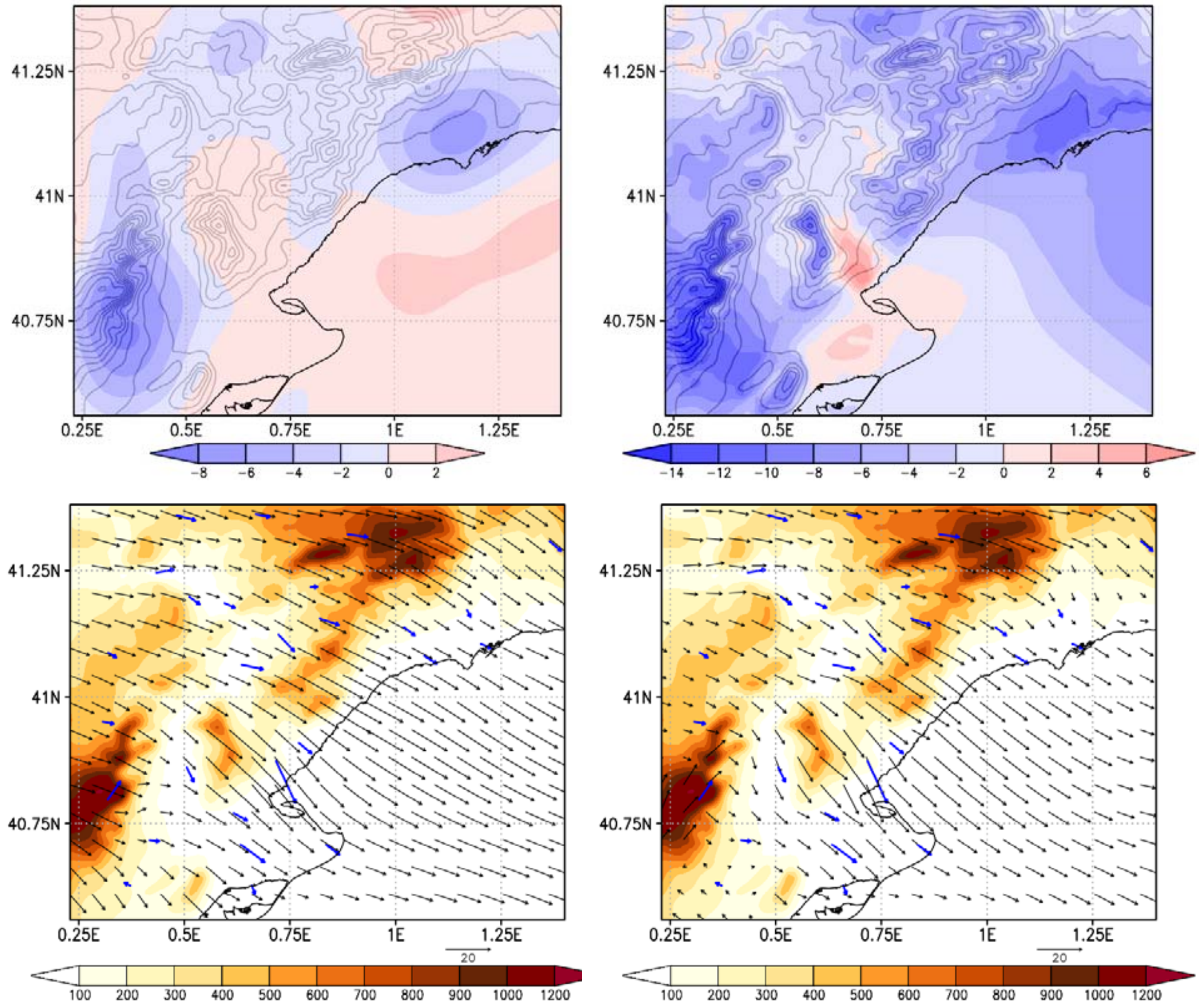

Figure 3.7
Top: analysis wind module increments (ms^{-1}) *at the first model level after assimilating the whole XMET network of AWS for CMMC 27. Results for WRF-3DVAR (left) and LAPS (right) on 1GRD. Bottom: resulting wind vector analysis (background plus increment) for WRF-3DVAR (left) and LAPS (right). Blue vectors show surface observations.*

the model at the AWS locations.

Figure 3.9 shows the 1GRD RMSEs for each case after 1, 6 and 12 h forecasts. After 1 h of model integration (Figs. 3.9a-c), CNTRL-runs and 3DVar-runs are quite similar, particularly for temperature and wind module. In contrast, LAPS-runs show a substantially better model performance in a vast majority of cases (22 out of 29) for WV10m. Typically, the averaged wind module improvement in the LAPS-runs is of about 1 ms^{-1} in terms of RMSE. For the 6 and 12 h forecasts, results for T2m are almost identical in the three sets of runs. However, the wind module forecasts show slightly better skills for LAPS-runs, especially in those cases where the CNTRL-runs and the 3DVar-runs present larger errors.

Figure 3.10 contains the temporal evolution of the RMSE for the three sets of simulations.

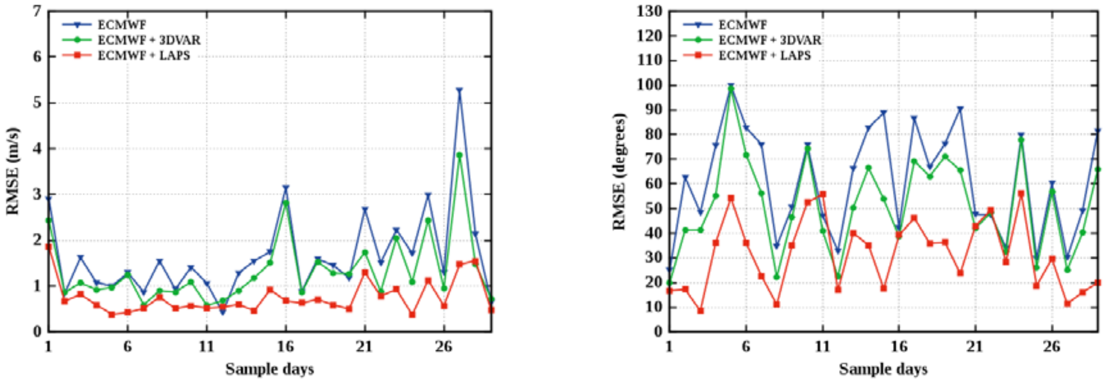

Figure 3.8
RMSEs for each of the 29 CMMC analysis. Cases are ordered chronologically. RMSEs are calculated for two variables: WV10m (ms^{-1}) *and WD10m (degrees) from left to right respectively. The lines show RMSE for the CNTRL-runs (blue), 3DVAR-runs (green) and LAPS-runs (red) runs. See Table 3.2 for a description of each CMMC case.*

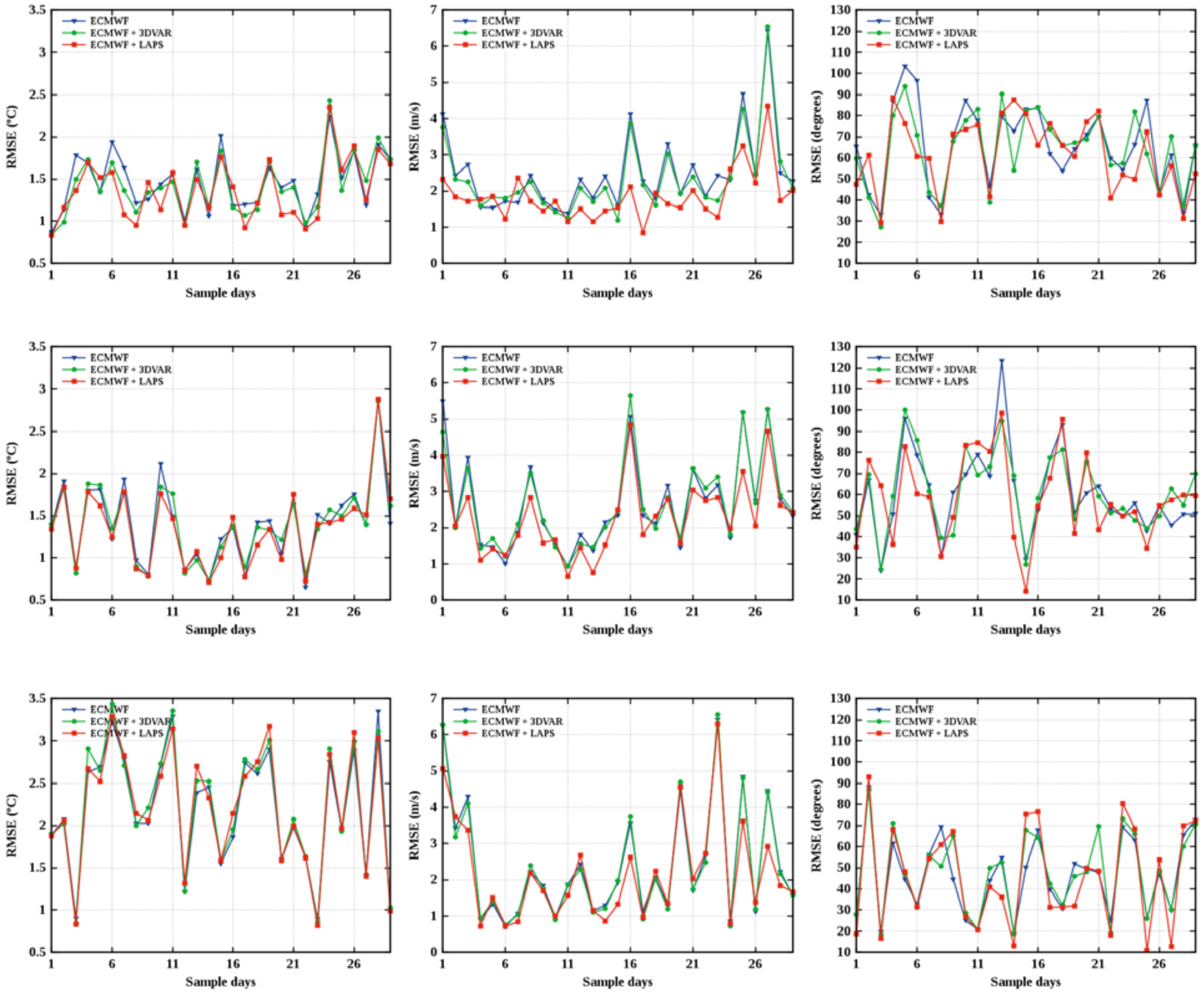

Figure 3.9
RMSEs for each of the 29 CMMC after 1 (top), 6 (middle) and 12 hours (bottom) forecasts for 1GRD. Cases are ordered chronologically. RMSEs are calculated for three variables: T2m (°C)*, WV10m* (ms^{-1}) *and WD10m (degrees) from left to right respectively. The lines show RMSE for the CNTRL-runs (blue), 3DVAR-runs (green) and LAPS-runs (red) runs. See Table 3.2 for a description of each CMMC case.*

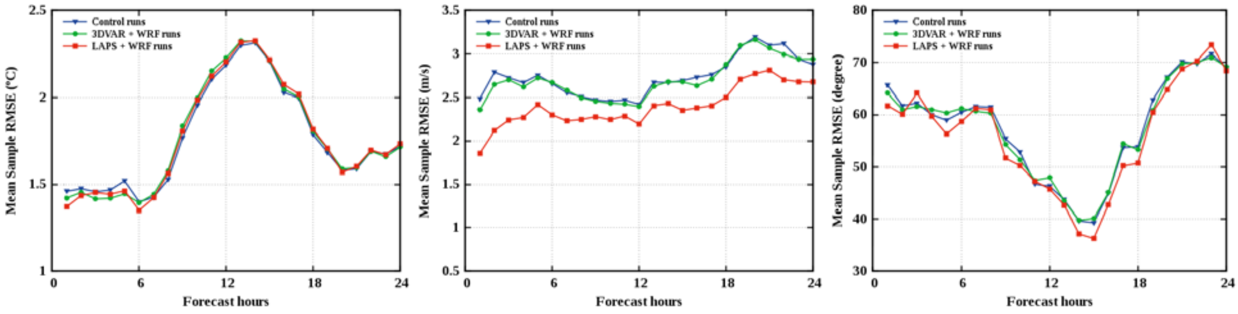

Figure 3.10
Evolution with forecast time of the 1GRD RMSE for the whole CMMC. Results for T2m (°C), WV10m (ms^{-1}) and WD10m (deg) from left to right respectively. The lines show RMSE for the CNTRL-runs (blue), 3DVAR-runs (green) and LAPS-runs (red) runs. Each point of the graphic results from computing the RMSE using all the stations and CMMCs.

RMSE is computed for T2m, WV10m and WD10m for all 29 cases of the CMMC at each forecast hour. On average, T2m forecasts for 3DVar-runs and LAPS-runs present no improvement with respect to the CNTRL-runs, except for the first 6 h. This is also true for WV10m forecasts in the 3DVar-runs. However, in contrast, the WV10m forecasts improve substantially through time in the LAPS-runs because the LAPS analyses cause an important reduction on the RMSE that persists up to 24 h later. The LAPS-runs offer also slightly better skills for WD10m.

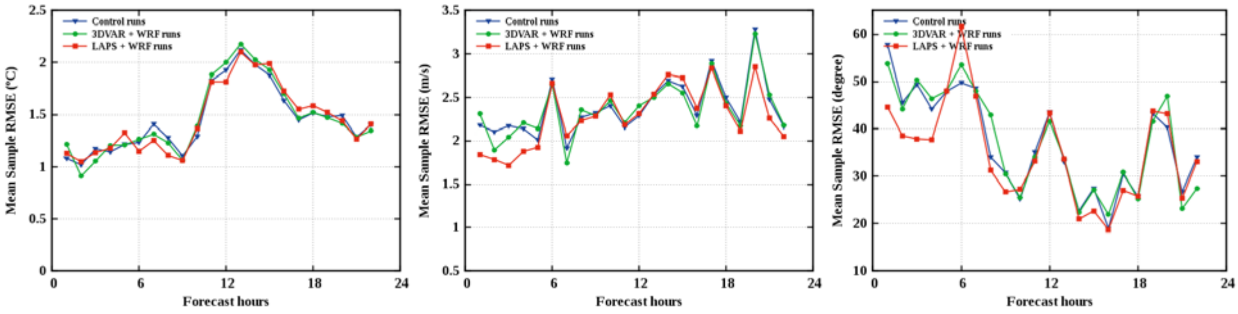

Figure 3.11
Evolution with forecast time of the 1GRD RMSE computed with the independent station (Section 3.3.1) for the whole CMMC. Results for T2m (°C), WV10m (ms^{-1}) and WD10m (deg) from left to right respectively. The lines show RMSE for the CNTRL-runs (blue), 3DVAR-runs (green) and LAPS-runs (red) runs.

Finally, Figure 3.11 provides the validation using an independent AWS not assimilated at the initial time. As seen in Figure 3.1, the AWS is at a complex terrain location and near a wind channelling zone. One remarkable difference compared to the previous results shown in Figure 3.10 is, the improvement produced by LAPS analysis for WV10m is noticeable only within the initial 5 forecast hours. For WD10m it is also possible to observe an improvement in the early forecast hours of LAPS-runs. In the case of 3DVar-runs, WV10m and T2m offer a minor RMSE at 2 h and 3 h forecast times, but generally no substantial improvement is provided.

3.5 Summary and conclusions

The capacity of 3DVar and LAPS systems to assimilate data from surface AWS in high-resolution (complex terrain) operational forecasts has been studied. A preliminary analysis consisting on the assimilation of a single AWS has revealed significant differences between both DA systems. The 3DVar analysis presents a strong dependence on the prescribed correlation function in the background error covariance term. The spread of the analysis increments in 3DVar is very homogeneous, reminding large-scale features that are unrealistic given the inhomogeneous nature of the near-surface fields and the data assimilated. In contrast, LAPS takes into account small-scale features and provides an analysis much consistent with observations. **These characteristics make LAPS more suitable to assimilate a high-density AWS network into a high-resolution model domain.**

The XMET AWS network has been assimilated in 29 meteorological cases and used to compare the WRF-ARW model skills for three sets of runs: CNTRL-runs (initial condition without DA), 3DVar-runs, and LAPS-runs. The conclusion is that **high-resolution WRF-ARW forecasts initialized with LAPS analyses improve substantially the wind fields.** These improvements are sustained during a period of 24 h when validating with the AWS assimilated. Although not statistically relevant, when validating with an independent AWS the improvement is observed only during 5 h. The temperature field shows no worsening and a small improvement is observed for the first 6 h. On the other hand, 3DVar-runs do not lead to significant variations and after few hours of simulation converge rapidly to background.

The results are in agreement with other studies that assimilate AWS only (e.g.Deng, Stull [2007]) except for the wind field (Fig. 3.10). The improvements gradually decrease after the assimilation period of the forecast (5-6 h). This decrease could be attributed to the effects of the lateral boundary conditions advecting into the domain. The adjustments made by the model to balance the mass and wind fields could also contribute to decrease the quality of the forecasts. On the other hand, the 24 h wind field improvement produced by LAPS at the AWS locations suggest that significant changes (Fig. 3.8) in the fields could lead to more enduring improvements.

Future work at SMC will try to assimilate the XMET network operationally, as currently done with data from satellites, radars, soundings and metars. This is a desirable step before running forecasts at 1 km grid resolution in a near future.

CHAPTER 4

RANS Diurnal cycle simulation and applications

This chapter is an elaboration of the material in

Barcons, J., Avila, M., Folch, A., **submitted**. Diurnal cycle RANS simulations applied to wind resource assessment. Wind Energy

4.1 Introduction

Over land, the ABL undergoes strong diurnal variations in response to surface forcings, *e.g.* frictional drag, terrain orography, and solar heating among others. The diurnal cycle of insolation is intrinsically dynamic and entails large variations in wind intensity, wind direction and turbulence. In order to account for these dynamical and thermal effects, microscale RANS models have been coupled with the energy conservation equation. The thermally coupled models are intrinsically transient and, as a consequence, the computational cost increases significantly with respect to the neutral case. Furthermore, the simulation of diurnal cycles needs time-dependent boundary conditions, commonly imposed by dynamical downscaling methodologies or imposing idealised profiles (*e.g.* Pieterse, Harms [2013]; Castro et al. [2014]; Koblitz et al. [2015]; Veiga Rodrigues et al. [2016]).

In the context of Wind Resource Assessment (WRA), the neutral atmosphere assumption is justified as long as the neutral condition is statistically representative of the average flow on a given site. However, situations exist in which the neutral assumption fails in reproducing near-surface yearly mean wind observations in regions with strong stratification. Typically, neutral RANS models together with wind observations from masts are used during WRA to characterise wind distributions over an area of interest. To this purpose, wind speedups (relative to mast) for different wind direction sectors simulations are frequency-weighed to obtain annual averaged values. However, in the case of non-neutral models, the question of how to extract meaningful results from a transient simulation is challenging and remains open yet.

Section 4.2 presents the equations implemented in the Alya-CFDWind microscale wind model to simulate a thermally stratified ABL. Section 4.3 presents the methodology used to run diurnal cycles, and a methodology to extract worth information. Section 4.4 proposes a novel methodology for WRA that builds on diurnal cycle RANS simulations and introduces thermal stability as an additional parameter in the process. Finally, Section 4.5 presents an initial study to test the 1D precursor model using time-dependent mesoscale tendencies to drive the diurnal cycle simulation.

4.2 Thermal coupling

The thermal model of Sogachev et al. [2012] has been implemented in Alya-CFDWind in order to solve atmospheric flows in complex terrains considering atmospheric stability in addition to the Coriolis force. The resulting governing equations are those introduced in Chapter 2 (Section 2.2) with some additional terms (in red) accounting for the thermal coupling plus the energy conservation equation (4.5). The model uses the Boussinesq approximation in the momentum equation for the thermal coupling. The resulting system of equations is:

$$\begin{aligned}
\nabla\cdot\boldsymbol{u} &= 0 && (4.1)\\
\frac{\partial \boldsymbol{u}}{\partial t}+\boldsymbol{u}\cdot\nabla\boldsymbol{u}-\nabla\cdot(\nu_t\nabla^s\boldsymbol{u}) &= -\boldsymbol{\nabla}p-2\boldsymbol{\omega}\times\boldsymbol{u}-\boldsymbol{g}\frac{\theta}{\theta_0} && (4.2)\\
\frac{\partial k}{\partial t}+\boldsymbol{u}\cdot\nabla k-\nabla\cdot\left(\frac{\nu_t}{\sigma_k}\cdot\nabla k\right) &= P_k-\varepsilon+G_k && (4.3)\\
\frac{\partial \varepsilon}{\partial t}+\boldsymbol{u}\cdot\nabla \varepsilon-\nabla\cdot\left(\frac{\nu_t}{\sigma_\varepsilon}\cdot\nabla \varepsilon\right) &= \frac{\varepsilon}{k}\left[\left(C_1+(C_2-C_1)\frac{l_m}{l_{\max}}\right)P_k-C_2\varepsilon+C_3G_k\right] && (4.4)\\
\frac{\partial \theta}{\partial t}+\boldsymbol{u}\cdot\nabla \theta-\nabla\cdot\left(\frac{\nu_t}{\sigma_\theta}\cdot\nabla \theta\right) &= 0 && (4.5)
\end{aligned}$$

where the potential temperature θ is an additional unknown field. The mixing length l_m (same as eq. 2.23 for the neutral case) and the maximum mixing length $l_{\max}$ are computed as:

$$\begin{aligned}
l_m &= C_\mu^{3/4}\frac{k^{3/2}}{\varepsilon}\\
l_{\max} &= \beta\frac{\int_0^\infty z\sqrt{k}dz}{\int_0^\infty \sqrt{k}dz}
\end{aligned}$$

where β is a coefficient chosen such in a neutrally stratified atmosphere $l_{max}=l_0$ (here, l_0 is the l_{max} eq. 2.24 for the neutral case). The turbulent kinetic energy production rate by buoyant forces (G_k) is:

$$G_k = -\alpha|\boldsymbol{g}|\frac{\nu_t}{\sigma_\theta}\frac{\partial\theta}{\partial z} \qquad (4.6)$$

where α is the thermal expansion coefficient (α=$1/\theta_0$ for ideal gases, being θ_0 a reference potential temperature) and σ_θ is the turbulent Prandtl number. Table 4.1 lists the model coefficients including the expression for C_3 depending on the stability-related coefficient α_G [Sogachev et al., 2012].

Table 4.1
Alya-CFDWind thermal model constants

κ	C_μ	C_1	C_2	C_3	σ_k	σ_ε	σ_θ
0.4	0.033	1.176	1.92	$1+(C_1-C_2)\alpha_G$	1.0	1.238	0.9

Boundary conditions

The thermally coupled problem also adds some additional terms into the specification of the boundary conditions. Changes with respect to what was exposed in Chapter 2 (Section 2.2) for the neutral formulation are:

- **On the bottom boundary**, wall law functions impose the Monin-Obukhov similarity theory

[Monin, Obukhov, 1954] with an additional term in the $|\boldsymbol{u}|$ equation plus the θ equation. Thus, $|\boldsymbol{u}|$ and θ at a distance δ_w from the ground are:

$$|\boldsymbol{u}(\delta_w)| = \frac{u_*}{\kappa}\left[\ln\left(1+\frac{\delta_w}{z_0}\right) - \Psi_m\left(\frac{\delta_w}{L}\right)\right] \tag{4.7}$$

$$\theta(\delta_w) = \theta_{wall} + \frac{\sigma_t\theta_*}{\kappa}\left[\ln\left(1+\frac{\delta_w}{z_0}\right) - \Psi_h\left(\frac{\delta_w}{L}\right)\right] \tag{4.8}$$

where θ_* is the friction potential temperature ($\theta_*{=}q_{wall}/\rho c_p u_*$, with q_{wall} being the downward surface heat flux, c_p is the heat capacity and ρ is the air density), and θ_{wall} is the potential temperature at the wall. The correction terms $\Psi_m(\delta_w/L)$ and $\Psi_h(\delta_w/L)$ account for thermal stability and are functions of the ratio δ_w/L, where Obukhov length L reads as

$$L = u_*^2/\kappa\alpha|\boldsymbol{g}|\theta_* \tag{4.9}$$

- **On the top boundary**, symmetry boundary condition (zero normal gradient) is imposed for θ.
- **On the inflow boundary**, θ vertical profile is imposed from a 1D precursor simulation assuming uniform roughness and flat terrain.
- **On the outflow boundary**, symmetry boundary condition is imposed for θ.

4.3 Methodology for diurnal cycle simulation

The simulation of a diurnal cycle on complex terrain comprehends the same general steps than in the thermally neutral flow simulation; the pre-process, the AlyaCFD-Wind simulation and the post-process. As in the previous Section, only the additional aspects of the thermally coupled problem are introduced here:

4.3.1 1D precursor simulation

The 1D precursor is a single-column model that furnishes vertical profiles used as initial and boundary conditions to Alya-CFDWind. To run a 1D diurnal cycle (transient integration), the precursor model needs a time-varying surface temperature (or surface heat flux) and a geostrophic wind intensity.

The precursor model has been implemented and verified (code-to-code) with the GABLS2 benchmark [Svensson et al., 2011], a challenging case of strong diurnal cycle over dry land. Moreover, a modified version of GABLS2 is considered, consisting on a periodic repetition of the boundary conditions of the GABLS2 experiment during the first day, henceforth called CYCLE. This is done to guarantee that, after a sufficient time, the results of the 1D precursor model are cyclic and independent on the initial condition. Figure 4.1 shows the time-varying surface temperatures for both diurnal cycles (GABLS2 and CYCLE), used as the bottom condition for the 1D Alya-CFDWind precursor model. In order to facilitate the model inter-comparison [Svensson et al., 2011], the forcing conditions (driving the diurnal cycle) were simplified giving rise to an "idealised" case that considers a constant geostrophic wind of $|\boldsymbol{u}_g| = 9.5$ ms^{-1}. Using these surface temperatures and geostrophic wind, the 1D precursor model was run in a grid of 4 km height using 450 vertical elements growing geometrically in size from 0.5 to 10 m and using an integration time step of δt=10 s. Compared with the neutrally stratified simulation, the element size at the ABL height needs to be around one order of magnitude smaller when running thermally stratified cases. This is necessary in order to capture the very steep gradients of wind velocity, turbulent kinetic energy and potential temperature around the ABL height.

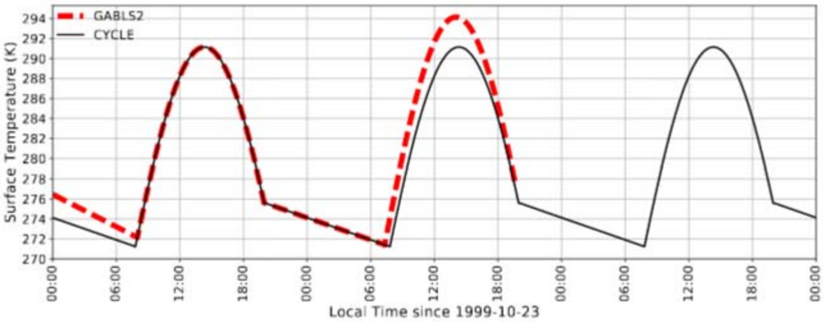

Figure 4.1
Time series of surface temperature for GABLS2 and CYCLE 1D diurnal cycles. The GABLS2 benchmark actually starts on 22 October 1999 at 16 h LT allowing 8 h of spin-up. The 23 October 1999 is selected as the evaluation period and is the segment that is repeated in the periodic CYCLE.

Figure 4.2 shows the resulting 1D model vertical profiles at noon (thermally unstable) and midnight (thermally stable). Note that the CYCLE periodic run needed 5 cycles to achieve periodicity so, Cycle5 vertical profiles (Fig. 4.2) were obtained in the following cycles. As expected, the unstable and stable regimes show large differences. For example, the nocturnal boundary layer (NBL) height is slightly above 100 m contrasting with the 1 km ABL height at noon. Furthermore, there is a well defined nocturnal low-level jet of about $\boldsymbol{u}$=12 ms^{-1} at the top of the NBL that contrasts with $\boldsymbol{u}$=6.5 ms^{-1} at the same height during the unstable regime. Turbulent kinetic energy also shows large differences, specially over 100 m height.

Figure 4.3 compares 1D precursor model near-surface results (GABLS2 and CYCLE) with those from the Large Eddy Simulation (LES) in Kumar et al. [2010] and the RANS single-column models (SCM) spread from Svensson et al. [2011]. It is observed that GABLS and CYCLE runs obtain similar results, differing more during the day time. The most remarkable differences between the

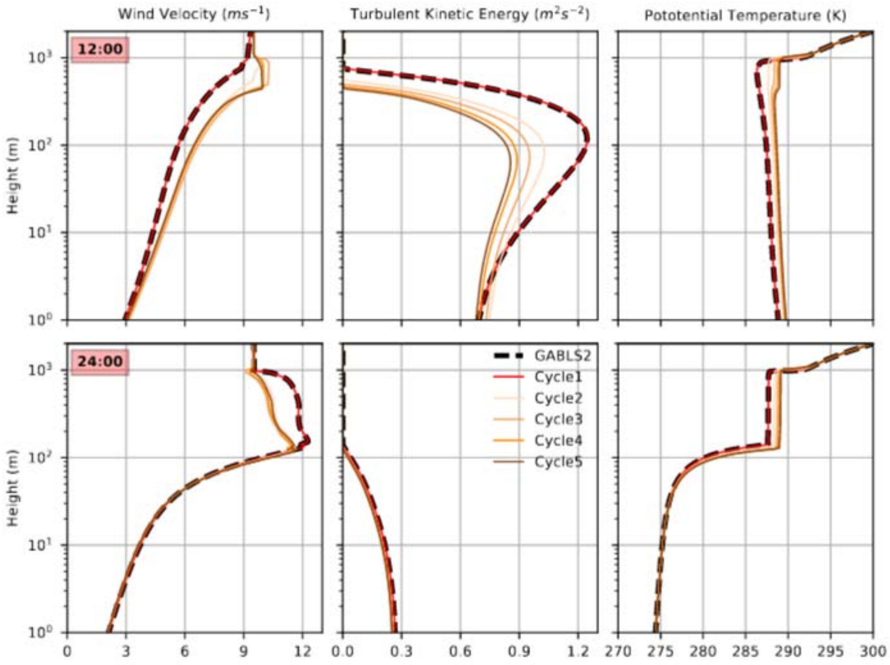

Figure 4.2
Vertical profiles of wind velocity, turbulent kinetic energy and potential temperature at 12:00 (top) and at 24:00 LT (bottom) for GABLS2 and CYCLE (5 consecutive periodic cycles Cycle1 to Cycle5 are shown).

precursor and the LES model appear in the 10 m wind velocity. Despite this, the precursor results lay within the spread of the SCMs.

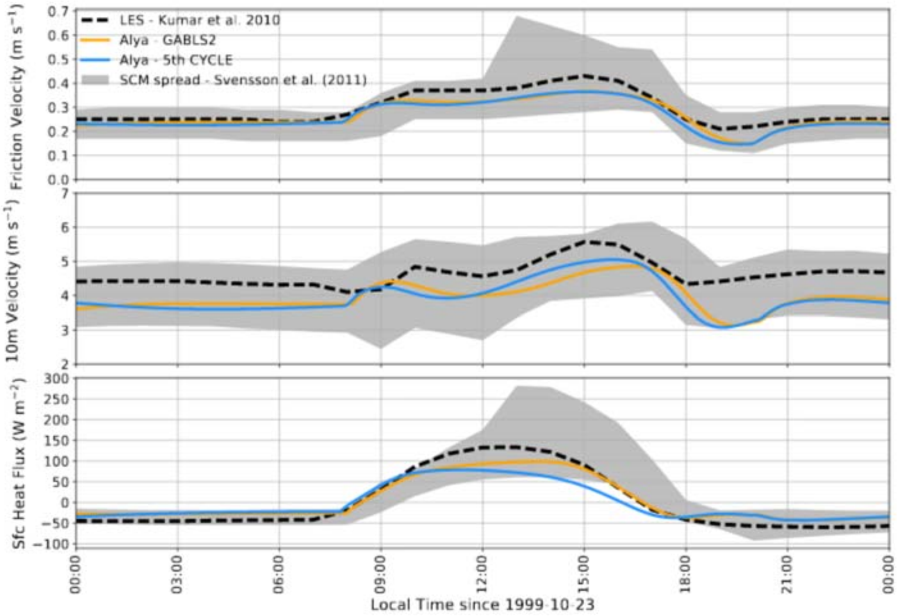

Figure 4.3
GABLS2 23 October 1999 time series of friction velocity (top), 10 m wind velocity (middle) and surface heat flux (bottom). Comparison between LES simulation from Kumar et al. [2010], our precursor model (GABLS2 and Cycle5 results) and the SCM spread reported in Svensson et al. [2011].

4.3.2 3D diurnal cycle simulation

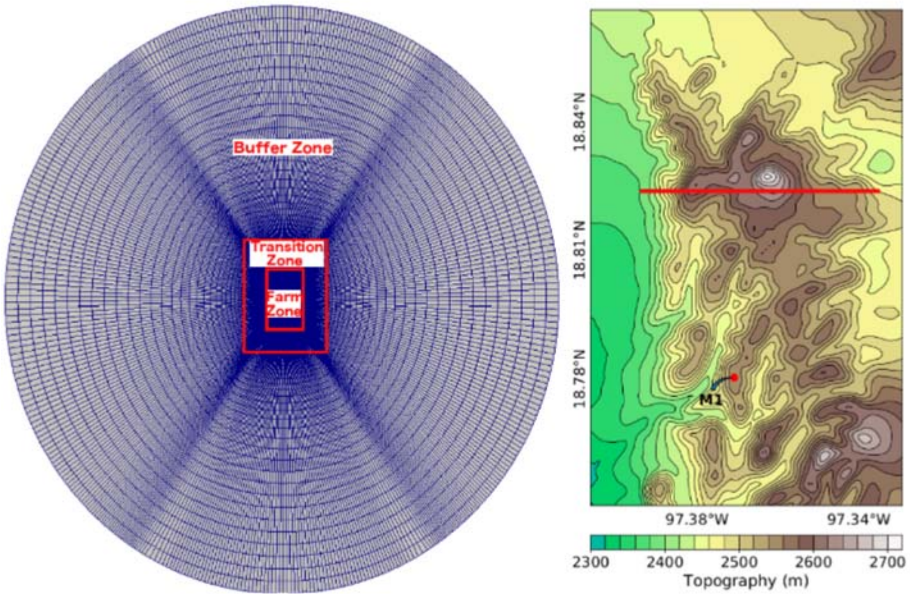

Figure 4.4
Puebla test case. Horizontal mesh at surface with the inner part coloured (left) and a zoom of the inner region of interest at 100 m resolution (right) showing contours of topography. The computational mesh has 1.6 million nodes. The horizontal red line marks the longitudinal cut used in further plots and M1 is the reference mast used for WRA.

A site located in the Mexican state of Puebla has been used to test the implementation of the thermal model in Alya-CFDWind and the diurnal cycle methodology. This site was selected because, in addition to its very complex orography, we had access to a long-period dataset acquired by a private company during a wind resource measurement campaign. The dataset used here consists on 80 m height wind measurements from 7 met masts instrumented with sonic anemometers for a total period of acquisition of 3 years (not synchronous in all masts). These data are used in the following sections to validate the diurnal cycle simulations and the related applications.

For the 3D diurnal cycle simulations, a domain with an inner region of interest of 6.4×13 km^2 is considered (Farm Zone in Figure 4.4). In this inner part, the horizontal grid resolution is δx=δy=100 m and grows gradually lengthwise across the transition and buffer zones. Along the vertical direction, the grid has 60 vertical layers growing geometrically in size inside the ABL (up to $\sim$ 1000 m height) from 1 to 170 m. The top of the mesh is at 2.4 km above the highest terrain elevation. The geostrophic wind velocity is set to $|\boldsymbol{u}_g|$=17.5 ms^{-1}. The 1D precursor simulation generates the time dependent inflow and ground boundary conditions for the 3D simulation. The precursor simulation imposes the time varying surface temperature $\theta_{wall}(t)$ of the CYCLE case (Section 4.3.1), which is prescribed on the bottom boundary of the entire domain through the boundary condition (eq. 4.8). The resulting wind velocity, turbulence and potential temperature profiles of the fifth periodic cycle are used to run 16 diurnal cycles, each characterised by a geostrophic wind direction.

As an example, Figure 4.5 shows contour plots of u_x, k and θ for the 270° geostrophic wind direction simulation at two different time instants. This Figure shows also vertical profiles at four marked points to highlight differences between both time instants. Note that, under stable conditions, the flow is not allowed to go uphill and recirculates (v_x shows negative values near the surface) due to the strong stable thermal stratification. Looking at 2 h LT v_x and k plots, it can be observed how the nocturnal jet above the top of the hills causes a strong wind shear near the surface that originates a high turbulent kinetic energy region. These effects contrast with the profiles under unstable conditions. The 14 h LT plots clearly show how the atmospheric instability develops a well-mixed ABL with smoother vertical profiles, v_x gradually grows with heigh and k has its maximum near the surface and decreases gently with heigh.

The simulation of a 3D diurnal cycle over complex terrain introduces new simulation challenges with respect to the neutral stability case. On the one hand, in the neutral stability case symmetry BC are prescribed at the outflow for k and ε and the geostrophic pressure is prescribed (Section 2.2.2). This later condition is not straightforward in the non-neutral transitory case due to the differences between the pressure at the outflow and the prescribed pressure. In order to avoid imposing BCs for pressure at the outflow, we impose the vertical profiles of $\boldsymbol{u}$ (Dirichlet outflow condition). This kind of boundary condition produces numerical oscillations near the outflow wall, but these are small and constrained to the buffer region. On the other hand, the dynamics of diurnal cycle simulations needs to be captured using an appropriate time step. These transient simulations are therefore computationally more expensive than neutral simulations which reach steady state. At the beginning, we use a very small time integration step (δt <1 s) to assimilate the IC, which comes from a flat terrain precursor (*i.e.* no terrain effects, no recirculation). So, we use a variable integration time step starting from δt= 0.15 s during 200 time steps and then increasing δt progressively until a value of δt= 6 s is reached. The computation of each diurnal cycle for the Puebla case (1.6 M nodes) took around 15 h CPU time using 256 cores for 28 h of real time simulation (18,000 time integration steps) using the MN-III supercomputer.

4.3.3 Diurnal cycle discretisation using ABL stability classes

The proposed methodology entails two major aspects; the simulation of diurnal cycles and the selection of one time instant representative of each stability class (process applied to each wind direction diurnal cycle simulation). Thus, four thermal stability regimes have been defined: stable, stable-to-unstable transition, unstable and unstable-to-stable transition. The selection criteria analyses the θ and $|\boldsymbol{u}|$ vertical profiles from the 1D precursor simulation. For convenience, the analysis is

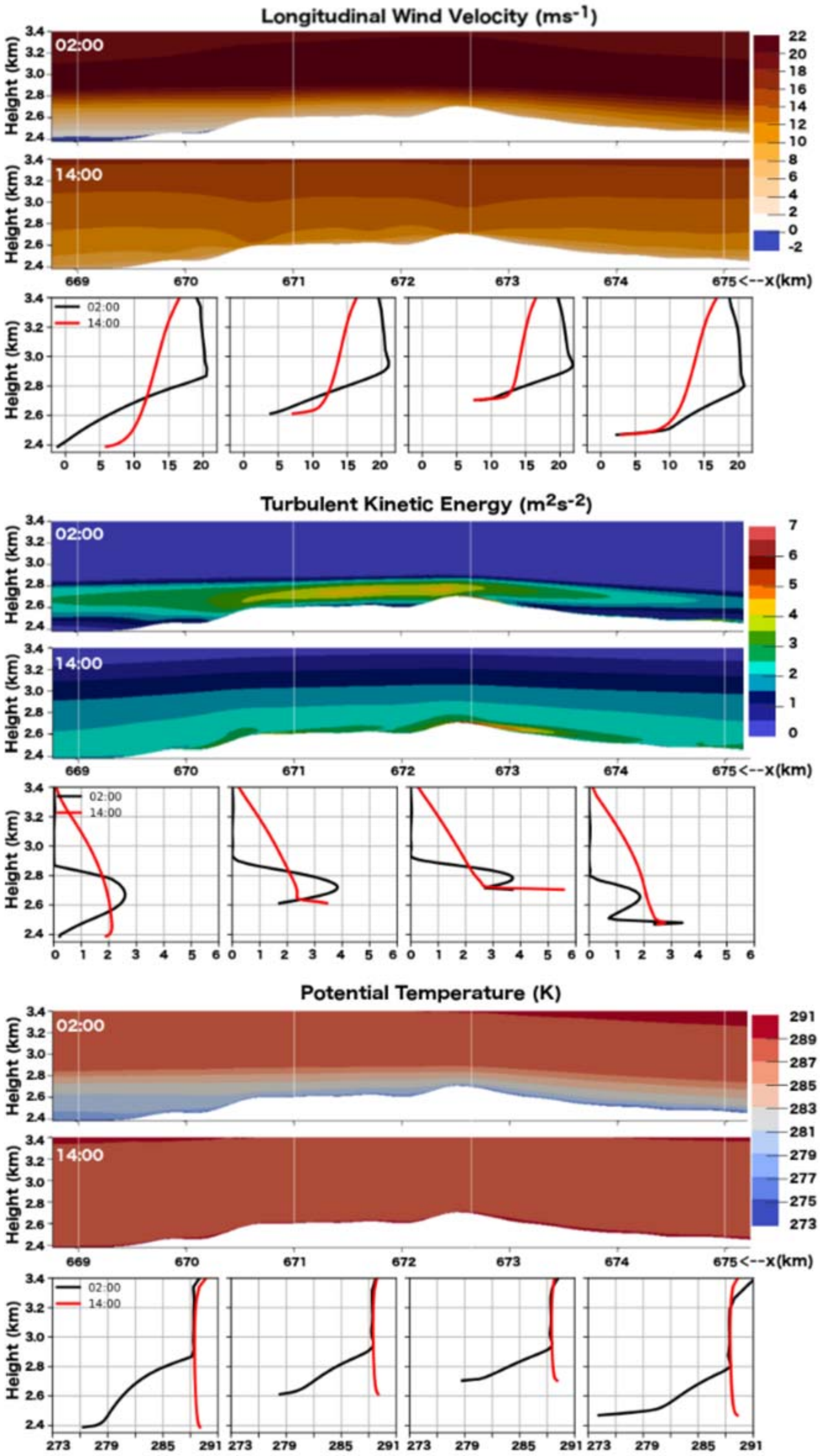

Figure 4.5
Contour plots and vertical profiles at 4 sites (marked with thin vertical white lines) at 2 h (thermally stable) and 14 h (thermally unstable) LT for longitudinal velocity u_x *(top), turbulent kinetic energy* k *(middle) and potential temperature* θ *(bottom) along the 6 km lenght cross section shown in Figure 4.4. Results for the diurnal cycle simulation with a geostrophic wind direction of 270°, i.e. aligned with the x axis.*

made using the first 100 m above terrain because observed wind time series are at 80 m height above terrain. The stable and unstable cases are easily identified because the $|\boldsymbol{u}|$ profiles remain almost stationary for certain hours (2-3 h). In contrast, the transition cases are identified using the extremes of the Obukhov length ($|L| \rightarrow \infty$) where L changes its sign; from positive-to-negative represents stable-to-unstable, from negative-to-positive represents unstable-to-stable. Left plot in Figure 4.6 shows the time evolution of L with vertical lines denoting the time instants assumed representative of each thermal stability class.

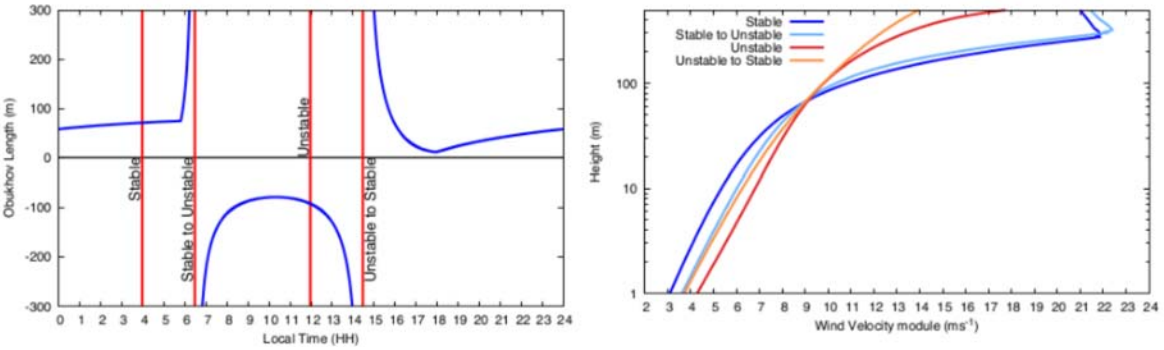

Figure 4.6
Left: Obukhov length time evolution of Cycle5 diurnal cycle using ALYA-CFDWind1D model. The red vertical lines indicate the time instants that are considered representative of each thermal stability class. Right: wind velocity vertical profiles for each stability class (logarithmic scale).

Figure 4.7 compares the Alya-CFDWind results for the 90° geostrophic wind direction simulations. This figure compares the wind speed-ups at 80 m height from a neutral stratified steady state simulation with the representatives of each stability class from the diurnal cycle simulation. The stable stratified case presents two main differences respect to the neutral case; on the one side, a strong speed-down in the eastern part of the domain; on the other side, an important down-slope speed-up in the western part favoured by the strong nocturnal boundary layer stratification. Unstable and unstable-to-stable cases differ from the neutral case but to a lesser extent.

4.4 Application 1: Wind resource assessment

Microscale Computational Fluid Dynamics (CFD) models are routinely used for wind resource assessment. These models generally assume neutral atmospheric stratification, an assumption that can lead to inaccurate modelling results and to larger uncertainties at certain sites. A new methodology for wind resource evaluation is proposed based on RANS simulations of diurnal cycles including the effect of thermal stratification. Time-dependent boundary conditions generated by a 1D precursor simulation drive the 3D diurnal cycle simulations. As explained in Section 4.3.3, the simulations results for each geostrophic wind direction are discretised by selecting time instants that are representative of different thermal stability regimes. Finally, these representative results are combined

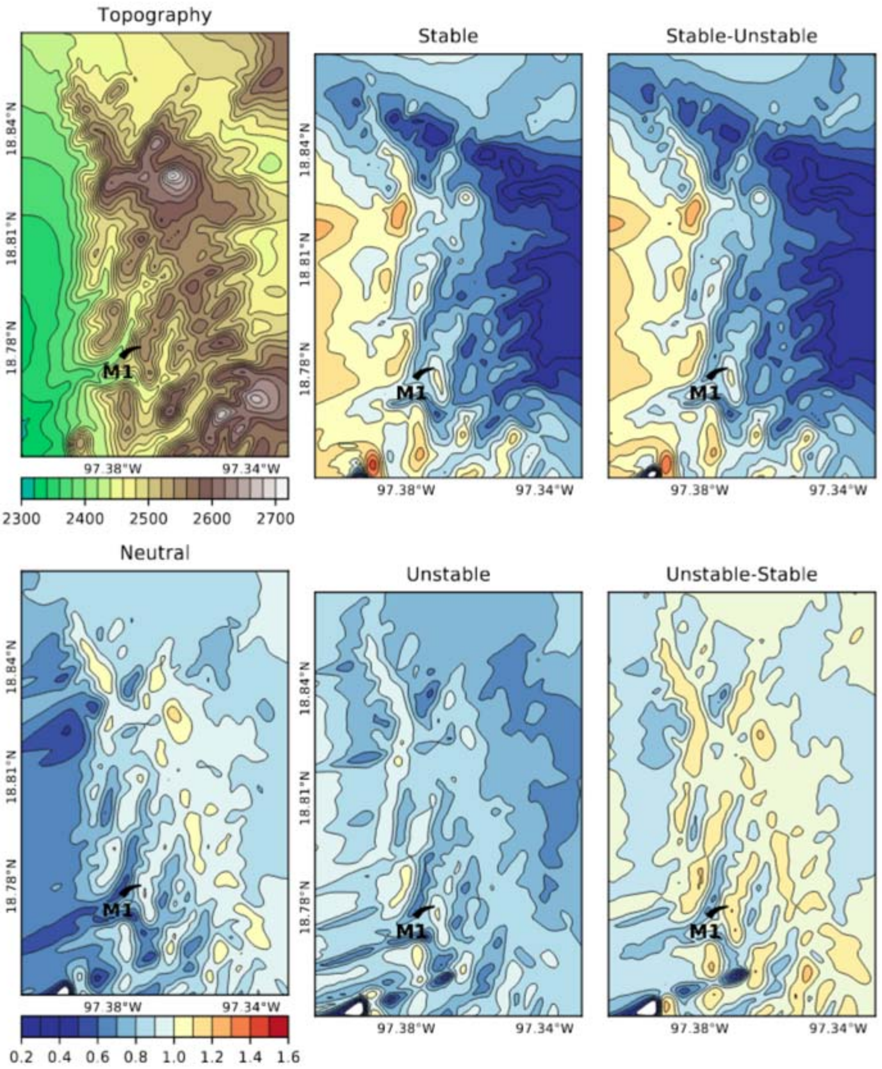

Figure 4.7
Wind speed-up contour plots at 80 m above the terrain for the neutral case and the 4 stability classes. Simulations using a constant geostrophic wind direction of ϕ=90° *(i.e. westward flow) and a geostrophic wind velocity of* $|\boldsymbol{u}_g|$=17.5 ms^{-1}. *The site has a preferential incoming wind direction of* ϕ=90°±10° *with around an 80 % of incidence per year. Speed-ups are relative to the reference mast M1. Contours of topography are shown for reference.*

with time series of mast observations to obtain the Annual Energy Production (AEP) density.

4.4.1 Methodology to consider ABL thermal stability

During a WRA study, near-surface wind time series (from mast measurements or, alternatively, from mesoscale model simulations) are classified based on wind direction sectors and velocity bins. Microscale model sector simulations, typically assuming neutral conditions, are then used to extrapolate the mast wind measurements over the region of interest; thus, accounting for topographic effects and providing several (yearly) averaged quantities of interest like: the mean wind speed, or the annual energy production (AEP). The diurnal cycle simulations allow adding a third dimension, the thermal stability class, to the reference methodology that always assumes neutral stability. To this end, wind time series are also classified based on thermal stability based on temperature and heat fluxes time series.

The proposed methodology entails two major aspects; the classification of the observational time series into thermal stability classes and the simulation of diurnal cycles. The former needs observed wind time series synchronised with temperature and heat fluxes time series. Using the diagnosed static thermal stability and surface heat fluxes, the wind time series can be classified into four thermal stability regimes: stable, stable-to-unstable transition, unstable and unstable-to-stable transition. Then, a wind-rose (a classification of wind velocity measurements into wind directions and velocity bins) can be constructed for each thermal stability class.

On the other hand, one time instant representative of each stability class can be extracted from the diurnal-cycle simulations as done in Section 4.3.3 (process applied to each wind direction diurnal cycle simulation). The WRA procedure continues with the calculation of the mean wind speed and AEP fields for each of the four thermal stability classes, *i.e.* using the corresponding wind-rose. Finally, the percentages of occurrence of each stability class are used to weight and sum previous results and, to provide the mean wind speed and the AEP density fields for the site. As in the neutral case, model outputs are combined to obtain the AEP by calculating the mean wind power density (WPD) at each point of the computational domain, which is given by

$$WPD = \frac{1}{2}\rho\overline{\boldsymbol{u}}^3$$

where ρ is the air density, and the over-lined term denotes the expected value of the cube of the wind velocity.

4.4.2 Results for the Puebla site

This section presents and compares results of two WRA studies for the Puebla site, one using neutral stratified simulations and other using the methodology proposed in the previous section. The validation and comparison of both methodologies uses approximately 1 year of synchronous wind measurements from 7 masts at 80 m height.

The right plot in Figure 4.8 shows the M1-M7 masts locations where M1 is used as reference and the other 6 masts are used for validation of model results. Because data is confidential and not publicly available, results are shown as normalised values. Unfortunately, the dataset does not contain heat fluxes and temperature measurements. This forced us to find an alternative way to classify the wind time series into thermal stability classes and to quantify each frequency of occurrence. This limitation has been circumvented by running the WRF-ARW model for the validation period. Thus, WRF-ARW simulations allowed us to obtain the ground heat fluxes, the surface heat fluxes and vertical profiles of θ at the area of interest. The obtained percentages of occurrence of each stability class are: 37.0 % stable, 8.5 % stable-to-unstable transition, 28.0 % unstable and 26.5 % unstable-to-stable transition. Figure 4.8 shows the ratios of the annual average speed-up and the AEP density at 80 m height between the diurnal cycle and the neutral methodologies. Note that results present an east-west pattern, very similar to the stable stratified pattern seen in Figure 4.7, because easterly winds are very dominant (80 % of frequency). So, in the present test case, the stable stratification wind distribution, with a weight of 37.0 %, has a dominant effect over the averaged results observed in Fig. 4.8.

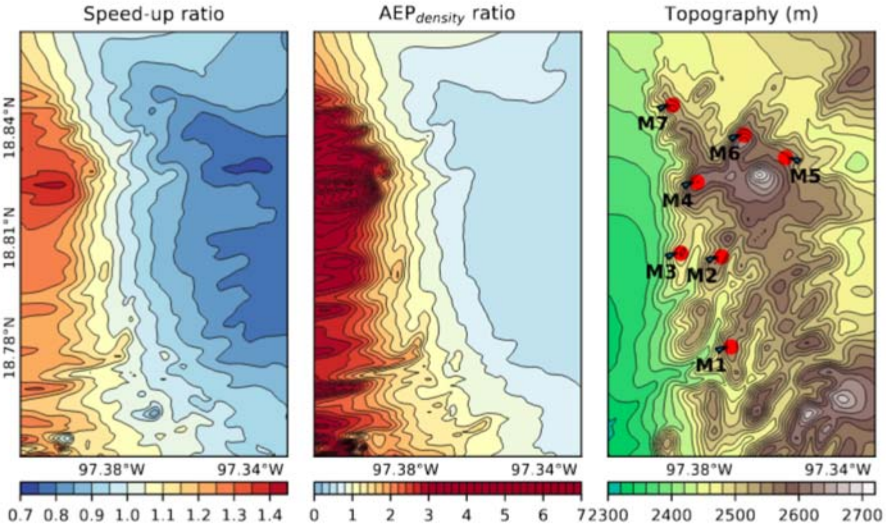

Figure 4.8
Left: ratio of the annual average speed-up at 80 m height between the diurnal cycle and the neutral WRA results. Middle: same for AEP density. Right: topography contours and locations of masts M1-M7. Mast M1 is used as the reference for speed-up computation, masts M2-M7 are used for validation.

For validation purposes, we define the AEP density normalised with respect to the mean measured AEP density of all masts:

$$AEP'(x,y) = \frac{AEP(x,y)}{\frac{\sum_{n=M1}^{M7} AEP_n}{N}} \tag{4.10}$$

where AEP_n is the annual energy production calculated using the wind measures in mast n, and N is the total number of masts. The percentage error (PE) of AEP at each mast (n) is defined as:

$$PE_n = 100\left(1 - \frac{AEP_n}{AEP_{Simulated_n}}\right) \tag{4.11}$$

Figure 4.9 presents the results of both metrics. The graph on the top shows that the thermal methodology improves the prediction of the AEP distribution at this concrete location, showing an

	M2	M3	M4	M5	M6	M7
Obs	1,09	1,26	1,30	0,48	0,76	1,11
Neutral	1,05	0,82	1,11	0,89	1,27	0,93
Diurnal CYCLE	0,92	1,16	1,42	0,39	0,75	0,94

	M2	M3	M4	M5	M6	M7	MAPE
Neutral	-3,93	-53,48	-17,01	45,63	40,20	-20,27	30,09
Diurnal CYCLE	-18,94	-7,99	8,64	-22,59	-0,64	-19,03	12,97

Figure 4.9
Top: validation at masts M2-M7 using normalised AEP density (eq. 4.10). Observations in black, results for the neutral case in blue, results for the diurnal cycle strategy in orange. Bottom: percentage error (eq. 4.11) at masts M2-M7 for neutral (blue) and diurnal cycle (orange) WRA cases. The mean absolute percentage error (MAPE) for all masts are 30.09 and 12.97% for the neutral and diurnal cycle strategies respectively.

AEP distribution remarkably closer to observations. Masts M2 and M3 offer an example of that; both masts are installed in two almost parallel hills (see right plot in Figure 4.8) where M3 is at lower height and at the west of M2. There, neutral stratified simulations predict a decrease of AEP density; in contrast, measurements and the proposed thermal methodology show an increment. The bottom graph in Figure 4.9 shows that at masts M3, M5 and M6, the PE of AEP is close to 50% when considering the neutral stratified methodology. In contrast, the proposed methodology predicts the AEP at these masts with a PE less than a 22%, i.e. reduces the error significantly. In addition, the mean absolute percentage error ($MAPE = \sum_n |PE_n|/N$) decreases from 30.1% to 13.0% respect to the neutral methodology.

4.5 Application 2: Mesoscale tendencies 1D approach

The simulation of realistic ABL conditions is of special interest for the wind energy and other applications. As introduced previously, dynamical coupling methodologies between mesoscale and microscale models are a major approach that can be used to WRA or to forecast. Certain methodologies directly introduce time-varying mesoscale model profiles as boundary conditions for the CFD RANS model; Castro et al. [2014] and Veiga Rodrigues et al. [2016] are two examples of this. Sanz-Rodrigo et al. [2017] proposed an alternative approach based on the GABLS3 benchmark [Bosveld et al., 2014a; Holtslag, 2014]. The methodology encompasses the extraction of mesoscale tendencies (forcings) from MMM models and their introduction as source terms within the CFD governing equations. This Section revisits the GABLS3 benchmark following Sanz-Rodrigo et al. [2017] and using the 1D precursor Alya-CFDWind model. This case serves for validation purposes and as a good starting point to simulate diurnal cycles using dynamical mesoscale information.

The GABLS3 benchmark is part of the Global Energy and Water Exchange (GEWEX) Atmospheric Boundary Layer Study (GABLS) framework, where GABLS1 [Cuxart et al., 2006] and GABLS2 [Svensson et al., 2011] precede it. The general objective of GABLS is to improve the representation of the atmospheric boundary layer in regional and large-scale atmospheric models [Holtslag, 2014]. To this end, the GABLS3 benchmark revisited for wind energy [Sanz-Rodrigo et al., 2017] stablished the framework to benchmark both, single-column models (which are used by meteorological models to parameterise the ABL) and CFD models coming from the wind energy sector. Concretely, GABLS3 analyses a real diurnal cycle with a strong nocturnal low-level jet (LLJ) at the Cabauw Experimental Site for Atmospheric Research (CESAR), located in the Netherlands.

4.5.1 Methodology

Table 4.2

WRF output processed variables used to drive the GABLS3 diurnal cycle.

WRF output processed variables	
One point variables	
T_2	$2m$ Temperature
T_s	Skin Temperature
u_*	Friction velocity at the surface
h_{sfc}	Kinematic Upward sensible heat flux at surface
Column variables	
θ	Potential Temperature
θ_{adv}	Potential Temperature Advection
U	Velocity U-comp.
U_{adv}	Advective momentum U-comp.
U_g	Geostrophic wind U-comp. $= (1/fc)$ Pressure gradient V-comp.
V	Velocity V-comp.
V_{adv}	Advective momentum V-comp.
V_g	Geostrophic wind V-comp. $= (1/fc)$ Pressure gradient U-comp.

Following the Sanz-Rodrigo et al. [2017], the mesoscale quantities come from the WRF model and have been spatial and temporally averaged to filter out microscale fluctuations. Table 4.2 presents the list of the extracted variables classified into point (at one single level) and column variables (for the whole atmospheric column). This set of variables can also be classified depending on their use; for the initial condition, as an additional source term, or used to calculate near surface and bottom wall values:

- **The initial condition group** is formed by U,V and θ profiles; the fields are linearly interpolated in the vertical coordinate, above first WRF model level, to the 1D model nodes. Because the MMM first level is usually found at around 10 m height or above, these fields are extrapolated from there and down to the surface using MOST [Monin, Obukhov, 1954].

- **The additional CFD source terms** are the advective terms θ_{adv}, U_{adv} and V_{adv}, and the geostrophic wind components U_g and V_g. The last two terms are introduced into the governing momentum equations as a pressure gradient $\nabla p = 2\omega \times \boldsymbol{U_g}$. As it is done for the initial conditions, these profiles are vertically interpolated, and these are also linearly interpolated over time to be provided to the 1D model at each integration time step ($\delta_t = 30\ s$).

- **The time-dependent wall values and near surface values** for the initial conditions are extrapolated using MOST and the point variables T_2, u_* and h_{sfc}. The T_s is not used because corresponds to the first soil layer in contact with the atmosphere. The properties of this layer are related to the soil and the evolution of the temperature is a bit different regarding from the air just above.

4.5.2 Results

Figure 4.10 compares the time-height contour plots of GABLS3 observations, WRF simulation and 1D precursor Alya-CFDWind model including mesoscale tendencies. The plots show that the ABL temporal evolution is correctly simulated and the obtained results are in good agreement with both, observations and WRF. Although the LLJ is slightly underestimated, it has been predicted at the correct height and approximately with the same duration and extension as in the observed. In addition, results shown in Figure 4.10 are in good agreement with those presented in Sanz-Rodrigo et al. [2017]. We have also evaluated the relative impact of the mesoscale tendencies in the simulation by separately introducing each forcing, and different combinations of these (not shown). As found in Sanz-Rodrigo et al. [2017], results showed that near the surface, the geostrophic pressure gradient terms become dominant in the momentum equations. In contrast, the momentum advective terms become more important at elevated heights. Thus, the geostrophic pressure gradient and the

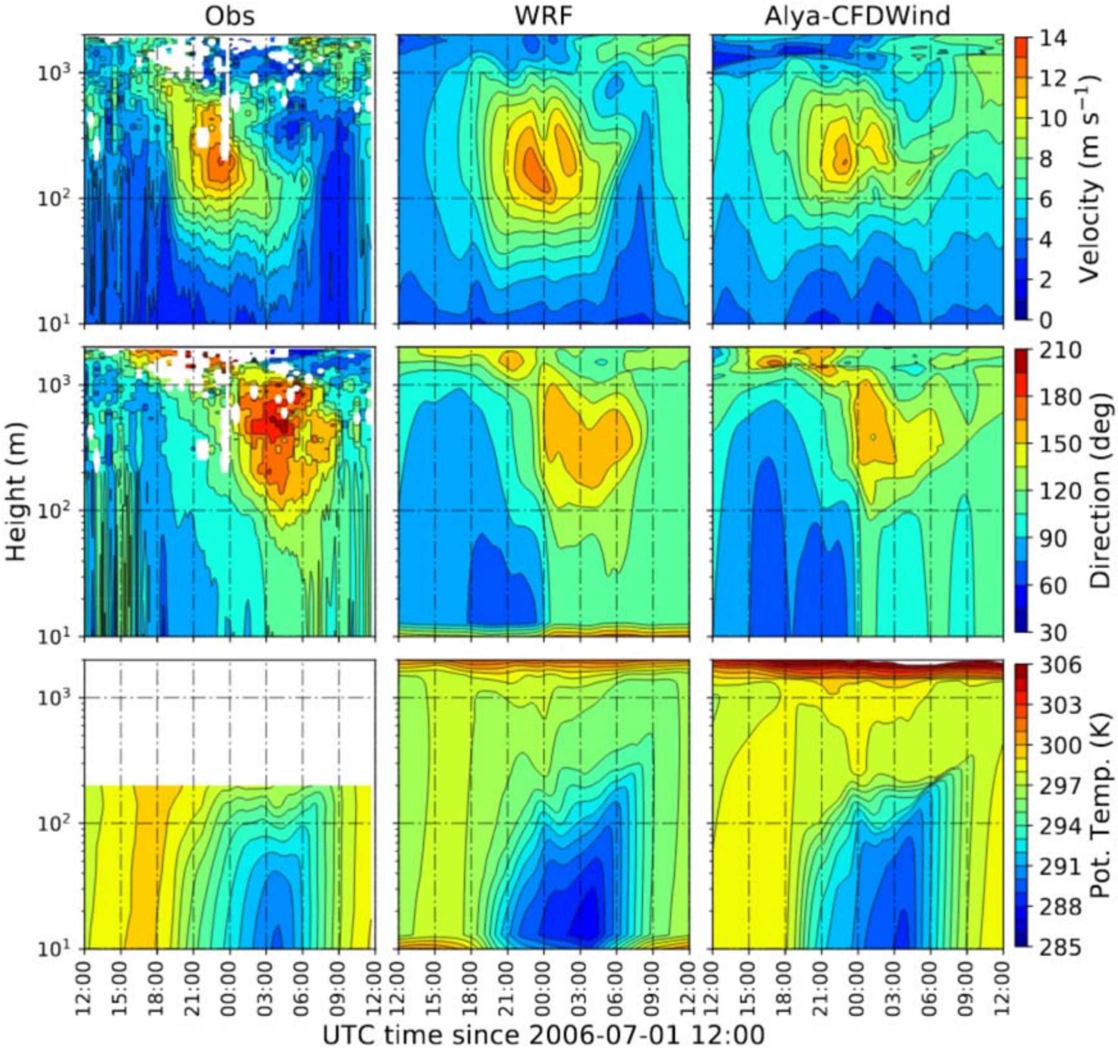

Figure 4.10
GABLS3 time-height contour plots of wind velocity (top), wind direction (middle) and potential temperature (bottom) for the observations, WRF-ARW simulation and 1D AlyaCFD-Wind precursor including mesoscale tendencies.

momentum advective terms are the main forcing terms needed to simulate the dynamic evolution of the ABL using tendencies.

4.6 Summary and discussion

This Chapter has introduced a methodology to simulate diurnal cycles with a CFD-RANS model and the following selection of time instants representative for each stability regime. Previous to the simulations, a single-column 1D precursor simulation generates time-dependent inflow and bottom boundary conditions for the model. The vertical profiles of $\boldsymbol{u}$ are also prescribed at the outflow boundaries (Dirichlet outflow condition) to avoid problems when imposing pressure. The computation of a 3D diurnal cycle, at a grid resolution (for the region of interest of 6.4×13 km^2) of

δx=δy=100 m, has taken around 15 h CPU time using 256 cores for 28 h of real time simulation (18,000 time integration steps). The simulations have used a variable integration time step δt, very small at the beginning (δt <1 s) to assimilate the initial conditions and progressively growing until δt_f ≈6 s. The methodology has been applied to wind resource evaluation over complex terrains.

The WRA application entails two major aspects; first, the construction of one wind-rose for each thermal stability regime (stable, stable-to-unstable transition, unstable and unstable-to-stable transition) using observed wind time series together with temperature and heat fluxes time series. Second, the simulation and discretisation of the diurnal cycles. Finally, the methodology uses the wind-roses and the percentages of occurrence of each stability regime, to frequency-weigh the stability classes representatives and obtain annually averaged values of speed-ups and energy density production. The methodology has been tested and validated on a location in the Mexican state of Puebla, where we had access to a long-period dataset of 7 met-masts. Unfortunately, the dataset did not contain heat fluxes and temperature data. Thus, the wind data measurements have been classified into thermal stability classes using mesoscale simulations of the Weather Research and Forecasting model for the validation period, from which the frequency of each stability class has been calculated. Finally, the annual energy density production (AEP) and the annual average speed-ups have been calculated and compared against the neutrally stratified case. Results have shown that the introduction of thermal stability has decreased the AEP prediction error with respect to the neutral stratified simulations (from 30.09 to 12.97%) and have shown an AEP distribution remarkably closer to observations.

This WRA study has shown the potential of the proposed thermal methodology. Although results are encouraging, there are some aspects that should be faced in future studies. First, the diurnal cycles should be representative of the region under study. This could be achieved linking the methodology with statistical weather classification techniques [e.g. Badger et al., 2014], introducing different diurnal cycles for each wind velocity direction. Second, a more suitable temperature distribution should be imposed over the ground; for example a ground temperature field depending on the angle of insolation and on terrain elevation. Third, the thermal model accounts for Coriolis and buoyant forces, that introduce a dependence of the speed up distribution on the velocity modulus. We believe that the proposed methodology could improve simulating several wind velocities for each wind direction. This latter approach would need a larger number of simulations, *i.e.* increasing the computational cost of the methodology; however, the rapid increase in computational power can provide a more suitable framework to introduce this kind of approaches in a near future.

CHAPTER 5

A physical-statistical downscaling strategy

This chapter is an elaboration of the material in

Barcons, J., Folch, A., **in review**. A wind field downscaling strategy based on domain segmentation and transfer functions. Wind Energy

5.1 Introduction

This chapter presents an alternative cost-efficient wind field downscaling strategy that introduces microscale information from pre-computed CFD simulations into a mesoscale solution/forecast. The downscaling methodology combines a domain segmentation technique with transfer functions, a concept originally proposed for microscale wind resource assessment over regional scales by Sanz-Rodrigo et al. [2010]. Here the concept of transfer functions is extended to forecast near-surface high-resolution winds by combining a mesoscale forecast with a set of microscale pre-computed CFD reference simulations. This adds little extra cost to the operational model chain and supposes a compromise between simpler mass-consistent downscaling and dynamic NWP-to-CFD coupling, too costly in terms of operational forecast yet. Section 5.2 introduces the downscaling methodology based on domain segmentation and transfer functions. A case study for validation is presented in Section 5.3 for a site in the Mexican state of Puebla, characterised by a very complex orography. This site has been instrumented with eleven 80 m height meteorological masts by a wind energy company with a prospective scope. Section 5.4 shows the validation results for a 9-month period, used to quantify the gain in the downscaled wind field with respect to the mesoscale WRF forecast depending on wind intensity and atmospheric stability. Section 5.5 applies the diurnal cycle simulations and the thermal stability regimes classification to the downscaling. Finally, Section 5.6 contains a summary and a discussion on the limitations of the methodology and on its future improvements.

5.2 Methodology based on domain segmentation and transfer functions

We propose a downscaling methodology that links the different components of the model chain using a combination of domain segmentation and transfer functions [Sanz-Rodrigo et al., 2010]. This methodology constructs a downscaled wind from a WRF wind field (forecast) and a set of pre-computed steady-state RANS microscale reference solutions from Alya-CFDWind. In this way, the resulting downscaled wind field keeps the mesoscale pattern but, at the same time, incorporates the microscale fluctuations at a local scale. This methodology is very attractive from the point of view of operational forecasting because the downscaling is performed for the area(s) of interest as a post-process step. Thus, as opposed to a pure CFD dynamical downscaling or to a simpler mass-consistent approach, our methodology supposes no extra computational cost during operations.

The starting point of the downscaling is a WRF simulation (forecast) plus a set of pre-computed Alya-CFDWind runs covering the downscaling target area(s). Each of these Alya-CFDWind reference simulations ($\boldsymbol{U}_{CFD}^{\phi}$) is computed a priori imposing a geostrophic wind direction ϕ prescribed at the top of the computational domain. The 360° possible geostrophic wind directions are discretised assuming bins of constant width, *e.g.* a set of 16 pre-computed simulations results on a 22.5° geostrophic (top) wind binning. However, note that because of Coriolis and terrain effects, winds from Alya-CFDWind twist with height, resulting on non equally-spaced bin direction increments as height decreases from top to surface. The downscaling methodology involves a series of steps (Figure 5.1):

1. The first step consists on constructing a series of 2D terrain-following grids Ω_{2D} at user-defined elevations above the terrain (*e.g.* z_t =10, 20 and 50 m) where the downscaled wind will actually be computed. Both the mesoscale (WRF) and the microscale (pre-computed Alya-CFDWind) wind fields need to be interpolated to the nodes of these Ω_{2D} grids.

2. Each of these Ω_{2D} planes is then decomposed on a series of structured segments S_{ij} centred at the position of each WRF grid mass-point. The area of the segments is, therefore, $2\Delta x_{WRF} \times 2\Delta y_{WRF}$, where Δx_{WRF} and Δy_{WRF} are the WRF cell dimensions. This defines regions of overlap between segments (*i.e.* $\cup S_{ij} = \Omega_{2D}$ and $\cap S_{ij} \neq \emptyset$) to allow obtaining a smooth solution in the domain reconstruction step. The purpose of this domain segmentation is to have a reference mesoscale wind direction θ^{ij}_{WRF} (that corresponds to the WRF grid mass-point wind direction) for each segment S_{ij}.

3. For each segment S_{ij} and time instant t, the direction θ^{ij}_{WRF} is used to build a segment microscale solution ($\boldsymbol{U}_{ij}$) by performing a linear interpolation between the two pre-computed runs $\boldsymbol{U}^{\phi_1}_{CFD}$ and $\boldsymbol{U}^{\phi_2}_{CFD}$ that bound θ^{ij}_{WRF} (*i.e.* $\theta^{ij}_{WRF} \in [\phi_1, \phi_2]$). In this way, and by construction, the average microscale wind direction over each segment $\boldsymbol{U}_{ij}$ coincides with that of the mesoscale θ^{ij}_{WRF}.

4. Small variations of θ^{ij}_{WRF} can occur across adjacent segments S_{ij}, resulting on small differences on wind velocity and direction at nodes in the overlapping regions. In order to have a smooth transition between these adjacent $\boldsymbol{U}_{ij}$ solutions, a smoothing operation is performed at the overlap regions between segments. In particular, a linear weighted interpolation is considered for each horizontal wind component. The blending of all segment microscale solutions $\boldsymbol{U}_{ij}$, on both latitudinal and longitudinal directions, results on an intermediate microscale field $\boldsymbol{U}_{inter}$.

5. Finally, the transfer functions are applied to scale the modulus of the microscale wind at each point of the Ω_{2D} planes as:

$$|\boldsymbol{U}_{down}| = f|\boldsymbol{U}_{WRF}| = \frac{|\boldsymbol{U}_{inter}|}{< |\boldsymbol{U}_{inter}| >_{\Re}} |\boldsymbol{U}_{WRF}| \tag{5.1}$$

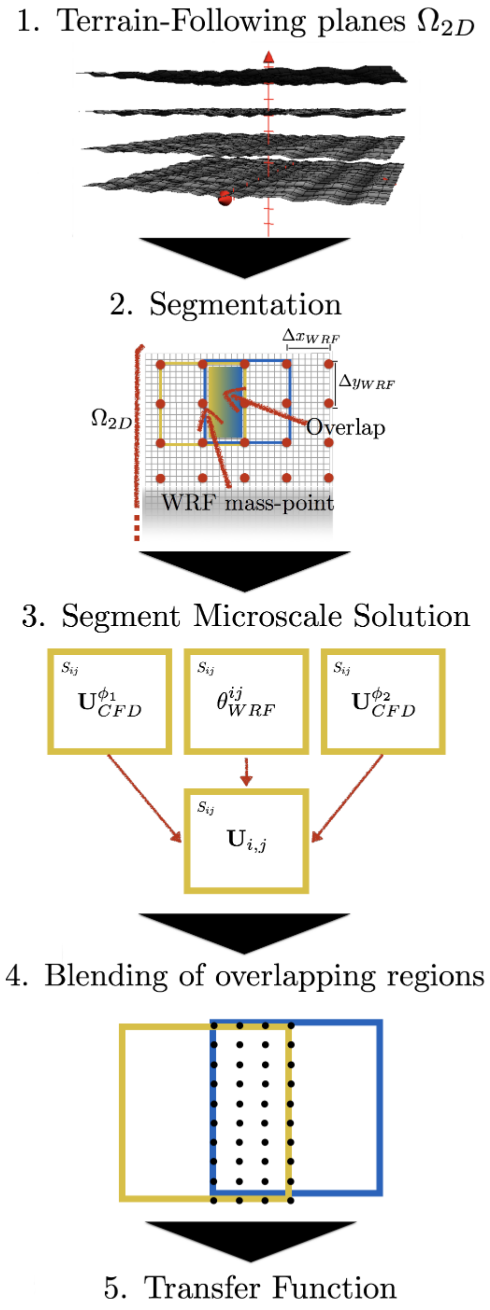

Figure 5.1
Steps of the downscaling methodology giving the wind field on a series of terrain-following Ω_{2D} planes using domain segmentation and transfer functions.

where $\boldsymbol{U}_{down}$ is the resulting downscaled wind velocity, $f(x, y, z, t)$ is the point-dependent transfer function at time t, $\boldsymbol{U}_{WRF}$ is the WRF wind velocity modulus interpolated at the point, $\boldsymbol{U}_{inter}$ is the microscale wind velocity resulting from step 4, and $< \boldsymbol{U}_{inter} >_{\Re}$ is the spatial average of $\boldsymbol{U}_{inter}$ over a radius of influence $\Re$. Note that, by construction, when $\Re \to 0$ the downscaled wind velocity tends to that of WRF ($\boldsymbol{U}_{down} \to \boldsymbol{U}_{WRF}$). In contrast, as $\Re$ increases, the transfer functions incorporate to the downscaled field the local wind fluctuations caused by microscale topographic forcing.

Some critical aspects of the methodology have to be mentioned. First, the horizontal resolution of the mesoscale model should be sufficiently coarse to avoid, as much as possible, a double counting of terrain forcing effects. It means that the WRF model should not account for the microscale flow characteristics that are already explicitly resolved by the Alya-CFDWind solver. Second, the domain segmentation technique is designed to guarantee that the downscaled field preserves locally the WRF wind direction on average (the mesoscale pattern). Third, the transfer functions are used to scale (correct) the WRF wind velocity modulus accounting for terrain speed-up and slow-down effects.

5.3 Validation case

5.3.1 Site description

The validation considers a site in the Mexican state of Puebla characterised by a very complex orography. The area is located at about 20 km south of Pico de Orizaba volcano (5636 m a.s.l., the highest Mexican peak) and near the town of Esperanza, on a plateau with an averaged elevation of 2400 m. The predominant yearly wind direction is westward, where east winds coming from the Gulf of Mexico pass first over a vast flat area and then, when approaching the region of interest, encounter a complex orography with high mountain slopes and channelling zones on the way up to the plateau.

This site was selected for validation because of access to a long-period dataset acquired by a private company during a wind resource prospection campaign. Wind data comes from a very dense network of 11 met masts (Fig. 5.2) instrumented with sonic anemometers at 40, 60, and 80 m height, with a total period of acquisition of 3 years (not synchronous in all masts). The acquisition frequency of sensors is of 1 Hz, with instantaneous values averaged over 10 min periods. For validation, the 9 month period from June 2013 to February 2014 is used, for which a continuous and synchronous record exists for all masts. The advantage is that to dispose of a dataset of such a spatial density over a long-period of time is unusual. However, the drawback is that met masts

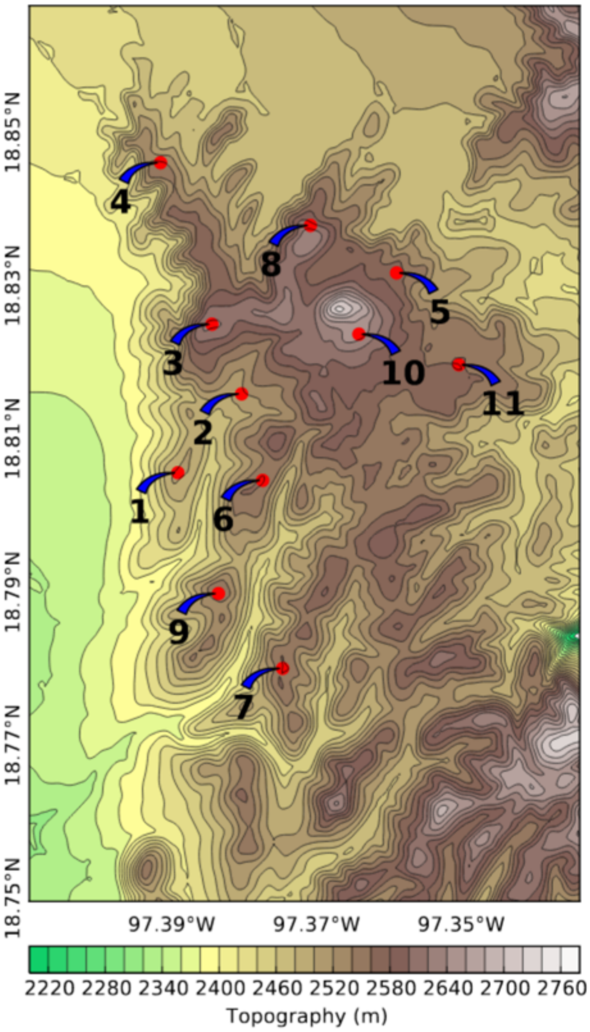

Figure 5.2
Elevation contours (in m a.s.l.) of the area of interest and location of the 11 met masts deployed for wind resource assessment. The area shown is 8×13 km^2.

were deployed at elevated zones, away from deep valley bottoms and channeling zones. This can constrain our model validation because no large differences are expected a priori between mesoscale and downscaled microscale winds at mast locations. Note that a similar problem would occur if using surface Automatic Weather Stations (AWS) because, typically, AWS are also deployed at locations where the mesoscale component of the wind dominates. This private dataset is confidential and, for this reason, period (yearly) absolute values of wind speed can not be shown throughout this Chapter. Wind values will be given normalised to the mean observed winds, with no absolute error differences shown.

5.3.2 WRF-ARW model setup

The WRF model was configured as summarised in Table 5.1. The simulated period (9 months) is covered by overlapping 48 h model runs, allowing 24 h for model spin-up and with a model output period of 30 min. Initial and 3-hourly boundary conditions for each run come from the European Centre for Medium-Range Weather Forecasts (ECMWF) operational deterministic model at 0.125° resolution [Persson, 2015]. Figure 5.3a shows the WRF computational domain and the topography contours at 3 km model resolution. The domain is centred near the Pico de Orizaba volcano, covering an area of 255 × 255 km^2.

Table 5.1
Configuration of the WRF-ARW model for the Puebla test case.

WRF-ARW configuration	
Model version	3.4.1
Initial and lateral BCs	ECMWF at 0.125° resolution
Domains	1
Horizontal grid resolution	3 km
Horizontal grid size	86 × 86
Vertical levels	60 levels, with top at 50 hPa
Simulation length	48 h (spin-up of 24 h)
Integration time step	20 s
Parametrization	**Scheme**
Microphysics	WRF single-moment 6-class (WSM6) [Hong, Lim, 2006]
Cumulus	Modified Kain-Fritsch (KF) [Kain, 2004]
Surface Layer	Eta Monin-Obukhov (Eta) [Janjić, 1996, 2001]
Land Surface	Unified Noah Land Surface Model (LSM) [Chen, Dudhia, 2001]
Planetary Boundary Layer	Mellor Yamada Janjic (MYJ) [Janjić, 1994, 2001]
Long-wave Radiation	Rapid Radiative Transfer Model (RRTM) [Mlawer et al., 1997]
Short-wave Radiation	Dudhia [Dudhia, 1989]

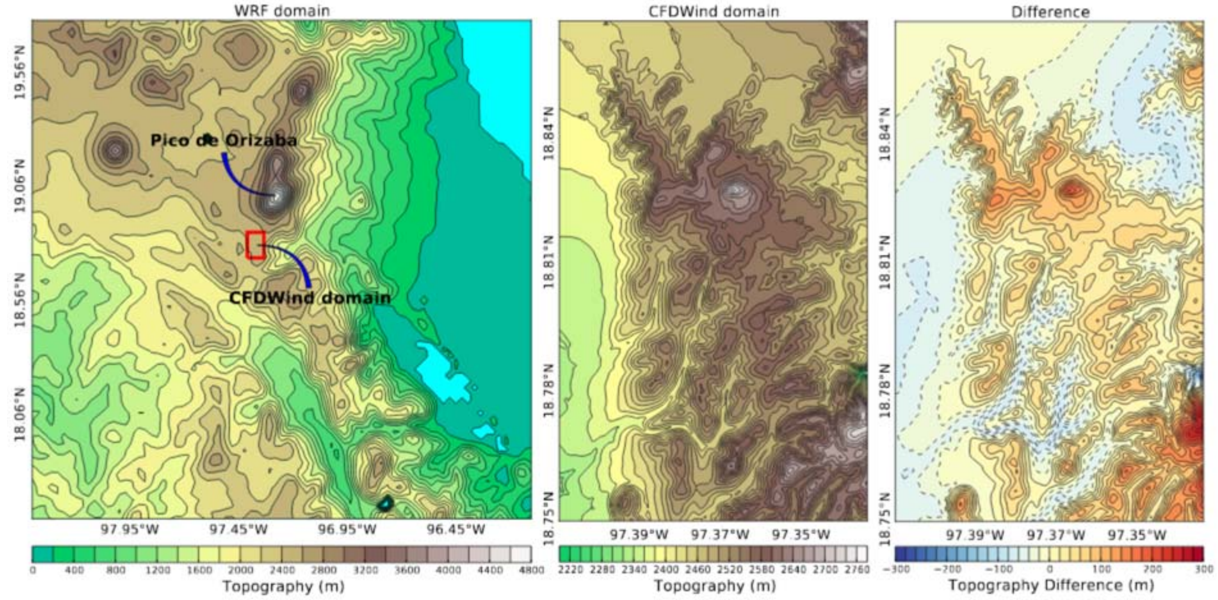

Figure 5.3
(a) WRF computational domain and topography contours (255×255 *km*^{2})*. (b) Downscaling area showing the ALYA-CFDWind topography contours* (8×13 *km*^{2})*. The red box in the WRF domain shows the location of the ALYA-CFDWind computational domain. (c) Topography differences between WRF (at 3 km resolution) and ALYA-CFDWind (40 m resolution).*

5.3.3 Alya-CFDWind model setup

The Alya-CFDWind computational domain (Figure 6.8) consists of an inner region of 8×13 km^2 at 40 m horizontal grid resolution surrounded by a transition zone in which the size of the elements increases up to that of the external buffer zone, having no topography and used to accommodate the incoming flow. Along the vertical direction, the structured grid extends up to 5.5 km above the ground, with 56 vertical layers growing geometrically in size from 1 m at surface to 250 m at top. The resulting computational mesh has around 12.5M grid points. The Coriolis force corresponds to that of a latitude 18.8° N, and the maximum mixing length is calculated automatically by the model depending on the wind velocity at top and the Coriolis force as in Apsley, Castro [1997]. Note that, for simplicity, neutral atmosphere is assumed at this stage. The pressure gradient $\nabla p = 2\rho\boldsymbol{\omega} \times \boldsymbol{u}_g$ is fixed over the whole domain, where $|\boldsymbol{u}_g|$ =17.5 m s^{-1} is the geostrophic wind vector, ρ is the air density, and ω is the Earth's angular velocity vector. With these conditions, one Alya-CFDWind simulation is performed for each reference direction (sector) of the geostrophic wind using 22.5° binning (*i.e.* 16 different runs were needed to scan all geostrophic directions). Assuming self-similarity, these pre-computed reference runs are then scaled and interpolated during the downscaling process depending on the WRF model outputs.

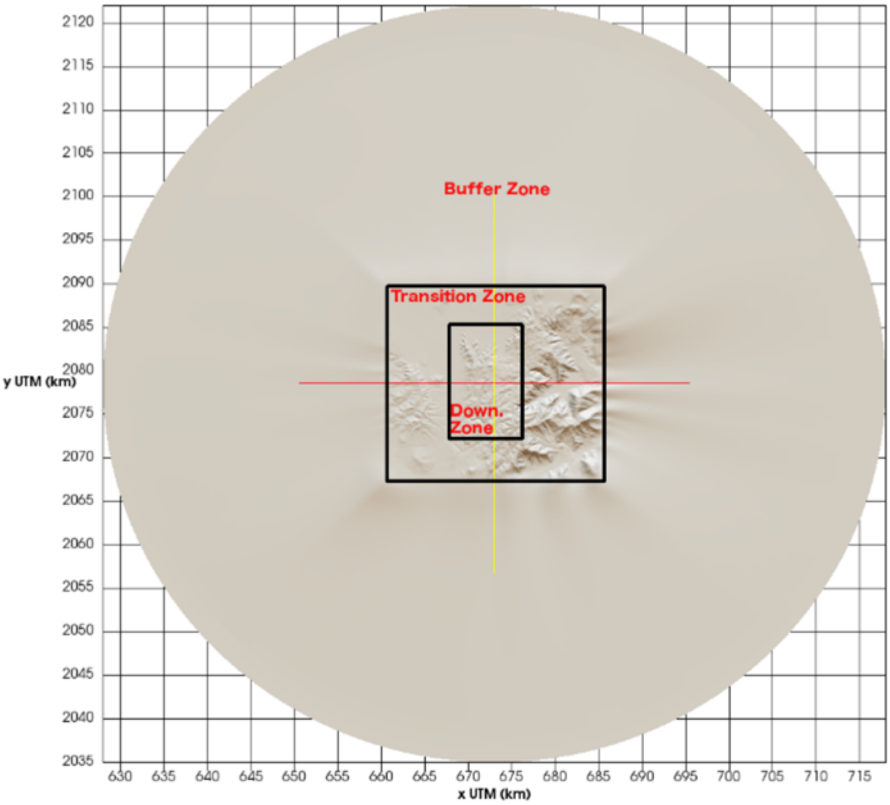

Figure 5.4
ALYA-CFDWind computational domain with 3 different mesh zones identified: a 8×13 *km*^{2} *zone at 40 m horizontal grid resolution (i.e. the downscaling area, see Fig. 5.3b), a transition zone of 5 km at north and south and 8 km and 10 km at west and east respectively, and an external flat buffer zone.*

5.3.4 Downscaling setup

The downscaling methodology described in Sect. 5.2 was applied every 30 min for each WRF model output at near-surface terrain-following levels of 10, 20, 40, 60, and 80 m (*i.e.* using 5 different Ω_{2D} planes for downscaling). In oder to assess the optimal radius of influence $\Re$ for the transfer functions (see eq. 5.1), the downscaling methodology was considered under four different cases of $\Re = 150$ m ($\Re_{150}$), $\Re = 250$ m ($\Re_{250}$), $\Re = 500$ m ($\Re_{500}$) and $\Re = 1000$ m ($\Re_{1000}$). As previously mentioned, this radius affects the weight given to the mesoscale and the microscale contributions on the resulting downscaled solution respectively.

5.3.5 Metrics for validation

The following metrics were used to validate quantitatively the downscaling methodology for all masts over the 9-month period:

1. Mean Error (ME) for wind velocity:

$$\mathrm{ME}(f,o) = \frac{1}{n}\sum_{i=1}^{n}(f_i - o_i) \tag{5.2}$$

   equivalent to the bias, the ME gives information of wether wind speed forecasts (f_i) are, on average, overestimating (positive values) or underestimating (negative values) observations (o_i).

2. Root Mean Square Error (RMSE) for wind velocity and direction:

$$\mathrm{RMSE}(f,o) = \sqrt{\frac{1}{n}\sum_{i=1}^{n}(f_i - o_i)^2} \tag{5.3}$$

   gives additional information about the deviation of forecasts from observations.

3. Skill Score (SS%) for wind velocity and direction:

$$\mathrm{SS\%}(f,r,o) = 100\left(1 - \frac{\mathrm{MSE}(f,o)}{\mathrm{MSE}(r,o)}\right) \tag{5.4}$$

   where MSE is the Mean Square Error. The SS% can be interpreted as the accuracy of the model under evaluation (f) relative to a reference model (r). This index penalises large differences between forecasts and observations (o).

5.3.6 Atmospheric stability classification

The mesoscale WRF wind fields implicitly include atmospheric stability information. In contrast, the pre-computed microscale Alya-CFDWind fields assume neutral stability and account for local-scale terrain effects. For this reason, differences in the downscaling skill scores could exist under different atmospheric stability conditions and wind intensities. In order to desegregate these effects, three different stability classes are distinguished as:

$$\begin{cases} & z/L & > 0.1 & \text{stable} \\ 0.1 \geq & z/L & \geq 0 & \text{near neutral} \\ & z/L & < 0 & \text{unstable} \end{cases}$$

where z is the height of the layer used to calculate L, the Obukhov length from the Monin-Obukhov

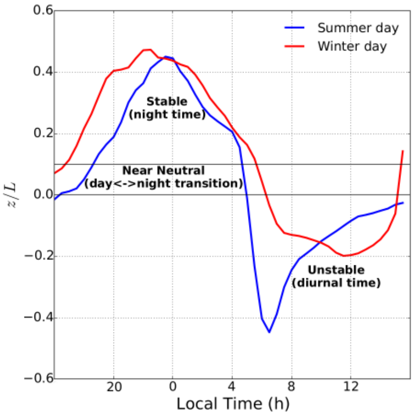

Figure 5.5
Values of z/L during a summer and a winter cloud-free diurnal cycle. The specific days are 8 August 2013 and 5 January 2014 respectively. The different stability regimes are shown.

similarity theory [Monin, Obukhov, 1954]:

$$L = \frac{\rho c_p u_*^3}{\kappa \alpha |\boldsymbol{g}| q_{flux}}$$

where c_p is the air heat capacity, ρ is the air density, u_* is the friction velocity, κ is the von Kármán constant, α is the thermal expansion coefficient, and q_{flux} is the surface heat flux. Figure 5.5 shows the dimensionless stability parameter z/L during two cloud-free 24 h periods. Note that z/L changes its sign (from positive to negative) around sunrise, when buoyancy forces foster air mixing and the atmospheric boundary layer grows in height. This period, which ends after noon, is typically dominated by convection. In contrast, z/L becomes positive during the evening, where convective forces near surface almost vanish and the atmosphere passes through a short period of near neutral stability.

5.4 Validation results

5.4.1 Qualitative evaluation

Before performing a full-period quantitative validation, it is illustrative to show the downscaling results for a particular 24 h period characterised by a persistent easterly situation, the predominant wind direction over the region. In the methodology, the resulting downscaled wind direction comes exclusively from the domain segmentation and overlapping processes. The RMSEs values (all measuring heights computed together) for this particular day are 10.4° for the downscaled field in front of 11.1° for WRF. On the other hand, the near-surface wind velocity fields after applying the transfer functions depend on the value of $\Re$. Table 5.2 lists the values of RMSE and SS% obtained for different values of $\Re$. As observed, for this particular day, the worst skill score is obtained with the radius of influence of $\Re_{1000}$ because the transfer-function produces an exaggerated overestimation of the wind velocity. Conversely, the lower RMSE and the best skill score are obtained with a radius of influence of $\Re_{500}$. This value will be assumed throughout this section.

Table 5.2
Values of RMSE (in m s^{-1}) and Skill Score (SS%) for the 24 h period selected using 30 min data from the 11 met masts. WRF model is used as reference model in the SS% calculations.

	RMSE	**SS%**
WRF	2.6	0.0
$\Re_{150}$	2.6	0.9
$\Re_{250}$	2.5	4.1
$\Re_{500}$	2.4	6.0
$\Re_{1000}$	3.1	-18.3

For illustrative purposes, Figure 5.6 compares the 10 m wind velocity fields from the pre-computed Alya-CFDWind model, the WRF model and the downscaling methodology. This Figure highlights the local terrain information contained in the pre-computed microscale solution (Fig. 5.6a) in front of the smoother field provided by the much coarser WRF model at 3 km resolution (Fig. 5.6b). Clearly, the resulting downscaled field (Fig. 5.6c) contains the general mesoscale pattern but modulated by the local-scale terrain information added by the CFD model. Figure 5.7 compares the mesoscale and the downscaled wind fields at the same time instant over a small region of about 3×3 km^2 (one WRF cell size) that includes Mast-7. Note how the downscaled field speeds-up the wind flow at the top of the ridges while, in contrast, winds slow-down and rotate at valleys and channeling zones. For this particular time instant, the differences in wind direction and velocity between WRF and the downscaled field at the valley (red dot in Fig. 5.7) are of 77.8° and 3.3 m s^{-1} respectively. These differences are mainly due to the terrain channeling effects. Figure 5.8 shows the differences between the downscaled and the WRF mesoscale wind velocities depending on the

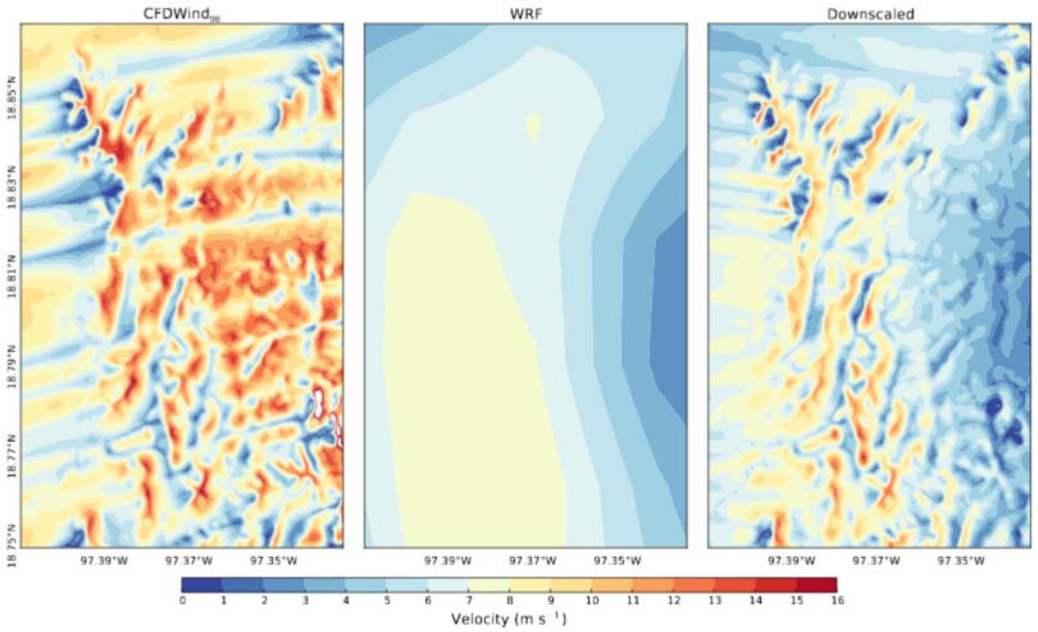

Figure 5.6
Wind velocity at 10 m height on 3 July 2013 at 6 a.m. (LT). (a) Pre-computed ALYA-CFDWind solution u^{90}_{CFD} *(i.e. assuming a* 90° *geostrophic wind direction), (b) WRF at 3 km resolution and, (c) resulting downscaled field assuming a value of* $\Re = 500$ *m for the transfer functions.*

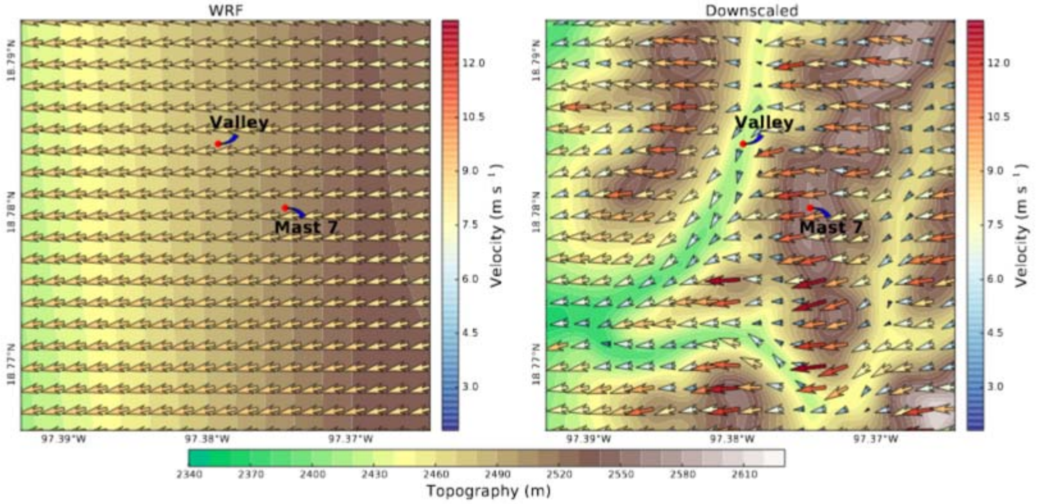

Figure 5.7
(a) WRF wind velocity vectors at 10 m height on 3 July 2013 at 6 a.m. (LT). (b) wind field after downscaling using a radius of influence of $\Re_{500}$*. Plots cover an area of* 3×3 *km*^{2} *that corresponds to one WRF cell and include Mast-7 (red dot) and a small valley 500 m west (not visible at mesoscale resolution).*

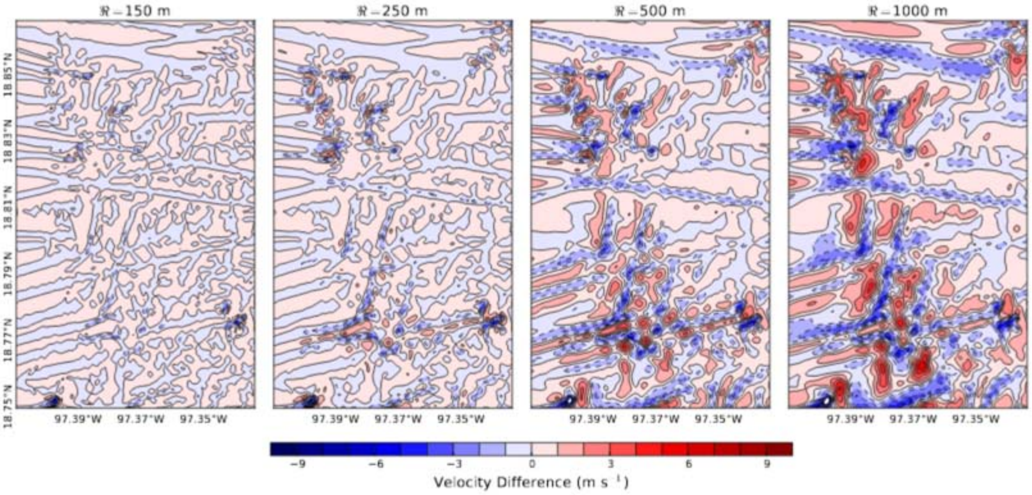

Figure 5.8
Wind velocity differences between the downscaled and the WRF fields considering a radius of influence of 150, 250, 500, and 1000 m from left to right. Results at height 80 m above the terrain for 3 July 2013 at 6 a.m. (LT).

value of $\Re$. As observed, the smaller the value of $\Re$ the more the downscaled velocity field coincides with that of WRF. In this particular example, $\Re_{150}$ differences are less than 1 m s^{-1} for all points of the domain. In contrast, as $\Re$ increases, the transfer functions incorporate more local wind velocity fluctuations around the mean mesoscale component and, in consequence, more local terrain effects appear in the downscaled field. Figure 5.9 shows the 3 July 2013 time series of results at Mast-7 site (80 m height). During this particular day, the mesoscale forecast did not capture well the observed wind variability. Comparing WRF and different $\Re$ cases, the downscaled results follow the mesoscale pattern adding a correction factor that depends on the terrain and on the value of $\Re$ used. In this location (Mast-7), the different $\Re$ cases result on a wind velocity increase and little direction variations, with a maximum wind veering of about 5°. In contrast, Figure 5.10 shows the same time series of results but at the valley (valley point in Fig. 5.7), where no observations are available. At this location, the downscaling corrections are much more pronounced, with the transfer functions decreasing the mesoscale velocity by 10-35% (depending on $\Re$) and a wind veering correction of about 8° along the period (at 80 m height above terrain).

In summary: the downscaled fields contain the mesoscale pattern; the smaller the value of $\Re$ the more the downscaled velocity field tends to that of WRF; the corrections introduced by the downscaling methodology increase as one approaches the ground surface; valleys and channeling zones show larger differences than elevated locations.

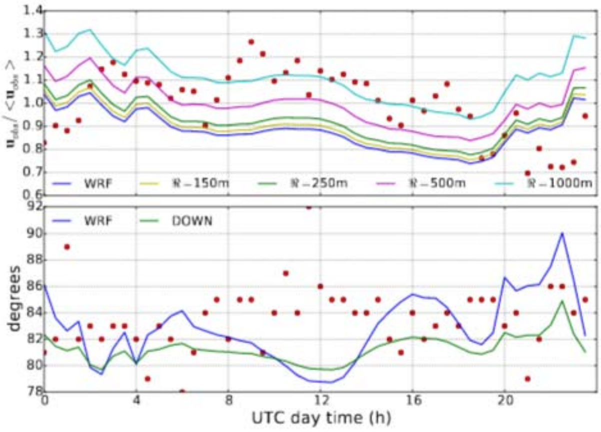

Figure 5.9
Time series of wind velocity and direction at Mast-7 during 3 July 2013. Results at 80 m height. Wind velocity is normalised to the day-mean of observations. Red dots represent observations (averaged over 30 minutes), blue lines show the WRF forecast and the rest of lines show the downscaled values for different radii of influence, from 150 to 1000 m.

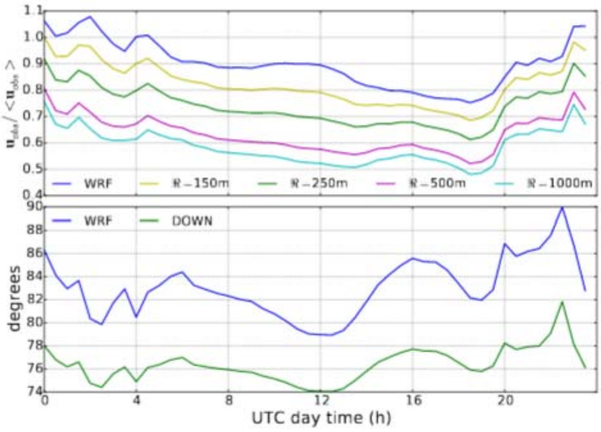

Figure 5.10
Same than in Fig. 5.9 but at the valley point, where no observations exist.

5.4.2 Quantitative validation

A couple of comments are necessary before performing the quantitative validation of the downscaling methodology for the 9-month period. First of all, substantial differences between mesoscale WRF forecasts and 10 min averaged mast observations can occur due to a number of reasons. Causes of erroneous forecasting intervals may include WRF model phase errors (*e.g.* delay/advance on the predicted arrival time of a front, the starting point of a convective event, thermal winds, etc.), loose of the mesoscale pattern by the model, or wind direction meandering during periods of low wind intensity. Regardless of its origin, model errors generated in the mesoscale range are dragged down to the microscale and could offer a blurred vision of the downscaling methodology. For this reason, we filtered out from the dataset all the velocity-direction pairs in which the WRF direction errors at masts were larger than 60° and/or the observed velocities were less than 4 m s^{-1}. On the other hand, it has already been pointed out that masts were deployed (for wind resource assessment purposes) at locations where the synoptic and mesoscale component dominate. As a result, small differences between the mesoscale and downscaled fields are expected at the sites used for validation.

Tables 5.3 and 5.4 show the validation results for the 9-month period, classifying the results depending on observation height. Note that Table 5.4 does not differentiate $\Re$ cases because the transfer functions only apply to the velocity modulus. Looking at Table 5.3, ME values show a similar pattern for all heights, *i.e.* as $\Re$ increases the downscaling tends to overestimate the wind velocity. In addition, the RMSE and the SS% show a worsening of the downscaled wind velocity as $\Re$ increases. The worst value of SS% (more negative) is obtained for $\Re_{1000}$, whereas the $\Re_{150}$ and the $\Re_{250}$ cases show similar performance than WRF. Contrasting to these results, Table 5.4 shows that the downscaled wind direction slightly improves with respect to WRF (positive SS%).

Table 5.3
Mean Error (ME), Root Mean Square Error (RMSE) (in m s^{-1}) and Skill Score (SS%) for wind velocity at 11 masts during the 9-month validation period depending on the data acquisition heights (40, 60, and 80 m). Downscaling results with different radii of influence $\Re$ for the transfer functions are shown. WRF model is used as reference model in the SS% calculations.

		40 m			**60 m**			**80 m**	
	ME	**RMSE**	**SS%**	**ME**	**RMSE**	**SS%**	**ME**	**RMSE**	**SS%**
$\Re_{150}$	-0.5	3.3	-0.7	-0.2	3.1	-0.8	-0.2	3.3	-0.8
$\Re_{250}$	-0.2	3.3	-2.2	0.0	3.2	-2.6	0.0	3.3	-2.7
$\Re_{500}$	1.1	3.8	-32.0	0.8	3.4	-19.7	0.7	3.6	-18.3
$\Re_{1000}$	2.6	4.8	-116.6	1.9	4.1	-75.2	1.7	4.2	-58,3

Table 5.5 desegregates the $\Re_{250}$ case for the 9-month validation period distinguishing three different stability classes (Section 5.3.6) and three different velocity bins of 4 m s^{-1} $\leq \boldsymbol{u}_{obs} <$ 8 m s^{-1}, 8 m s^{-1}$\leq \boldsymbol{u}_{obs} <$ 12 m s^{-1} and $\boldsymbol{u}_{obs} \geq$ 12 m s^{-1}. As observed, the downscaling skill scores improve as the velocity increases and outperform those of WRF at high velocities. The downscaling also

Table 5.4
Downscaling Root Mean Square Error (RMSE) and Skill Score (SS%) for wind direction (in °) at 11 masts during the 9-month validation period depending on the data acquisition heights (40, 60, and 80 m). WRF model is used as reference model in the SS% calculations.

40 m		**60 m**		**80 m**	
RMSE	**SS%**	**RMSE**	**SS%**	**RMSE**	**SS%**
15.5	11.0	16.5	6.9	16.9	6.8

Table 5.5
Downscaling Mean Error (ME), Root Mean Square Error (RMSE) and Skill Score (SS%) for wind velocity (m s^{-1}) and direction (°) during the 9-month period. Results are classified in wind velocity and atmospheric stability bins. WRF model is used as reference model in the SS% calculations.

	Velocity			**Direction**	
Velocity bin	**ME**	**RMSE**	**SS%**	**RMSE**	**SS%**
$4 < vel < 8$	1.3	3.3	-11.1	19.5	5.2
$8 < vel < 12$	-0.4	3.0	-2.6	14.6	9.6
$vel > 12$	-2.6	3.8	10.6	11.2	19.7
Stability bin	**ME**	**RMSE**	**SS%**	**RMSE**	**SS%**
Stable	-2.9	4.1	4.7	18.7	7.4
Neutral	-0.3	2.7	2.3	15.3	10.0
Unstable	1.0	3.2	-8.6	15.8	7.6

improves WRF results (positive SS%) in near-neutral and stable stability regimes, where buoyancy forces and vertical convective effects are supposed residual. These results are directly related to the fact that the pre-computed Alya-CFDWind fields have been obtained assuming neutral stability. Regarding wind direction, Table 5.5 also shows that the downscaling results outperform those of WRF for all velocity bins and stability classes. To complement these results, Figure 5.11 shows the velocity error difference for all pairs forecast-observation in the 9-month validation period depending on stability and wind velocity (using pairs of data with observed velocities greater than 8 m s^{-1}). Red dots in this figure mean that the downscaling improves the WRF forecast, whereas blue dots indicate the opposite. As observed, error differences at the measuring sites (11 masts) range between -1.2 and 1.2 m s^{-1}. The plot clearly reveals two well-defined regions, a blue-dominated zone (WRF is better than the downscaled field) and a red-dominated zone (downscaled field is better than WRF). Blue-dominated zone expands over the region with lower velocities and within the unstable regime, where buoyancy forces dominate. Conversely, the red-dominated zone covers the region with higher velocities and within near-neutral and stable regimes.

5.5 Introduction of diurnal cycle simulations and stability classes

This Section includes atmospheric stability in the microscale Alya-CFDWind pre-computed runs, *i.e.* considering a diurnal cycle for each geostrophic reference direction rather than a steady-state

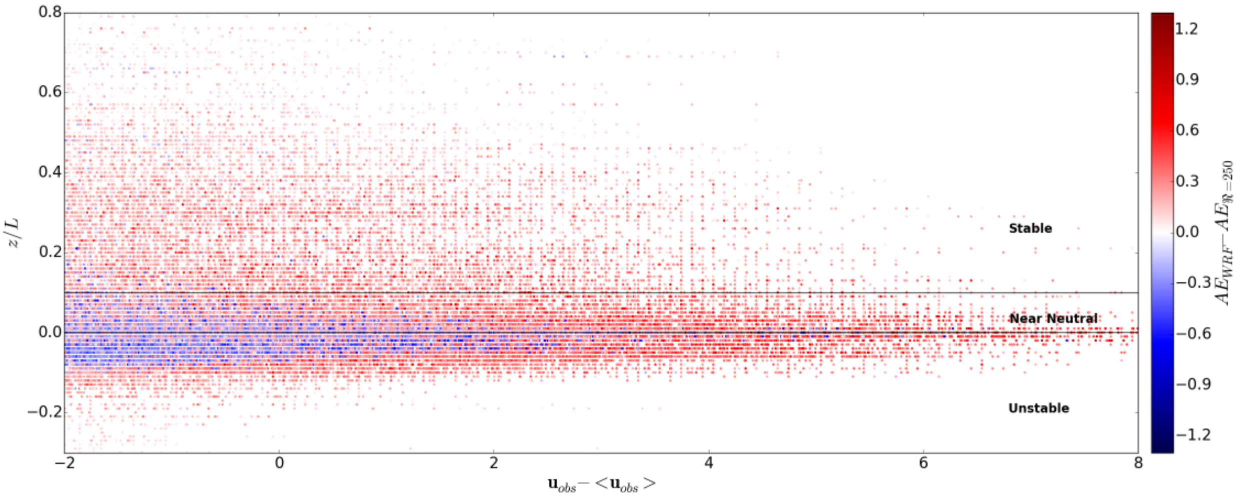

Figure 5.11
Scattered differences of absolute error $AE_{WRF} - AE_{\Re=250}$ *(in m s*$^{-1}$*) for all pairs forecast-observation in the 9-month period where the observed velocities exceeded 8 m s*$^{-1}$*. Positive values (red points) indicate the downscaling results improve WRF whereas negative values (blue points) indicate the opposite. Results depending on the stability class (z/L) and observed wind velocity (expressed as the difference with respect to the mean value of observations* $\boldsymbol{u}_{obs} - < \boldsymbol{u}_{obs} >$ *in m s*$^{-1}$*).*

neutral solution. The complete methodology to obtain these pre-computed diurnal cycles has been extensively introduced in Chapter 4. Here, we use the Alya-CFDWind diurnal cycle simulations used in the same Chapter 4[1], and apply the discretisation technique presented in Section 4.3.3, where 4 thermal stability regimes are considered; stable, stable-to-unstable transition, unstable, and unstable-to-stable transition. As done in Section 4.4.2, the ABL stability of WRF outputs is determined using the ground heat fluxes, the surface heat fluxes and vertical profiles of θ at the area of interest.

Table 5.6
Downscaling ($\Re_{500}$*) Root Mean Square Error (RMSE) and Skill Score (SS%) for wind velocity (m s*$^{-1}$*) and direction (°) during the 9-month period. Results are classified in wind velocity and atmospheric stability bins. The downscaling results using Alya-CFDWind steady-state simulations are used as reference model in the SS% calculations.*

	Velocity			Direction	
Velocity bin	**ME**	**RMSE**	**SS%**	**RMSE**	**SS%**
$4 < vel < 8$	1.8	3.7	6.2	19.3	2.7
$8 < vel < 12$	0.3	3.2	4.8	14.0	6.1
$vel > 12$	-1.7	3.3	0.6	11.0	2.0
Stability bin	**ME**	**RMSE**	**SS%**	**RMSE**	**SS%**
Stable	-1.1	3.3	0.0	16.2	8.1
Stable – Unstable	0.8	3.6	5.3	17.3	-6.0
Unstable	2.2	3.7	10.0	15.9	1.2
Unstable – Stable	1.5	3.3	5.8	15.5	1.3

Table 5.6 shows the validation of the downscaling results for $\Re_{500}$, this time using the 4 ther-

---

[1] an inner region of interest of 6.4×13 km^2 and a horizontal grid resolution of δx=δy=100 m

mal stability regimes considered. The downscaling results with the pre-computed Alya-CFDWind steady-state neutral simulations are now used as the model of reference to calculate the SS%, *i.e.* to quantify the improvement when introducing thermal coupling (positive SS%). For consistency, these simulations and the corresponding downscaling, have been re-run using the same mesh used for the diurnal cycle. As observed in Table 5.6, the downscaling skill scores improve when considering diurnal cycle simulations. Wind velocity results in unstable regime clearly improve as well as at lower velocity regimes. The worst SS% is obtained for wind direction in stable-to-unstable transition.

5.6 Summary and discussions

A novel mesoscale-to-microscale downscaling methodology to forecast near-surface high-resolution winds has been presented. The methodology combines a domain segmentation technique to preserve the mesoscale pattern with the use of transfer functions to incorporate the unresolved mesoscale model sub-grid terrain forcing effects (topographic effects). The downscaled near-surface wind field is obtained at 2D terrain following planes by merging segment-wise solutions obtained from pre-computed Alya-CFDWind reference simulations. Because of the blending process, a certain mass unbalance may occur even if each segment solution verifies the continuity equation. However, we have estimated that this unbalance resulting from blending is, at most, of the order of $\nabla \cdot u_{down} < 10^{-3}$ s^{-1} at all points.

The downscaling methodology has been validated against experimental data from a network of masts deployed at elevated zones within a complex terrain site at Puebla, Mexico. Unfortunately, the dataset did not allow us to quantify the gain at points where more pronounced microscale effects can be expected (*e.g.* valleys and channelling zones). Downscaled near-surface wind fields incorporate terrain forcing speed-up effects at the top of the ridges while, in contrast, winds slow-down and rotate at valleys and channeling zones. For the 9-month validation period, the downscaling methodology slightly improved the WRF model forecasts at masts in stable and near-neutral atmospheric regimes and for high wind velocities. In contrast, downscaling results did not show improvement during unstable regimes and during low wind velocities, where thermal effects prevail. This can be explained by the assumption of neutral stability in the pre-computed microscale fields and evidences the need to incorporate the diurnal cycle thermal effects into the Alya-CFDWind simulations. However, once the diurnal cycle simulations have been added as the pre-computed runs, downscaling results improved in those velocity and stability regimes where previous SS% were worse. Nonetheless, the stable-to-unstable transition, which coincides with the early development of the convective ABL, is still poorly characterised. This reveals a clear limitation of the methodology.

In terms of operational wind forecasting, a major advantage of the methodology is that it incorporates physical aspects of CFD models (not captured by simpler mass-consistent models) without adding substantial computational cost. For example, running the downscaling for a 48 h forecast window (30 min outputs) considering 5 planes of 13×8 km^2 at 40 m resolution with $\Re$=250 m takes only around 3 min on a standard laptop PC. The computing time depends on the value of $\Re$ (larger values of $\Re$ require more computing time because of the spatial average) but, in any case, this supposes a small percentage of the mesoscale model forecast computing time. Furthermore, these downscaling computing times could be drastically reduced by parallelising the downscaling code.

CHAPTER 6

Application to Microscale Atmospheric dispersion case

This chapter is an elaboration of the material in

Folch, A., **Barcons, J.**, Kozono, T., Ntchantcho, R., Costa., A., 2017. High-resolution modeling of atmospheric dense gas dispersion using TWODEE-2.1. Application to the 1986 Lake Nyos event. Natural Hazards and Earth System Sciences. 17, 6, 861-879; doi:10.5194/nhess-17-861-2017

where Sections 6.2, 6.3 and 6.7 are introduced here to put the reader in context, and for readability purposes. The contribution of this thesis are Sections 6.4, 6.5 and 6.6.

6.1 Introduction

Atmospheric dispersal of a gas denser than air can threat the environment and surrounding communities if the terrain and meteorological conditions favour its accumulation in topographic depressions, thereby reaching toxic concentration levels. Numerical modelling of atmospheric gas dispersion constitutes a useful tool for gas hazard assessment studies, essential for planning risk mitigation actions. In complex terrains, microscale winds and local orographic features can have a strong influence on the gas cloud behaviour, potentially leading to inaccurate results if not captured by coarser-scale modelling. We apply the methodology introduced in Chapter 5 (Section 5.2) to obtain time-dependent high-resolution microscale wind field to be used as input to a shallow-layer gas dispersal model (TWODEE-2.1). The goal is to simulate the time evolution of CO_2 gas concentration at different heights above the terrain. The strategy is applied to review simulations of the 1986 Lake Nyos event in Cameroon, where a huge CO_2 cloud was released by a limnic eruption. The gas cloud was spread downslopes from the lake suffocating thousands of people and animals across the Nyos and adjacent secondary valleys. The comparison with previous simulations that assumed coarser-scale steady winds and topography illustrates the importance of high-resolution wind modelling in complex terrains. This chapter reproduces the work presented in Folch et al. [2017], where Sections 6.2, 6.3 and 6.7 are introduced here to put the reader in context, and for readability purposes. The contribution of this thesis are Sections 6.4, 6.5 and 6.6.

6.2 The TWODEE dense gas dispersal model

TWODEE-2.1 [Hankin, Britter, 1999; Costa et al., 2008; Folch et al., 2009] is a FORTRAN90 code for the atmospheric dispersal of dense gases based on the shallow layer approach. The code is prepared to read steady or time-dependent wind fields for their interpolation to the computational mesh. Under the assumption that $h/L << 1$ (being h the gas cloud depth and L a characteristic length), the 2D shallow layer approach allows a compromise between more realistic but computationally demanding 3D dispersal and simpler 1D integral models. The TWODEE family models build on the depth averaged equations for a gas cloud resulting from mixing a gas of density ρ_g with an ambient fluid (air) of density ρ_a ($\rho_g > \rho_a$). The integration of volume, mass, and momentum balance equations over the mixed cloud depth from the ground to the top of the cloud yields to [e.g. Hankin, Britter, 1999]:

$$\frac{\partial h}{\partial t} + \nabla \cdot (h\overline{\boldsymbol{u}}) = u_e + u_s \tag{6.1}$$

$$\frac{\partial \left(h(\overline{\rho} - \rho_a)\right)}{\partial t} + \nabla \cdot \left(h\left(\overline{\rho} - \rho_a\right)\overline{\boldsymbol{u}}\right) = \rho_a u_e + \rho_g u_s \tag{6.2}$$

$$\begin{aligned} \frac{\partial\left(h\overline{\rho}\,\overline{\boldsymbol{u}}\right)}{\partial t} + \nabla\cdot\left(h\overline{\rho}\,\overline{\boldsymbol{u}}\otimes\overline{\boldsymbol{u}}\right) + \frac{1}{2}S_1\nabla\left(g(\overline{\rho}-\rho_a)h^2\right) + \\ S_1 g(\overline{\rho}-\rho_a)h\nabla e + \frac{1}{2}\overline{\rho}C_D|\overline{\boldsymbol{u}}|\overline{\boldsymbol{u}} + \\ \boldsymbol{F} + \kappa\rho_a\left(\frac{\partial}{\partial t} + v_a\frac{\partial}{\partial x} + w_a\frac{\partial}{\partial y}\right)\cdot\left(h(\overline{\boldsymbol{u}}-\boldsymbol{u}_a)\right) = \rho_a u_e \boldsymbol{u}_a \end{aligned} \tag{6.3}$$

where h is the cloud depth (defined as the height below which 95% of the buoyancy is located), $\overline{\rho}$ is the depth averaged cloud density, $\overline{\boldsymbol{u}} = (\overline{u}_x, \overline{u}_y)$ is the depth averaged cloud velocity, $\boldsymbol{u}_a = (v_a, w_a)$ is the ambient fluid (air) velocity vector (here obtained by downscaling), u_e is the ambient fluid entrainment velocity modulus, u_s is the gas inflow velocity modulus (source term), $e = e(x, y)$ is the terrain elevation, C_D is a drag coefficient, $\boldsymbol{F}$ is the turbulent shear stress force (per unit area), and $S_1 \approx 0.5$ and κ are semi-empirical parameters. The terms in the momentum equation (6.3) include the local time derivative, the convective term, the pressure gradient (assumed hydrostatic although the density profile can be non-uniform), the effect of terrain slope, the surface shear stress (depending on the terrain roughness and characterised by the drag coefficient), the force per unit area exerted by turbulent shear stress and, finally, the leading edge terms that account for interaction among dense and ambient fluids. Given closure equations for the drag coefficient C_D, shear stress force $\boldsymbol{F}$ and entrainment velocity u_e [Hankin, Britter, 1999; Folch et al., 2009], the set of equations above can be resolved numerically to obtain cloud height and vertically averaged density and velocity depending on terrain, source term (definition of u_s) and ambient fluid velocity (wind field). Although TWODEE is a shallow water model, it can also estimate the vertical density profile from the depth averaged density $\overline{\rho}$ assuming an empirical exponential decay [Hankin, Britter, 1999]:

$$\rho(z) = \rho_a + \tfrac{2}{S_1}(\overline{\rho}-\rho_a)\exp\left(-\tfrac{2}{S_1}\tfrac{z}{h}\right) \quad 0 \le z \le h \tag{6.4}$$

from which the vertical concentration profile $c(z)$ (expressed in ppm) and the dosage $Do(t, z)$ during a time interval $(0, t)$ can be computed as:

$$c(z) = c_b + (10^6 - c_b)\frac{\rho(z)-\rho_a}{\rho_g-\rho_a} \tag{6.5}$$

$$Do(t, z) = \int_0^t \left[c(z)\right]^n dt \tag{6.6}$$

where c_b is the background concentration (in ppm) and n is the so-called toxicity exponent.

6.2.1 Impact assessment for dense CO$_2$ gas dispersal

According to the Occupational Safety and Health Administration (OSHA), the CO_2 Long Term Exposure LIMIT (LTEL) is set at air concentrations of 0.5% (5,000 ppm) for exposures up to 8-

hours per day, whereas the Short Term Exposure LIMIT (STEL) is set at air concentrations of 3% (30,000 ppm) for exposures up to 15 minutes. However, at higher concentrations/dosage, CO_2 causes several adverse health effects when inhaled. Experience shows that CO_2 air concentrations of around 5% (50,000 ppm) produce heavy breathing, sweating, quicker pulse, weak narcotic effects and headache. Under these concentrations, the exposure time to avoid the development of adverse health symptoms is of few minutes only. For example, a 30-minute exposure to 5% concentration (50,000 ppm) produces intoxication manifested as headaches, dizziness, restlessness, breathlessness, increased heart rate and blood pressure, and visual distortion. At around 10% concentration (100,000 ppm) humans are affected by respiratory distress, impaired hearing, nausea, vomiting, and loss of consciousness in 10 min only. Finally CO_2 air concentrations >15% (150,000 ppm) are considered lethal causing coma, convulsions, and rapid death. The U.K. Health and Safety Executive (HSE; www.hse.gov.uk) developed an assessment of dangerous toxic substances, including CO_2, defining the Specified Level Of Toxicity (SLOT) and the Significant Likelihood Of Death (SLOD) depending on concentration and duration of exposure [Harper, 2011]. Considering these values [Harper, 2011], we assume a cumulative normal distribution for the percentage of human fatalities:

$$P(c,d) = \frac{1}{2}\left[1 + \mathrm{erf}\left(\frac{c-\mu}{\sqrt{2}\sigma}\right)\right] \tag{6.7}$$

$$\mu = a_0 + \frac{b_0}{(1 + d^{c_0})} \tag{6.8}$$

$$\sigma = a_1 + \frac{b_1}{(1 + d^{c_1})} \tag{6.9}$$

where P is the probability of death, c is the CO_2 concentration (expressed in %), d is the exposure duration (expressed in minutes), and a_i and b_i are empirical constants. After calibration of equation (6.7) with the HSE tabulated values (assuming SLOT at 3%), we obtained the following values for the constants: $a_0 = 5.056$, $b_0 = 17.885$, $c_0 = 0.357$, $a_1 = 0.662$, $b_1 = 2.421$, and $c_1 = 0.354$. Results are shown in Figure 6.1, plotting the percentage of fatalities (probability of death in %) as function of CO_2 concentration for different exposure durations. An impact criterion based on these empirical curves was added in TWODEE-2.1 to compute, at each point of the computational domain, the predicted percentage of fatalities at user-defined heights.

6.3 The 1986 Lake Nyos limnic eruption

Lake Nyos (Fig. 6.2) is one of the ∼40 volcanic lakes scattered along the 1600 km-long Cameroon Volcanic Line [e.g. Lockwood, Rubin, 1989]. This lake became famous worldwide on Thursday 21 August 1986 after the occurrence of the most tragic limnic eruption ever registered. During few

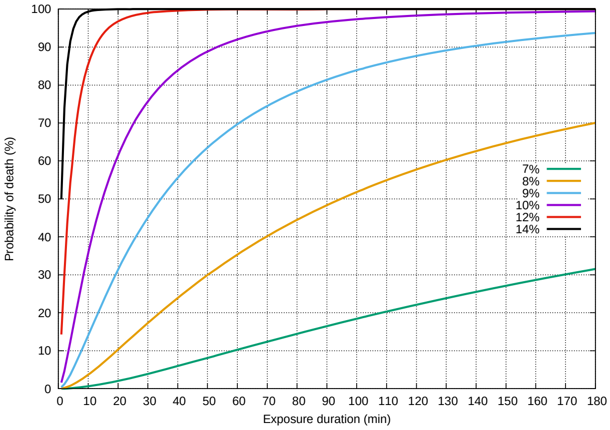

Figure 6.1
Percentage of fatalities (probability of death in %) depending on exposure duration (in min) according to eq. (6.7). Values are shown for different values of CO_2 *concentration ranging from 7% to 14% vol.*

(<5) hours, a huge (0.1-1 km^3) CO_2 gas cloud [Tuttle et al., 1987; Kanari, 1989; Evans et al., 1994] released during the lake Nyos overturning spread downslopes from the lake (1100 m a.s.l.) filling up the underlying Nyos valley and suffocating around 1700 people and 3000 cattle [e.g. Kling et al., 1986]. Evidence from eyewitness reports indicated that the cloud directed primarily W-NW at around 21:00 LT (20:00 UTC) affecting the bottom valleys of Cha and Fang (see Fig. 6.3), but without causing reported deaths at the later location [Baxter, Kapila, 1989]. Following this initial dispersal phase, the gas cloud direction shifted towards NE, probably as a consequence of a sudden wind veer, filling up the Nyos valley down to the Subum village (∼10 km line of sight from the lake), where the largest number of casualties occurred. Deaths in humans and animals (including birds) occurred up to 20 km distance across the main and adjacent secondary valleys [Le Guern et al., 1992].

Le Guern et al. [1992] collected multiple testimonies of survivors that allowed the authors for reconstructing the history of the event, locating where casualties occurred, and constructing a map of the areas impacted by the disaster (see Table 6.1 and Fig.1 in Le Guern et al. [1992]). It should be stressed that the percentages of fatalities reported by Le Guern et al. [1992] resulted from posterior interviews by anthropologists and are subject to large uncertainties related to translation and interpretation, approximate location of sites, and actual number of casualties. Notwithstanding these limitations, data inferred from eye-witnessing constitutes the only source of information available for indirect model validation given the lack of any wind or gas concentration measurement at Nyos on that time. At present, the level of risk at lakes Nyos and Monoun has decreased notably after the successful deployment of degassing pipes started in March 2001 and February 2003, respectively. The progressive gas removal resulted in considerable deepening of the level of gas-rich water in a

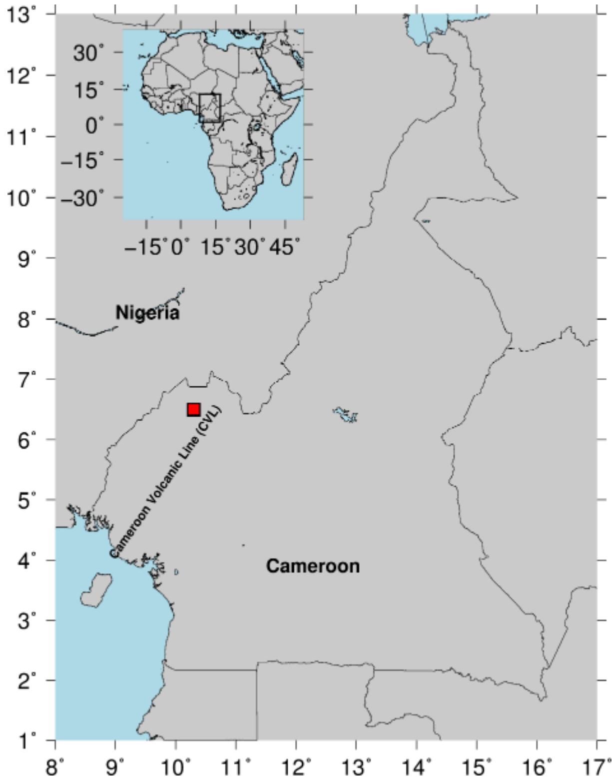

Figure 6.2
Map of Cameroon showing the lake Nyos area (red square).

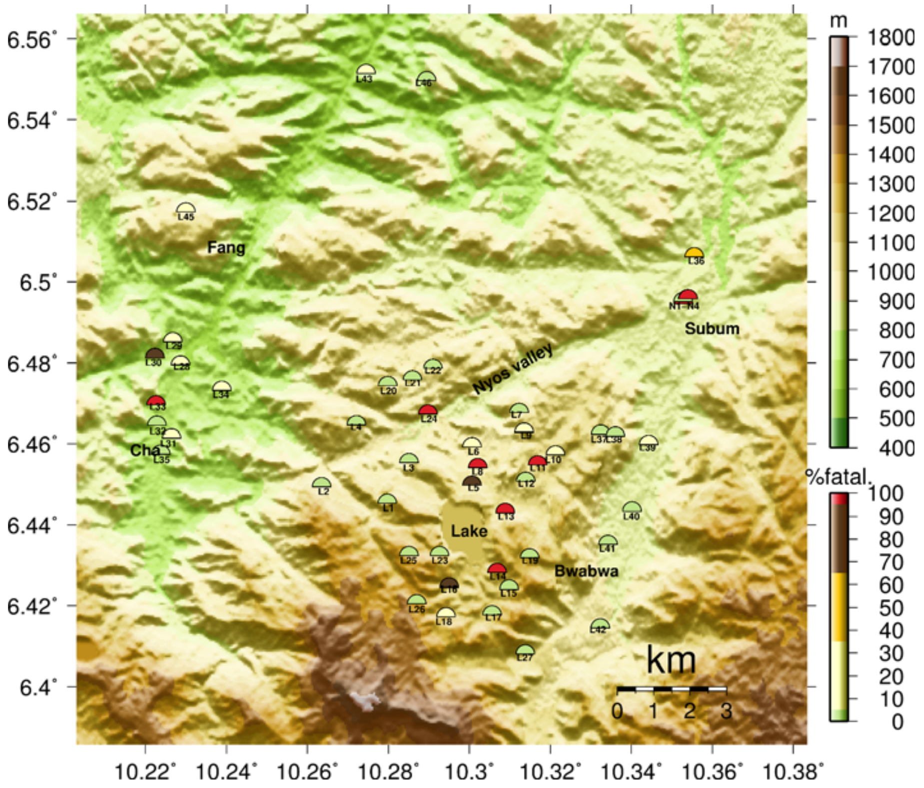

Figure 6.3
Topographic map of the area around Lake Nyos showing elevation contours (in m a.s.l.). The locations listed in Table 6.1 are shown by halved circles coloured according the percentage of fatalities (in %) reported by Le Guern et al. [1992].

Table 6.1
List of affected points with coordinates and percentage of observed fatalities. (x, y) coordinates are in UTM zone 32N (datum WGS84). Points starting with an L have been digitalised from Le Guern et al. [1992]; points starting with an N were obtained by the authors after interviewing survivors in situ. Comments as reported by Le Guern et al. [1992] in their Table 1.

Point	x (m)	y (m)	lon (°)	lat (°)	Fatalities(%)	Comments
L1	641523	712595	10.280	6.445	0	
L2	639726	713051	10.264	6.449	0	
L3	642113	713722	10.285	6.455	0	
L4	640665	714741	10.272	6.465	0	
L5	643829	713105	10.301	6.450	90	
L6	643829	714151	10.301	6.459	20	
L7	645116	715089	10.312	6.468	0	
L8	643989	713588	10.302	6.454	100	
L9	645250	714553	10.314	6.463	15	
L10	646108	713936	10.321	6.457	15	
L11	645625	713668	10.317	6.455	100	
L12	645303	713212	10.314	6.451	0	
L13	644740	712354	10.309	6.443	100	
L14	644526	710719	10.307	6.428	100	A man ran uphill, survived, all cows died
L15	644847	710263	10.310	6.424	0	
L16	643212	710316	10.295	6.425	80	Nobody at the compound, 50 cows died, 15 survived
L17	644392	709566	10.306	6.418	0	
L18	643131	709512	10.294	6.417	25	
L19	645411	711121	10.315	6.432	0	
L20	641523	715813	10.280	6.474	0	
L21	642193	715974	10.286	6.476	0	
L22	642756	716296	10.291	6.479	0	
L23	642944	711174	10.293	6.432	0	
L24	642622	715035	10.290	6.467	99	Nyos village: 6 lived, 600 died
L25	642113	711174	10.285	6.432	0	Upper Nyos; 150 survived, 0 died
L26	642327	709861	10.287	6.420	0	
L27	645303	708493	10.314	6.408	0	Several compounds, 40 survived, 0 died
L28	635865	716376	10.229	6.480	20	12 people survived
L29	635651	716993	10.227	6.485	30	
L30	635168	716564	10.222	6.481	65	
L31	635624	714365	10.226	6.461	25	3 people lived
L32	635222	714714	10.223	6.464	0	
L33	635195	715277	10.223	6.470	100	15 people died
L34	636991	715679	10.239	6.473	30	Cha village: 130 survived, 58 died
L35	635329	713936	10.224	6.457	0	
L36	649888	719352	10.356	6.506	50	Subum village: 400 lived, 400 died
L37	647341	714499	10.332	6.462	0	
L38	647743	714446	10.336	6.462	0	
L39	648655	714231	10.344	6.460	20	
L40	648199	712408	10.340	6.443	0	
L41	647556	711496	10.334	6.435	0	Mgombe: 160 lived
L42	647341	709217	10.332	6.415	0	Upper Mgombe: 150 lived
L43	640906	724340	10.274	6.551	10	
L44	642622	731794	10.290	6.619	5	
L45	635999	720559	10.230	6.517	0	
L46	642568	724152	10.289	6.550	0	
L47	638305	727235	10.251	6.578	0	
L48	641549	728844	10.280	6.592	0	
L49	640557	729756	10.271	6.600	0	
N1	649581	718074	10.353	6.495	100	
N2	649581	718136	10.353	6.495	0	
N3	649713	718210	10.354	6.496	50	
N4	649719	718210	10.354	6.496	100	

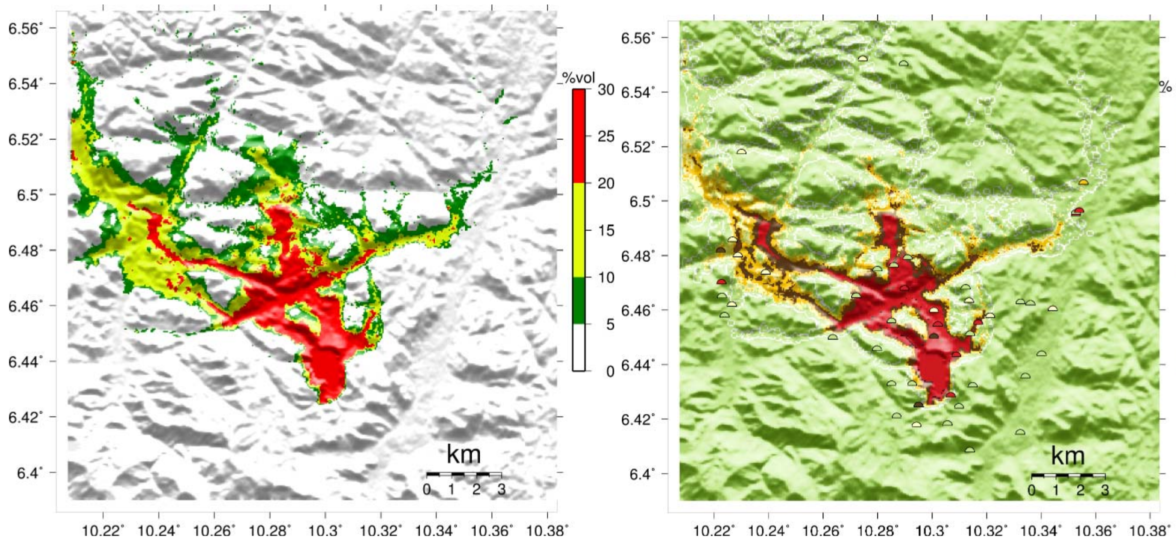

Figure 6.4
Previous modelling results from Costa, Chiodini [2015] scenario-II (4 h of gas emission assuming a constant mass flux of 1.4×10^5 $kgm^{-2}d^{-1}$ *from a diffuse source of* 235×235 m^2*). Left: maximum* CO_2 *concentration (%vol.) achieved at 1 m height. Right: percentage of fatalities (in %) predicted by the model applying eq. (6.7) at 1 m height. Halved circles show the actual reported percentages at locations using the same color scale.*

short period of time [Kling et al., 2005; Kusakabe et al., 2008]. However, there is still the recognised need to perform a quantitative CO_2 hazard assessment for several reasons, including the possibility of future gas build-up or a breakthrough of the dam build at the northern shore of the lake. Thus, for example, Aka, Yokoyama [2013] estimated that dam break could cause a sudden drop in lake level by 40 m, followed by decompression and inevitably a new gas burst.

6.3.1 Previous modelling results

Costa, Chiodini [2015] have recently used the TWODEE-2.0 model to simulate four different scenarios (released gas mass ranging from 0.29 to 1.95 Tg, wrongly reported in their table as Gg) using a 90m resolution DEM. Surface wind data resulted from applying the DWM mass-consistent pre-processor to a constant wind profile extracted from the closest point of the NCEP/NCAR Reanalysis-1 [Kalnay et al., 1996]. As a result of this limitation, none of their simulations was able to capture properly the cloud dispersion pattern, strongly influenced by a sudden wind veering. Figure 6.4 shows, for illustrative purposes, results for their scenario-II, the one that better reproduced the observations (see Fig.5 in Costa, Chiodini [2015] for other scenario results). In the following sections, these previous simulations are revisited considering a higher DEM accuracy (30 m instead of 90 m; from ASTER G-DEM, a product of METI and NASA) and high-resolution transient microscale surface winds derived from downscaling the WRF-ARW mesoscale winds with the ALYA-CFDWind model.

6.4 WRF-ARW simulations

WRF-ARW model configuration is summarised in Table 6.2. For the Nyos application, the WRF-ARW simulation starts on Thursday 21 August 1986 at 00:00 UTC lasting 48 h (around 18 h are allowed for model spin-up). Initial and 4-times daily boundary conditions driving WRF come from the NCEP/DOE Reanalysis 2. Figure 6.5 shows the five domains used, consisting of 1 parent grid at 81 km horizontal resolution, covering the African continent, and 4 nested domains at 27, 9, 3, and 1 km horizontal resolutions, all centred around Lake Nyos. The regional synoptic situation on Thursday 21 August 1986 is illustrated in Figure 6.6, showing WRF-ARW results for the first nest domain (27 km resolution) at different times. It can be observed how a low pressure (<800 hPa at 2000 m) region and its cyclonic circulation located NE of Cameroon coexists with strong winds both South and North and a region of weak winds over NW Cameroon at around 16:00 UTC (Fig. 6.6a). The simulations indicate that this situation lasted for about 6 hours until 22:00 UTC, when winds over Nyos became stronger and pointed SE. In contrast, near-surface winds followed a very different pattern (Figure 6.7) reflecting the topography-induced forcing at lower atmospheric levels. However, given the orographic complexity, the WRF-ARW results at 1 km resolution (inner nest) are still insufficient for driving high-resolution gas transport simulations, indicating the need for an ulterior downscaling.

Table 6.2
WRF-ARW model configuration used for the 1986 Lake Nyos simulations.

WRF-ARW configuration	
Model version	3.4.1
Initial and Lateral BC's	NCEP/DOE Reanalysis-2
Domains	1 parent + 4 nests
Horizontal resolutions	81 km (parent) and 27, 9, 3, and 1 km (nests)
Horizontal grid sizes	110×110 (parent) and 136×127, 121×133, 181×166, and 151×151 (nests)
Vertical levels	60 levels, with top at 70 hPa
Simulation length	48 h (spin-up of 24 h)
Time step	180 s (parent), ratios of 1/3 for nests
Parametrization	**Scheme**
Microphysics	WRF single-moment 6-class (WSM6) [Hong, Lim, 2006]
Cumulus	Modified Kain-Fritsch (disabled for 1 km nest) [Kain, 2004]
Surface Layer	MM5 Monin-Obukhov
Land Surface	Unified Noah Land Surface Model (LSM) [Chen, Dudhia, 2001]
Planet Boundary Layer	Mellor Yamada Janjic (MYJ) [Janjić, 1994]
Long-wave Radiation	Rapid Radiative Transfer Model (RRTM) [Mlawer et al., 1997]
Short-wave Radiation	Dudhia [Dudhia, 1989]

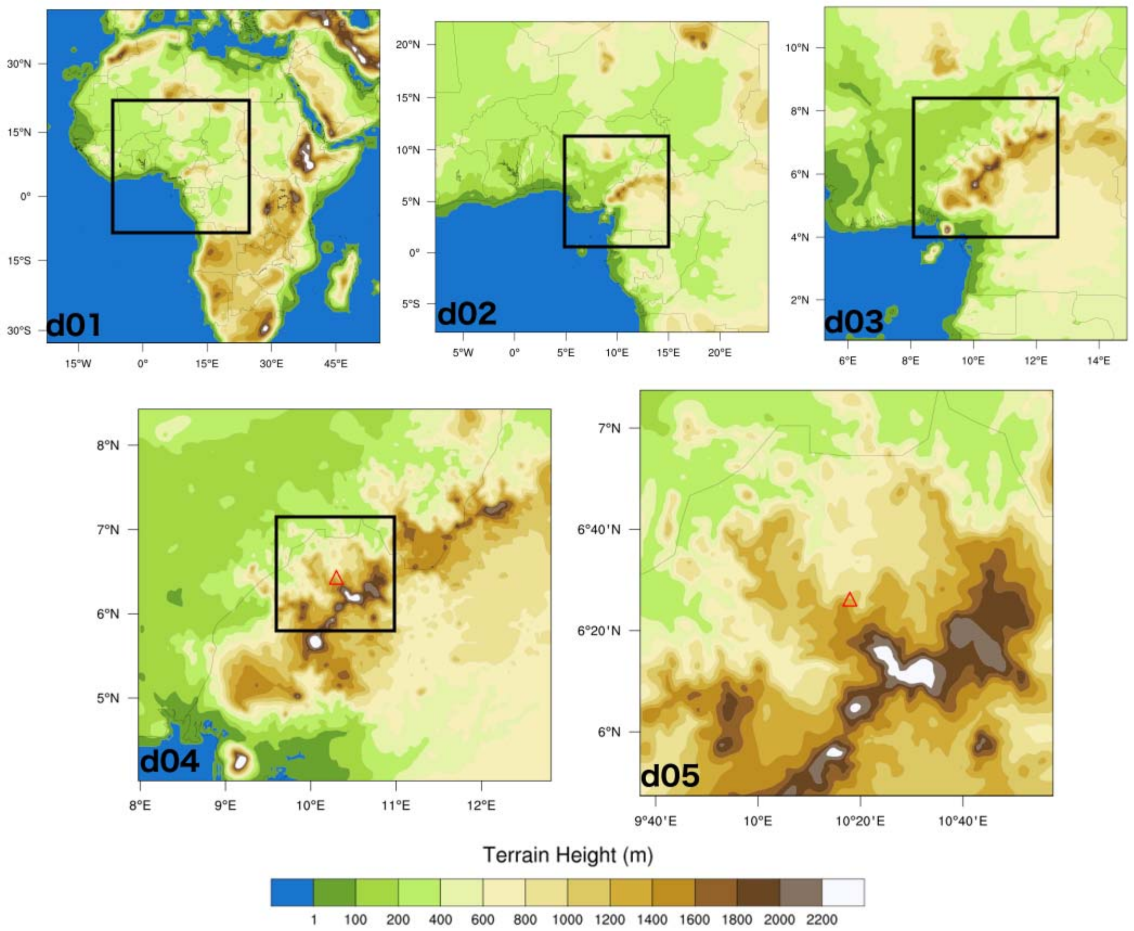

Figure 6.5
WRF-ARW domains for the Nyos run. The model configuration consists of one parent domain (d01) at 81 km horizontal resolution and 4 nests (d02 to d05) at 27, 9,3, and 1 km resolution centred at the Lake Nyos (red triangle, not on scale). Color contours indicate the WRF-ARW model topography at each resolution.

6.5 Alya-CFDWind simulations

For the Nyos case, the ALYA-CFDWind computational domain consists of an inner zone of 20×20 km^2 at 50 m horizontal resolution, a transition zone of 15 km and a flat buffer zone of 10 km to accommodate the flow. Along the vertical direction, the structured hexahedral grid extends up to 5 km above the terrain with 64 vertical layers growing geometrically in size from 0.5 m at surface to 250 m at the top of the computational domain. The resulting computational mesh (see Fig. 6.8) has a total number of grid points of about 30 million. The Coriolis force was set to that of a latitude of 6° N, and the maximum mixing length calculated depending on the wind at top as in Apsley, Castro [1997]. As boundary conditions, we prescribed the wind at top (geostrophic wind) to a reference value of 10 m s^{-1} considering different geostrophic wind directions (sectors) at 15° intervals. One

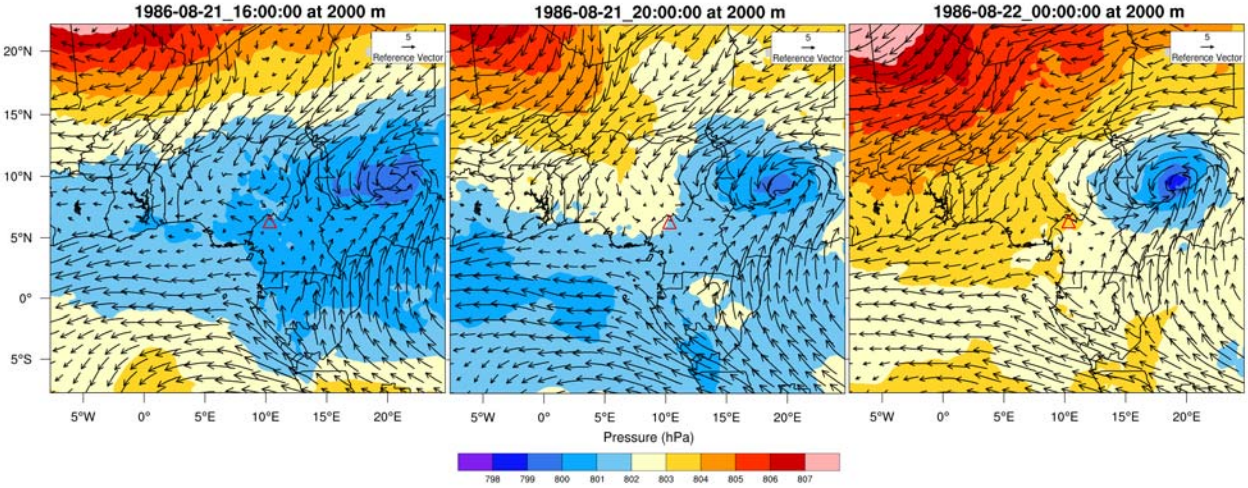

Figure 6.6
Synoptic meteorological situation according to the WRF-ARW simulation showing pressure contours (hPa) and wind vectors (m s^{-1}*) for domain d02 (first nest, 27 km resolution domain) at 2000 m height above sea level. Results for 21 Aug 1986 at 16:00 (left), 20:00 (center) and 24:00 (right) UTC. The red triangle shows the location of the Nyos lake. For clarity, only few model wind vectors are shown.*

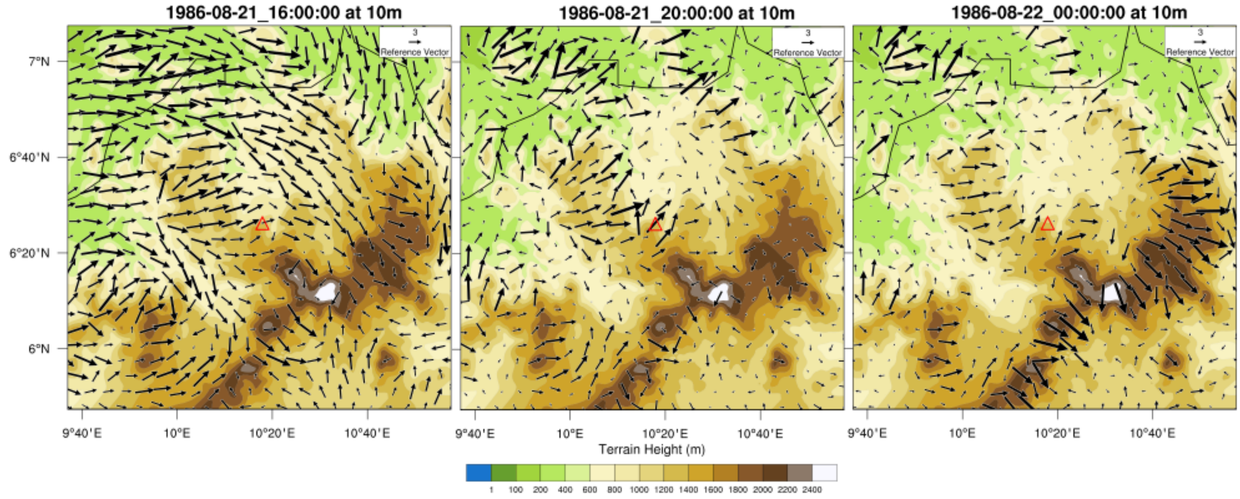

Figure 6.7
Local meteorological situation according to the WRF-ARW simulation showing terrain height contours (m a.s.l.) and wind vectors (m s^{-1}*) for domain d05 (last nest, 1 km resolution domain) at 10 m above the surface. Results for 21 Aug 1986 at 16:00 (left), 20:00 (center) and 24:00 (right) UTC. The red triangle shows the location of the Nyos lake. For clarity, only few model wind vectors are shown.*

ALYA-CFDWind simulation was performed for each reference direction of the geostrophic wind (*i.e.* 24 different runs are necessary to scan all possible geostrophic wind directions).

6.6 Downscaling results

Figure 6.9 compares the 3 km resolution WRF results at 10 m above the terrain with the downscaled field at the area of interest around the Lake Nyos. This Figure highlights the local information added by the microscale model over mountainous areas and valleys, where WRF shows a smoother

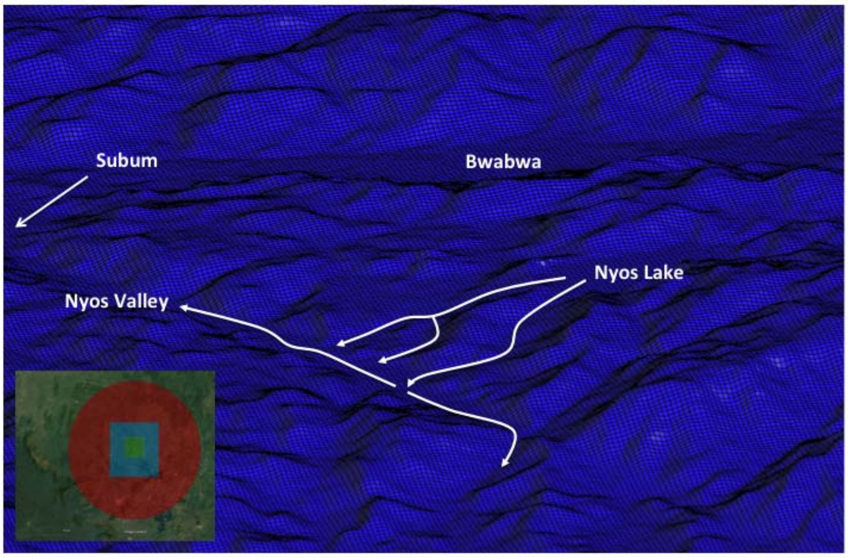

Figure 6.8
Detail of the ALYA-CFDWind computational mesh (50m horizontal resolution) around the Nyos lake. The bottom-left inset shows the extent of the computational domain composed of 3 differentiated zones, flat buffer (red), transition (pale blue), and inner domain (green) at 50 m resolution containing the detailed terrain information. The arrows indicate the approximate gas flow path according to observations.

behaviour. Unfortunately, no surface wind data existed at that time to validate these results. However, some consistence with reports exists. For example, a strong microscale wind rotation from NE to SW (wind origin direction) is clearly visible along the Nyos valley from 18:00 to 21:00 UTC, in agreement with cloud dispersal reports indicating two differentiated dispersal phases. In order to illustrate this phenomenon, Figure 6.10 plots time series of 10 m wind velocity and direction from 16:00 to 24:00 UTC at two locations of special interest, the lake itself and a point at the bottom of the Nyos valley (see Fig. 6.3).

Note how near surface wind direction changes sharply at both locations between 17:30 (wind from NE) and 19:30 (wind from SW) UTC. A systematic WRF model error phase of about 3 hours seems to exist because dispersal reports suggest such a strong wind veering occurring after 22:00 LT (21:00 UTC). In any case, these wind field variations strongly indicate the need for including time-dependent heterogeneous winds for the gas dispersal simulations. Finally, it is worth looking at the atmospheric stability during the time of the event since this parameter also favours the accumulation of dense gas at depressions. Figure 6.11 plots the static stability versus time, clearly reflecting a unstable to stable transition related to the diurnal cycle occurring at around 16:00 UTC.

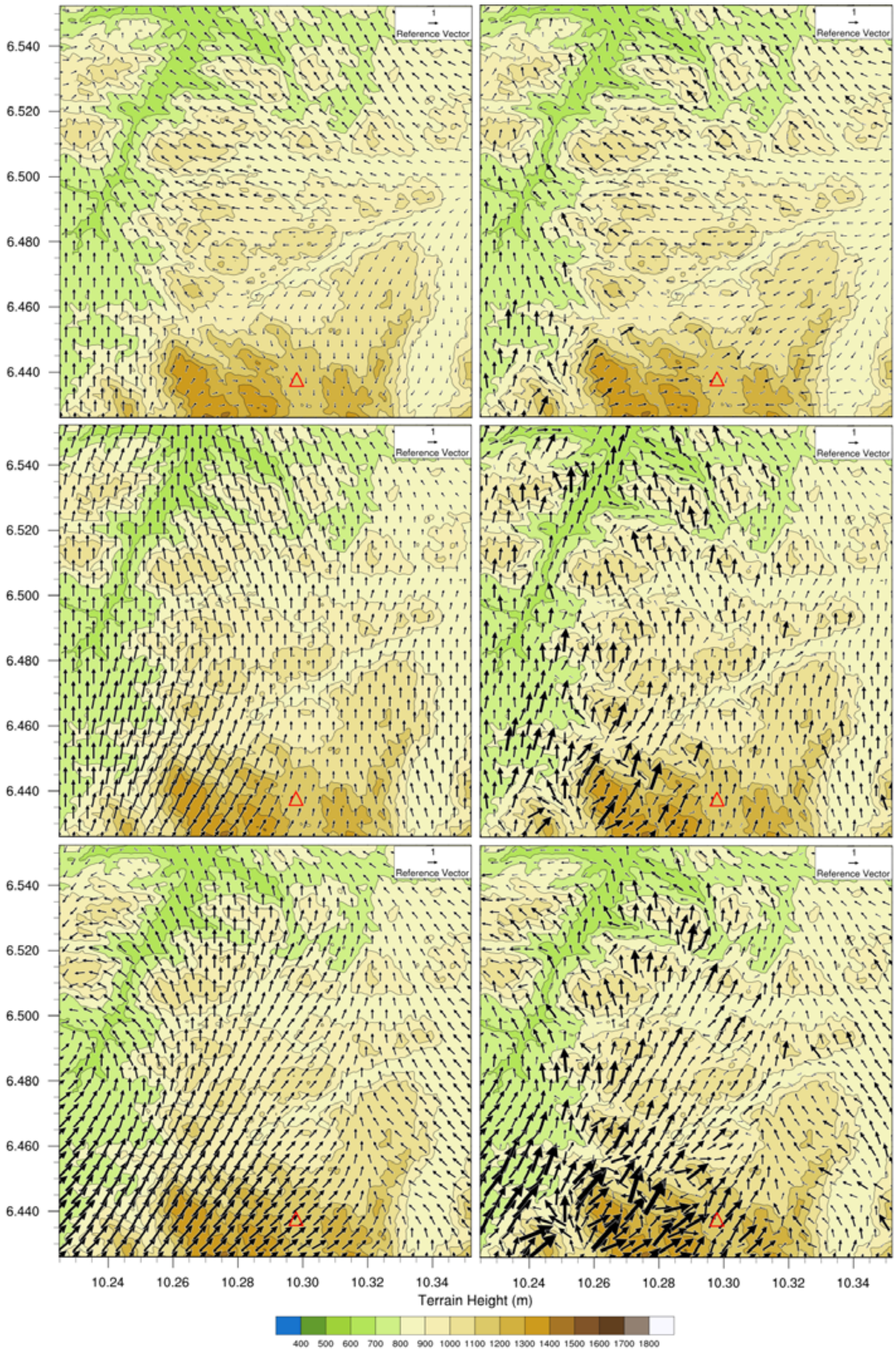

Figure 6.9
Wind vectors at 10 m above terrain as given by WRF-ARW at 3 km resolution (left column) and the downscaling (right column) for 21 Aug 1986 at 18:00 (top), 19:00 (middle) and 21:00 (bottom) UTC. For visualisation and point-to-point comparison purposes, WRF results have been interpolated to the CFD mesh and, when necessary, extrapolated below its lower level. The red triangle shows the location of the Lake Nyos.

6.7 High-resolution dispersal modelling results

Once the high-resolution winds have been obtained for the period and area of interest, 10 m wind values every 20 minutes (*i.e.* 3 times hourly) were given to the TWODEE-2.1 model together with the 30 m resolution DEM and the definition of the source term to simulate the CO_2 cloud dispersal.

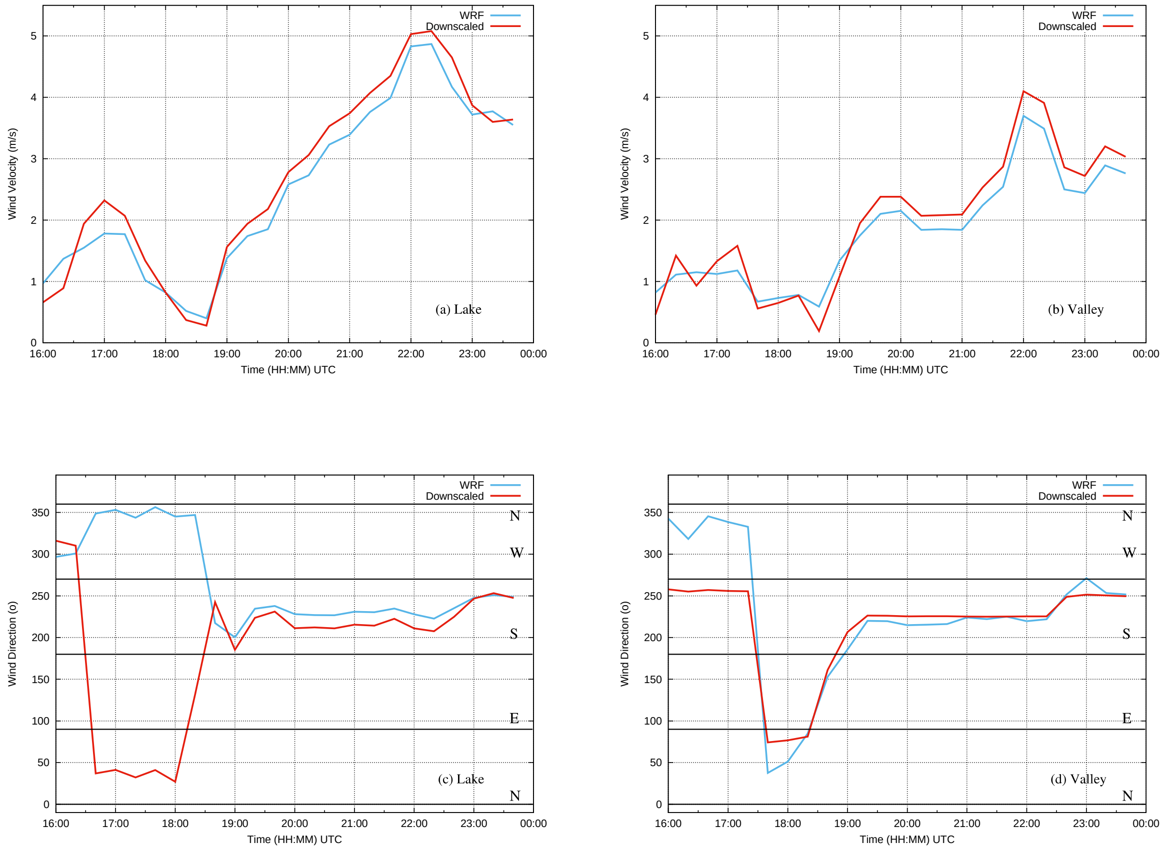

Figure 6.10
Time series of 10-m wind speed and direction at two points located at the Nyos lake (a,c) and at the bottom of the Nyos valley (b,d). Results from WRF simulations at 1 km resolution (blue lines) and downscaling using ALYA-CFDWind at 50 m (red lines). Wind direction criterion is that of the coming direction, i.e. 0° indicates wind coming from the N, 90° coming from the E, etc. Note the sudden short-lived wind veering from NE to SW starting at around 18:00 UTC.

Our simulations assume the eruption started at 17:30 UTC (18:30 LT), *i.e.* 2-3 h advanced with respect to eyewitness reports. This source term shift in the dispersal simulations was necessary because of the WRF model phase error discussed in Section 6.4. On the other hand, given the large uncertainties in the source term concerning eruption duration, intensity and evolution of CO_2 mass flow rate with time; we performed a source term characterisation considering different sets of simulations, each set with different source term characteristics. Results for all these simulations (a total of 62 source term scenarios) were validated on a point-by-point basis comparing the TWODEE-2.1 predicted probability of fatalities with the actual percentage of fatalities reported at 53 locations (Table 6.1). We also computed the total Mean Absolute Error (MAE) as:

$$MAE = \frac{1}{n_b} \sum_{i=1}^{n_b} (MAE)_i \tag{6.10}$$

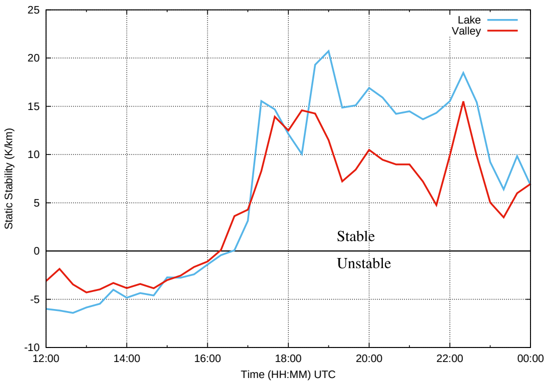

Figure 6.11
Static stability (gradient of potential temperature in $^{\circ}K\ km^{-1}$*) versus time at the same two points than in Fig. 6.10 (lake in blue and valley in red) according to WRF simulations at 1 km resolution. The potential temperature gradient has been computed using WRF* σ*-levels 1 and 6, at roughly 12 and 100 m above terrain, respectively. Positive values indicate stable atmosphere. Note the transition from unstable to stable stratification occurring after 16:00 UTC.*

with

$$(MAE)_i = \frac{1}{m}\sum_{j=1}^{m} |PO_j - PM_j| \tag{6.11}$$

where $(MAE)_i$ is the bin absolute error, m the number of observations (localities) in the $j-th$ bin, PO is the observed percentage of fatalities, and PM is the modelled probability at the same locality. We found that the higher-score simulations belong to a source with two phases; an initial phase with a constant CO_2 emission followed by a second phase with exponential source strength decay. This is a consistent result. Table 6.3 and Figure 6.12 summarise the characteristics of the source term for the highest ranked run. The total CO_2 emitted mass is 0.86 Tg, released during 3 h. This value is in good agreement with previous independent estimations, ranging from 0.29 Tg [Evans et al., 1994] to 1.95 Tg [Tuttle et al., 1987]. For comparison, the scenario-II in Costa, Chiodini [2015] (see Figure 6.4) gives a MAE of 36.6%, substantially higher even if the characteristics of the source term are similar to our best-fit runs both in terms of duration (4 h) and total mass (1.33 Tg). These differences can be explained because of the high-resolution time-dependent winds, which are able to capture the wind veering leading to the differentiated cloud dispersal branches (see Figure 6.12).

Table 6.3
Source term characteristics of the best fit simulation showing total CO_2 *emitted mass, mass flux variation,* χ^2*, and Mean Absolute Error (MAE) considering the 5-class binning criterion.*

Duration (hour)	**Total mass (Tg)**	**Mass flux (10^4 kg m^{-2}d^{-1})**	**MAE (%)**
3	0.86	4 for 30 min followed by a burst to 18 and 150 min exponential decay	34.7

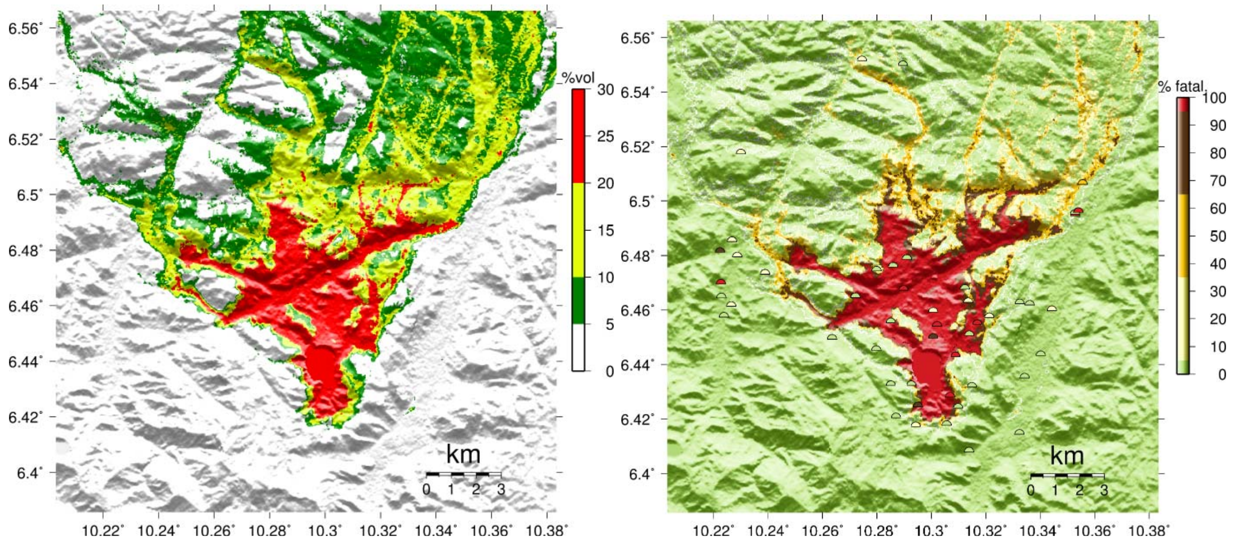

Figure 6.12
Best fit simulation results. Left: maximum CO_2 *concentration (%vol.) achieved at 1 m height. Right: percentage of fatalities (in %) predicted by the model applying eq. (6.7) at 1 m height. Halved circles show the actual reported percentages at locations using the same color scale.*

This can also be observed in Figure 6.13 by looking at the evolution of concentration with time

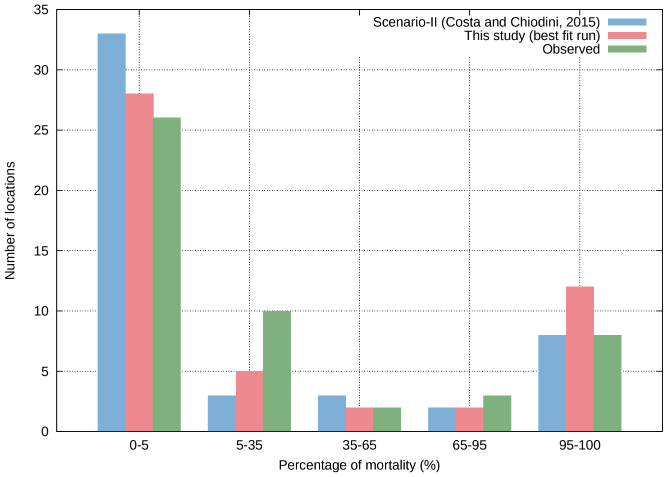

Figure 6.13
Histogram showing the fit between observations (green bars) and best-fit run (red bars) across the bins. Results from Costa, Chiodini [2015] are also shown for comparison (blue bars).

at different locations. As observed in Figure 6.14, the TWODEE-2.1 simulations can reproduce a first W-NW branch affecting the bottom valleys of Cha and Fang (location L34) followed by a gas cloud direction shift towards NE affecting the Subum village (location L36). According to simulations, this occurred around 2 hours after the eruption onset (*i.e.* 20:30 LT). Considering the 2-3 h shift necessary to correct the meteorological (WRF) phase error, this is in excellent agreement with eyewitness reports.

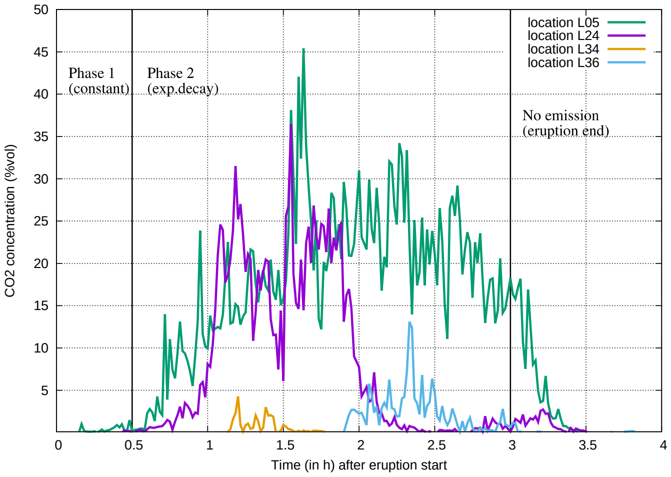

Figure 6.14
Evolution with time (in h) of CO_2 concentration (%vol.) at different locations for the best fit simulation. Results at 1 m height. Location L05 is near the Lake, L24 at the Nyos valley, L34 near Cha (W branch) and L36 near Subum (E branch). See Figure 6.3 for details.

6.8 Summary and discussions

This chapter has presented a real application of the downscaling methodology, presented in Chapter 5, at Lake Nyos atmospheric gas dispersal scenario in 1986. The downscaling has been used to assist the reconstruction of the event by the TWODEE-2.1 model. The results have shown better agreement compared with previous simulations that used a mass-consistent constant wind field extracted from the closest point of the NCEP/NCAR Reanalysis-1. Thanks to the high-resolution time-dependent downscaled wind fields, the TWODEE-2.1 model is capable of performing gas dispersal hazard assessment on very complex terrains for future studies.

CHAPTER 7

Conclusions

Previous chapters of this manuscript include their own section dedicated to summarise and discuss the main contributions of this Ph.D. The following lines summarise the main conclusions of the thesis and propose further steps for the near future.

7.1 Main conclusions

This thesis has focused on the design of an efficient downscaling methodology for operational high-resolution wind forecasts at SMC and BSC-CNS. Because of the limited computational resources of SMC, Physical-Statistical methodologies were identified as a good alternative to the more computationally expensive pure Physical-Dynamical coupling strategies. Since the very beginning, the downscaling methodology was thought as a chain of models, one model dealing with the mesoscale range and the other with the microscale range. To this end, the design process has faced three main objectives introduced in Chapter 1 (Section 1.6):

1. **Improvement of the MMM initial conditions by AWS Data Assimilation (Chapter 3)**
   The research conducted to this end has studied the capacity of WRF-3DVar and LAPS systems to assimilate data from surface Automatic Weather Stations (AWS) in high-resolution operational domains. 3DVar has shown unrealistic large-scale features not representing the inhomogeneous nature of the near-surface fields. In contrast, LAPS has captured small-scale features and has provided an initial condition for WRF much consistent with observations. This can be partially attributed to the fact that the variational analysis in LAPS has been

deactivated. In addition, the validation has shown that, after 24 h of simulation, the wind velocity RMSEs of the simulations initialised with LAPS analysis have been lower than those initialised with WRF-3DVar.

2. **Incorporation of thermal effects in the microscale simulations (Chapter 4)**
   The thermal model of Sogachev et al. [2012] implemented in Alya-CFDWind has allowed the simulation of diurnal cycles, *i.e.* considering atmospheric stability and the dynamics of the ABL. These simulations, together with the selection of certain time instants representative of each stability regime, have provided a framework to circumvent part of the limitations of the neutral atmosphere assumption. For example, the validation of the methodology applied to a Wind Resource Assessment (WRA) in the Puebla site has shown a decrease in the Annual Energy Production (AEP) prediction error with respect to the neutral stratified simulations (from 30.09 to 12.97%), and has shown an AEP distribution remarkably closer to observations.

3. **Design of the downscaling methodology (Chapters 5 and 6)**
   The combination of a domain segmentation technique with the use of transfer functions has demonstrated the ability to, on the one hand, preserve the mesoscale pattern and, on the other hand, incorporate unresolved mesoscale model sub-grid terrain forcing effects from the pre-computed microscale simulations. However, because the mesoscale nature of surface observations, the validation has not allowed the quantification of the gain at points where more pronounced microscale effects can be expected. In addition, the validation has shown that the time periods where the ABL stratification changes from stable to unstable, which coincide with the development of the convective ABL, are still poorly characterised. This has revealed a clear limitation of the methodology that deserves further study. Nonetheless, the downscaling has been successfully applied to simulate atmospheric dense gas dispersal from Lake Nyos in 1986. The results have shown better agreement when compared with previous simulations that used a mass-consistent steady wind at surface.

The fulfilment of these objectives has resulted in an efficient and operationally affordable downscaling methodology designed as a MMM post-process tool for wind field characterisation and forecast. Because the downscaling is a model chain, the assimilation of surface AWS in the MMM initial condition with LAPS can reduce the error of the mesoscale wind velocity forecasts and, consequently, can reduce the error of the downscaling. Microscale pre-computed diurnal cycles solutions are preferred over steady-state solutions because incorporate flow characteristics caused by thermal stratification effects. However, the downscaling success is very case dependent and by definition, fails in situations where thermally driven local phenomena occur, such as during the development of the convective ABL. Further validation with suitable observational data is needed to assess the suitability of the methodology for operational high-resolution wind forecast.

7.2 Future work

This section introduces the steps to implement a downscaling prototype into the operational setup of the SMC and proposes further research to improve the downscaling methodology:

- **Implementation of a downscaling prototype into the SMC operational setup**
  The methodology is ready to be implemented in the SMC operational setup as a prototype. This pre-operational phase will be used to validate and assess the suitability of the methodology. The implementation involves the following steps:

  1. The selection of a region(s) of interest containing several AWS of the observational network.
  2. The introduction of the XEMA network assimilation into the operational WRF model initialisation.
  3. Generate pre-computed diurnal cycle Alya-CFDWind simulations over the region of interest.
  4. The selection of the Alya-CFDWind simulations time instants representative of each stability regime.
  5. The design of a validation strategy.

- **Transfer functions**
  The transfer functions use a radius of influence $\Re$ to spatially average, point by point, the microscale wind velocity. Different values of $\Re$ imply very different scaling factors, *i.e.* significative differences in the resulting downscaled wind modulus. Further research needs to be conducted to use an adaptive $\Re$, where thermal stratification and surrounding topography are considered.

- **Alya-CFDWind diurnal cycle simulations**
  The diurnal cycle simulations have allowed for including thermal stratification considerations into the downscaling methodology, both in terms of forecast and the wind resource assessment. However, some unresolved aspects should be faced in future studies:

  1. The diurnal cycles should be representative of the region under study. This could be achieved linking the methodology with statistical weather classification techniques [e.g.

Badger et al., 2014], introducing different diurnal cycles for each wind velocity direction. In the same line, the inclusion of mesoscale tendencies in the 3D Alya-CFDWind simulations deserve further research.

2. A more suitable temperature distribution should be imposed over the ground; for example a ground temperature field depending on the angle of insolation and on terrain elevation.
3. The thermal model accounts for Coriolis and buoyant forces, that introduce a dependence of the speed up distribution on the velocity modulus. The proposed methodology could improve by simulating several wind velocities for each wind direction. This latter approach would need a larger number of simulations, i.e. increases the computational cost of the methodology which, nonetheless, is still done at the pre-process level.

Bibliography

Aka F. T., Yokoyama T. Current status of the debate about the age of Lake Nyos dam (Cameroon) and its bearing on potential flood hazards // Natural Hazards. 2013. 65, 1. 875–885.

Albers S.C. The LAPS Wind Analysis // Weather and Forecasting. 1995. 10. 342–352.

Albers S.C., McGinley J.A., Birkenheuer D.L., Smart J.R. The Local Analysis and Prediction System (LAPS): Analyses of Clouds, Precipitation, and Temperature // Weather and Forecasting. 1996. 11, September 96. 273–287.

Apsley D., Castro I. A limited-length-scale k-ϵ model for the neutral and stably-stratified atmospheric boundary layer // Boundary-Layer Meteorol. 1997. 83, 1. 75–98.

Arnold D., Morton D., Schicker I., Seibert P., Rotach M. W., Horvath K., Dudhia J., Satomura T., Takemi T., Serafin S., Schmidli J., Schneider S. High Resolution Modelling in Complex Terrain. Report on the HiRCoT 2012 Workshop, Vienna. 4179, February. 2012. 21–23.

Avila M., Folch A., Houzeaux G., Eguzkitza B., Prieto L., Cabezon D. A Parallel CFD Model for Wind Farms // Procedia Comput. Sci. 2013. 18. 2157 – 2166.

Avila M., Gargallo-Peiró A., Folch A. A CFD framework for offshore and onshore wind farm simulation // Journal of Physics: Conf. Series. 2017. 854.

Ayotte K. W. Computational modelling for wind energy assessment // Journal of Wind Engineering and Industrial Aerodynamics. 2008. 96, 10-11. 1571–1590.

Badger J., Frank H., Hahmann Andrea N., Giebel G. Wind-climate estimation based on mesoscale and microscale modeling: Statistical-dynamical downscaling for wind energy applications // Journal of Applied Meteorology and Climatology. 2014. 53, 8. 1901–1919.

Baik J., Park S., Kim J. Urban Flow and Dispersion Simulation Using a CFD Model Coupled to a Mesoscale Model // Journal of Applied Meteorology and Climatology. 2009. 48, 8. 1667–1681.

Barker D. M., Huang W., Guo Y. R., Bourgeois A. A three-dimensional variational (3DVAR) data assimilation system for use with MM5. Boulder, USA, 2003.

Barker D.M., Huang W., Guo Y.-R., Bourgeois A.J., Xiao Q.N. A Three-Dimensional Variational Data Assimilation System for MM5: Implementation and Initial Results // Monthly Weather Review. 2004. 132, 4. 897–914.

Barnes S.L. A technique for Maximizing Details in Numerical Weather Map Analysis // Journal of Applied Meteorology. 1964. 3.

Baxter P., Kapila M. Acute health impact of the gas release at Lake Nyos, Cameroon, 1986 // Journal of Volcanology and Geothermal Research. 1989. 39, 2-3. 265–275.

Blackadar A. K. The vertical distribution of wind and turbulent exchange in a neutral atmosphere // J. Geophys. Res. 1962. 67. 3095–3102.

Bosveld F. C., Baas P., Meijgaard E. van, Bruijn E. I F de, Steeneveld G.-J., Holtslag A. A M. The Third GABLS Intercomparison Case for Evaluation Studies of Boundary-Layer Models. Part A: Case Selection and Set-Up // Boundary-Layer Meteorology. mar 2014a. 152, 2.

Castro F. A., Silva Santos C., Lopes da Costa J. C. One-way mesoscale-microscale coupling for the simulation of atmospheric flows over complex terrain // Wind Energ. VII 2015. 18. 1251–1272.

Castro F.A., Silva Santos C., Costa J.C. Lopes da. One-way mesoscale-microscale coupling for the simulation of atmospheric flows over complex terrain // Wind Energy. 2014.

Chávez-Arroyo R., Sanz-Rodrigo J., Gankarski P. Modelling of atmospheric boundary-layer flow in complex terrain with different forest parameterizations // J. Phys.: Conf. Ser. 2014. 524. 012119.

Chen F., Dudhia J. Coupling an Advanced Land Surface–Hydrology Model with the Penn State–NCAR MM5 Modeling System. Part I: Model Implementation and Sensitivity // Monthly Weather Review. 2001. 129, 4. 569–585.

Chung T.J. Computational Fluid Dynamics. 2002. 1012.

Coirier W.J., Kim S., Chen F., Tewari M. Evaluation of urban scale contaminant transport and dispersion modeling using loosely coupled CFD and mesoscale models // 6th Symposium on the Urban Environment and Forum on Managing our Physical and Natural Resources. 2006.

Costa A., Chiodini G. Modelling Air Dispersion of CO^2 from Limnic Eruptions // Volcanic Lakes. Berlin, Heidelberg: Springer Berlin Heidelberg, 2015. 451–465.

Costa A., Chiodini G., Granieri D., Folch A., Hankin R.K.S., Caliro S., Avino R., Cardellini C. A shallow- layer model for heavy gas dispersion from natural sources: application and hazard assessment at Caldara di Manziana, Italy // Geochem Geophys Geosyst. 2008. 9:Q03002.

Cuxart J., Holtslag A. A. M., Beare R. J., Bazile E., Beljaars A., Cheng A., Conangla L., Ek M., Freedman F., Hamdi R., Kerstein A., Kitagawa H., Lenderink G., Lewellen D., Mailhot J., Mauritsen T., Perov V., Schayes G., Steeneveld G-J., Svensson G., Taylor P., Weng W., Wunsch S., Xu K-M. Single-Column Model Intercomparison for a Stably Stratified Atmospheric Boundary Layer // Boundary-Layer Meteorology. 2006. 118, 2. 273–303.

Daley R. Atmospheric Data Analysis. 1991. 457.

Deng X., Stull R. A mesoscale analysis method for surface potential temperature in mountainous and coastal terrain // Monthly Weather Review. 2005. 389–408.

Deng X., Stull R. Assimilating Surface Weather Observations from Complex Terrain into a High-Resolution Numerical Weather Prediction Model // Monthly Weather Review. 2007. 135, 3. 1037–1054.

Dudhia J. Numerical study of convection observed during the winter monsoon experiment using a mesoscale two-dimensional model // Journal of the Atmospheric Sciences. 1989.

Ehrhard J., Khatib I., Winkler C., Kunz R., Moussiopoulos N., Ernst G. The microscale model MIMO: development and assessment // Journal of Wind Engineering and Industrial Aerodynamics. 2000. 85, 2. 163–176.

Evans W. C., White L. D., Tuttle M. L., Kling G. W., Tanyileke G., Michel R. L. Six years of change in Lake Nyos, Cameroon, yield clues to the past and cautions for the future // Geochemical Journal. 1994. 28, 3. 139–162.

Folch A., Barcons J., Kozono T., Costa A. High-resolution modelling of atmospheric dispersion of dense gas using TWODEE-2.1: application to the 1986 Lake Nyos limnic eruption // Natural Hazards and Earth System Sciences. jun 2017. 17, 6. 861–879.

Folch A., Costa A., Hankin R.K.S. twodee-2: A shallow layer model for dense gas dispersion on complex topography // Computers & Geosciences. 2009. 35, 3. 667–674.

Frank H. P., Landberg L. Modelling the wind climate of Ireland // Boundary-Layer Meteorology. 1997. 85. 359–378.

Frey-Buness F., Heimann D., Sausen R. A statistical-dynamical downscaling procedure for global climate simulations // Theoretical and Applied Climatology. 1995. 50, 3-4. 117–131.

Gargallo-Peiró A., Avila M., Owen H., Prieto L., Folch A. Mesh Generation for Atmospheric Boundary Layer Simulation in Wind Farm Design and Management // Procedia Eng. 2015. 124. 239–251.

Garratt J. R. The atmospheric boundary layer (Cambridge atmospheric and space science series). 1994. 316.

Ha J.-H., Lee D.-K. Effect of Length Scale Tuning of Background Error in WRF- 3DVAR System on Assimilation of High-Resolution Surface Data for Heavy Rainfall Simulation // Advances in Atmospheric Sciences. 2012. 29, 6. 1142–1158.

Hanjalić K., Kenjereš S. Some developments in turbulence modeling for wind and environmental engineering // Journal of Wind Engineering and Industrial Aerodynamics. 2008. 96, 10-11. 1537–1570.

Hankin R. K. S., Britter R. E. TWODEE: The Health and Safety Laboratory shallow layer model for heavy gas dispersion. Part 1. Mathematical basis and physical assumptions // J. Hazard. Mater. 1999. A66, A66. 211–226.

Harper P. Assessment of the major hazard potential of carbon dioxide (CO2). June 2011. 28.

Haupt S.E., Zajaczkowski F.J., Long K.J., Annunzio A.J. Assimilating numerical weather prediction data into computational fluid dynamics models for wind prediction // CWE2010, Chapel Hill, North Carolina, USA. 2010.

Hiemstra C.A., Liston G.E., Pielke R.A., Birkenheuer D.L., Albers S.C. Comparing Local Analysis and Prediction System (LAPS) Assimilations with Independent Observations // Weather and Forecasting. 2006. 1024–1040.

Holtslag A. A M, Svensson G., Baas P., Basu S., Beare B., Beljaars A. C M, Bosveld F. C., Cuxart J., Lindvall J., Steeneveld G. J., Tjernström M., Van De Wiel B. J H. Stable atmospheric boundary layers and diurnal cycles: Challenges for weather and climate models // Bulletin of the American Meteorological Society. 2013. 94, 11. 1691–1706.

Holtslag Albert A M. Introduction to the Third GEWEX Atmospheric Boundary Layer Study (GABLS3) // Boundary-Layer Meteorology. aug 2014. 152, 2. 127–132.

Homicz G. F. Three-dimensional wind field modeling: a review // Sandia National Laboratories, Albuquerque, SANDIA. 2002. August.

Hong S-Y., Dudhia J. Next-Generation Numerical Weather Prediction: Bridging Parameterization, Explicit Clouds, and Large Eddies // Bulletin of the American Meteorological Society. 2012. 93, 1. ES6–ES9.

Hong S.-Y., Lim J.-O.J. The WRF Single-Moment 6-Class Microphysics Scheme (WSM6) // Journal of The Korean Meteorological Society. 2006. 42. 129–151.

Hong S.-Y., Noh Y., Dudhia J. A new vertical diffusion package with an explicit treatment of entrainment processes // Monthly Weather Review. 2006. 2318–2341.

Houzeaux G., Vázquez M., Cela J.M. A Massively Parallel Fractional Step Solver for Incompressible Flows // Journal of Computational Physics. 2009. 228, 17. 6316–6332.

Janjić Z.I. The step-mountain eta coordinate model: further developments of the convection, viscous sublayer and turbulence closure schemes // Mon. Wea. Rev. 1994. 122. 927–945.

Janjić Z.I. The surface layer in the NCEP Eta Model // Eleventh Conference on Numerical Weather Prediction, Norfolk, VA, 19-23 August; Amer. Meteor. Soc., Boston, MA, 354-355. 1996.

Janjić Z.I. Nonsingular Implementation of the Mellor-Yamada Level 2.5 Scheme in the NCEP Meso model // NOAA/NWS/NCEP Office Note 437. 2001.

Jones W.P., Launder B.E. The prediction of laminarization with a two-equation model of turbulence // International Journal of Heat and Mass Transfer. 1972. 15, 2. 301–314.

Justus C.G., Mikhail A. Height variation of wind speed and wind distributions statistics // Geophysical Research Letters. 1976. 3, 5. 261–264.

Kain J.S. The Kain-Fritsch convective parameterization: an update // Journal of Applied Meteorology. 2004. 1980. 170–181.

Kalnay E., Kanamitsu M., Kistler R., Collins W., Deaven D., Gandin L., Iredell M., Saha S., White G., Woollen J., Zhu Y., Leetmaa A., Reynolds R., Chelliah M., Ebisuzaki W., Higgins W., Janowiak J., Mo K. C., Ropelewski C., Wang J., Jenne R., Joseph D. The NCEP/NCAR 40-Year Reanalysis Project // Bulletin of the American Meteorological Society. 1996. 77, 3. 437–471.

Kanari S. I. An inference on the process of gas outburst from Lake Nyos, Cameroon // Journal of Volcanology and Geothermal Research. 1989. 39, 2-3. 135–149.

Klemp J. B., Skamarock W. C., Dudhia J. Conservative Split-Explicit Time Integration Methods for the Compressible Nonhydrostatic Equations // Monthly Weather Review. 2007. 135, 8. 2897–2913.

Kling G. W, Clary M. A., Compton H. R., Devine J. D., Evans W. C., Humphrey A. M., Koenigsberg E. J., Lockwood J. P., Tuyrle M. L., Wagner G. N. The 1986 Lake Nyos Gas Disaster in Cameroon, West Africa // Science. 1986. 236. 169–175.

Kling G. W., Evans W. C., Tanyileke G., Kusakabe M., Ohba T., Yoshida Y., Hell J. V. Degassing Lakes Nyos and Monoun: defusing certain disaster. // Proceedings of the National Academy of Sciences of the United States of America. 2005. 102, 40. 14185–14190.

Koblitz T., Bechmann A., Sogachev A., Sørensen N., Réthoré P. E. Computational Fluid Dynamics Model of Stratified Atmospheric Boundary-Layer Flow // Wind Energy. 2015. 18. 75–89.

Kumar V., Svensson G., Holtslag A. A M, Meneveau C., Parlange M. B. Impact of surface flux formulations and geostrophic forcing on large-eddy simulations of diurnal atmospheric boundary layer flow // Journal of Applied Meteorology and Climatology. 2010. 49, 7. 1496–1516.

Kunz R., Khatib I., Moussiopoulos N. Coupling of mesoscale and microscale models—an approach to simulate scale interaction // Environmental Modelling & Software. 2000. 15, 6-7. 597–602.

Kusakabe M., Ohba T., Issa ., Yoshida Y., Satake H., Ohizumi T., Evans W. C., Tanyileke G., Kling G. W. Evolution of CO 2 in lakes Monoun and Nyos, Cameroon, before and during controlled degassing // Geochemical Journal. 2008. 42, 1. 93–118.

Lazarus S.M., Brewster K.A., Horel J.D., Ciliberti C.M. Near-Real-Time Applications of a Mesoscale Analysis System to Complex Terrain // Weather and Forecasting. 2002. 17, 5. 971–1000.

Le Guern F., Shanklin E., Tebor S. Witness accounts of the catastrophic event of August 1986 at Lake Nyos (Cameroon) // Journal of Volcanology and Geothermal Research. 1992. 51, 1-2. 171–184.

Li L., Zhang L.-J., Zhang N., Hu F., Jiang Y., Xuan C.-Y., Jiang W.-M. Study on the microscale simulation of wind field over complex terrain by RAMS/FLUENT modeling system // CWE2010, Chapel Hill, North Carolina, USA. 2010.

Lockwood J. P., Rubin M. Origin and age of the Lake Nyos maar, Cameroon // Journal of Volcanology and Geothermal Research. 1989. 39, 2-3. 117–124.

McGinley J., Smart J. On providing a cloud-balanced initial condition for diabatic initialization. // Preprints, 14 th Conf. On Numerical Weather Prediction, Ft. Lauderdale, Amer. Meteor. Soc. 2001.

McGinley J.A., Albers S.C., Stamus P.A. Validation of a Composite Convective Index as Defined by a Real-Time Local Analysis System // Weather and Forecasting. 1991. 6, 3. 337–356.

Mengelkamp H.-T., Kapitza H., Pflüger U. Statistical-dynamical downscaling of wind climatologies // Journal of Wind Engineering and Industrial Aerodynamics. 1997. 67-68. 449–457.

Miao Y., Liu S., Chen B., Zhang B. Simulating urban flow and dispersion in Beijing by coupling a CFD model with the WRF model // Advances in Atmospheric Sciences. 2013. 30, 6. 1663–1678.

Mirocha J. D., Lundquist J. K., Kosović B. Implementation of a Nonlinear Subfilter Turbulence Stress Model for Large-Eddy Simulation in the Advanced Research WRF Model // Monthly Weather Review. 2010. 138, 11. 4212–4228.

Mlawer E.J., Taubman S.J., Brown P.D., Iacono M.J., Clough S.A. Radiative transfer for inhomogeneous atmospheres: RRTM, a validated correlated-k model for the longwave // Journal of Geophysical Research: Atmospheres. 1997. 102, D14. 16663–16682.

Mochida A., Iizuka S., Tominaga Y., Lun I. Y-F. Up-scaling CWE models to include mesoscale meteorological influences // Journal of Wind Engineering and Industrial Aerodynamics. 2011. 99, 4. 187–198.

Mochida A., Lun I.Y.F. Prediction of wind environment and thermal comfort at pedestrian level in urban area // Journal of Wind Engineering and Industrial Aerodynamics. 2008. 96, 10-11. 1498–1527.

Moeng C-H., Dudhia J., Klemp J., Sullivan P. Examining Two-Way Grid Nesting for Large Eddy Simulation of the PBL Using the WRF Model // Monthly Weather Review. 2007. 135, 6. 2295–2311.

Monin A. S., Obukhov A. Basic laws of turbulent mixing in the surface layer of the atmosphere. // Contrib. Geophys. Inst. Acad. Sci. USSR. IX 1954. 151. 163–187.

Morton D., Nudson O., Bahls D., Newby G., Region A. The Weather Research and Forecasting (WRF) Model as a Tool for Evaluating HPCMP Assets and Capabilities in Grand Scale Numerical Weather Prediction, 2010 DoD HPCMP Users Group Conference, Schaumburg. 2010.

Müller M.D. Effects of Model Resolution and Statistical Postprocessing on Shelter Temperature and Wind Forecasts // Journal of Applied Meteorology and Climatology. 2011. 50, 8. 1627–1636.

Parrish D.F., Derber J.C. The National Meteorological Center's Spectral Statistical-Interpolation Analysis System // Monthly Weather Review. 1992. 120, 8. 1747–1763.

Persson A. User guide to ECMWF forecast products. 2015. 127.

Pieterse J.E. E., Harms T.M. M. CFD investigation of the atmospheric boundary layer under different thermal stability conditions // Journal of Wind Engineering and Industrial Aerodynamics. 2013. 121. 82–97.

Pinto J. G., Neuhaus C. P., Leckebusch G. C., Reyers M., Kerschgens M. Estimation of wind storm impacts over Western Germany under future climate conditions using a statistical-dynamical downscaling approach // Tellus, Series A: Dynamic Meteorology and Oceanography. 2010. 62, 2. 188–201.

Pu Z., Zhang H., Anderson J. Ensemble Kalman filter assimilation of near-surface observations over complex terrain: comparison with 3DVAR for short-range forecasts // Tellus A. 2013. 65, 19620.

Purser R.J., Wu W.-S., Parrish D.F., Roberts N.M. Numerical Aspects of the Application of Recursive Filters to Variational Statistical Analysis. Part I: Spatially Homogeneous and Isotropic Gaussian Covariances // Monthly Weather Review. 2003. 131, 8. 1524–1535.

Sanz-Rodrigo J., Chávez-Arroyo R. A., Moriarty P., Churchfield M., Kosović B., Réthoré P.-E., Hansen K. S., Hahmann A., Mirocha J. D., Rife D. Mesoscale to microscale wind farm flow modeling and evaluation // Wiley Interdisciplinary Reviews: Energy and Environment. 2016a.

Sanz-Rodrigo J., Churchfield M., Kosović B. A methodology for the design and testing of atmospheric boundary layer models for wind energy applications // Wind Energy Science. feb 2017. 2, 1. 35–54.

Sanz-Rodrigo J., Churchfield M., Kosović B.. A wind energy benchmark for ABL modelling of a diurnal cycle with a nocturnal low-level jet: GABLS3 revisited // J. Phys.: Conf. Ser. 2016b. 753. 032024.

Sanz-Rodrigo J., Garcia B., Cabezón D., Lozano S., Martí I., García B. Downscaling mesoscale simulations with CFD for high resolution regional wind mapping // Proc. European Wind Energy Conference (Warsaw, Poland). 2010.

Skamarock W.C., Klemp J.B., Dudhia J. A description of the advanced research WRF version 3 // NCAR/TN–475+STR. 2008.

Sogachev A., Kelly M., Leclerc M. Y. Consistent two-equation closure modelling for atmospheric research: Buoyancy and vegetation implementations // Boundary-Layer Meteorology. 2012. 145, 2. 307–327.

Spalart P. R., Jou W. H., Strelets M., Allmaras S. R. Comments on the feasibility of LES for wings and on a hybrid RANS/LES approach // 1st AFOSR International Conference on DNS/LES, Rustin, LA. Advances in DNS/LES, Liu C and Liu Z (Eds.), Greyden Press, Columbus, OH,. 1997.

Stensrud D. J., Yussouf N., Dowell D. C., Coniglio M. C. Assimilating surface data into a mesoscale model ensemble: Cool pool analyses from spring 2007 // Atmos. Res. 2009. 93. 207–220.

Stull R. An introduction to boundary layer meteorology. 1988.

Svensson G., Holtslag A. A M, Kumar V., Mauritsen T., Steeneveld G. J., Angevine W. M., Bazile E., Beljaars A., Bruijn E. I F de, Cheng A., Conangla L., Cuxart J., Ek M., Falk M. J., Freedman F., Kitagawa H., Larson V. E., Lock A., Mailhot J., Masson V., Park S., Pleim J., Söderberg S., Weng W., Zampieri M. Evaluation of the diurnal cycle in the Atmospheric Boundary Layer over land as Represented by a Variety of Single-Column models: The second GABLS EXperiment // Boundary-Layer Meteorology. 2011. 140, 2. 177–206.

Taylor P.A., Walmsley J.L., Salmon J.R. A simple model of neutrally stratified boundary-layer flow over real terrain incorporating wave number-dependent scaling // Boundary-Layer Meteorology. 1983. 26. 169–189.

Tewari M., Kusaka H., Chen F., Coirier W. J., Kim S., Wyszogrodzki A., Warner T. T. Impact of coupling a microscale computational fluid dynamics model with a mesoscale model on urban scale contaminant transport and dispersion // Atmospheric Research. 2010. 96, 4. 656–664.

Toshihiro K., Akihiro K., Hiromasa U., Leonard K. P. Estimation of vertical air motion from limited horizontal wind data numerical experiment // Atmospheric Environment (1967). 1983. 17, 11. 2181 – 2192.

Troen I., Petersen E.L. The European Wind Atlas // Riso National Laboratories, Denmark. 1998. 656pp.

Tuttle M.L., Clark M.A., Compton H.R, Devine J.D., Evans W.C., Humphrey A.M., Kling G.W., Koenigsberg E.J., Lockwood J.P., Wagner G.N. The 21 August (1986) Lake Nyos gas disaster, Cameroon. 1987. 87–97.

Udina M., Sun J., Kosović B., Soler M. R. Exploring Vertical Turbulence Structure in Neutrally and Stably Stratified Flows Using the Weather Research and Forecasting Large-Eddy Simulation (WRF-LES) Model // Boundary-Layer Meteorol. 2016. 161, 2. 355–374.

Vázquez M., Houzeaux G., Koric S., Artigues A., Aguado-Sierra J., Arias R., Mira D., Calmet H., Cucchietti F., Owen H., Taha A., Dering Burness E., Cela J.M., Valero M. Alya: Multiphysics engineering simulation toward exascale // J. Comput. Scie. 2016. 14. 15–27.

Veiga Rodrigues C., Palma J. M L M, Rodrigues Á. H. Atmospheric Flow over a Mountainous Region by a One-Way Coupled Approach Based on Reynolds-Averaged Turbulence Modelling // Boundary-Layer Meteorology. may 2016. 159, 2. 407–437.

Veiga Rodrigues C., Santos C. M. S., Palma J. M. L. M., Castro F. A., Miranda P. M. A., Rodrigues A. H. Short-term Forecasting of a Wind Farm Output using CFD // European Wind Energy Conference and Exhibition, Brussels, Belgium. 2008.

Wagenbrenner N. S., Forthofer J. M., Lamb B. K., Shannon K. S., Butler B. W. Downscaling surface wind predictions from numerical weather prediction models in complex terrain with WindNinja // Atmospheric Chemistry and Physics. 2016. 16. 5229–5241.

Wallace J. M., Hobbs P. V. Atmospheric Science: an Introductory Survey (Second Edition). 2006.

Warner T.T. Numerical Weather and Climate Prediction. 2011. 526 S.

Wicker L.J., Skamarock W.C. Time-Splitting Methods for Elastic Models Using Forward Time Schemes // Monthly Weather Review. 2002. 130, 8. 2088–2097.

Wilcox D.C. Reassessment of the scale-determining equation for advanced turbulence models // AIAA Journal. 1988. 26, 11. 1299–1310.

Wyngaard J.C. Toward Numerical Modeling in the "Terra Incognita" // Journal of the Atmospheric Sciences. 2004. 61, 14. 1816–1826.

Xie Y., Koch S., McGinley J., Albers S., Bieringer P. E., Wolfson M., Chan M. A Space–Time Multiscale Analysis System: A Sequential Variational Analysis Approach // Mon. Wea. Rev. 2011. 139. 1224–1240.

Yamada T., Koike K. The A2C Mesoscale Meteorological Modeling System for Computational Wind Engineering Applications // CWE2010, Chapel Hill, North Carolina, USA. 2010.

Yamada T., Koike K. Downscaling mesoscale meteorological models for computational wind engineering applications // Journal of Wind Engineering and Industrial Aerodynamics. 2011. 99, 4. 199–216.

Zajaczkowski F. J., Haupt S. E., Schmehl K. J. A preliminary study of assimilating numerical weather prediction data into computational fluid dynamics models for wind prediction // J. Wind Eng. Ind. Aerodyn. apr 2011. 99, 4. 320–329.